UC Santa Barbara
UC Santa Barbara Electronic Theses and Dissertations

Title

DNA nanostars: A model system to investigate biomolecular condensation

Permalink

https://escholarship.org/uc/item/8tb2s168

Author

Abraham, Gabrielle Rose Cronin

Publication Date

2023

Peer reviewed|Thesis/dissertation

University of California
Santa Barbara

DNA nanostars: A model system to investigate biomolecular condensation

A dissertation submitted in partial satisfaction
of the requirements for the degree

Doctor of Philosophy

in

Physics

by

Gabrielle Rose Cronin Abraham

Committee in charge:

Professor Omar A. Saleh, Co-Chair
Professor Deborah K. Fygenson, Co-Chair
Professor Zvonimir Dogic
Professor M. Cristina Marchetti

March 2023

The Dissertation of Gabrielle Rose Cronin Abraham is approved.

Professor Zvonimir Dogic

Professor M. Cristina Marchetti

Professor Deborah K. Fygenson, Committee Co-Chair

Professor Omar A. Saleh, Committee Co-Chair

March 2023

DNA nanostars: A model system to investigate biomolecular condensation

Copyright © 2023

by

Gabrielle Rose Cronin Abraham

Acknowledgements

Curriculum Vitæ
Gabrielle Rose Cronin Abraham

Education

2023	Ph.D. in Physics (Expected), University of California, Santa Barbara.
2019	M.A. in Physics, University of California, Santa Barbara.
2016	B.S. in Physics, University of Arkansas

Honors and Awards

2016–2019	National Science Foundation Graduate Research Fellowship
May 2021	Chair's Appreciation Award
October 2020	Women in Science and Engineering Womxn of the Month
2017, 2019	Physics Circus Outreach Award
June 2020	Physics Summer Fellowship
2019–2020	UCSB Central Fellowship
March 2018	Graduate Student Associate Travel Grant
2017	Tel Aviv Travel Fellowship
2016–2017	Broida Fellowship
2016–2017	Yzurdiaga Fellowship

Publications

- B.-j. Jeon, D. T. Nguyen, **Gabrielle R. Abraham**, N. Conrad, Deborah K. Fygenson, and Omar A. Saleh. (2018) Salt-dependent properties of a coacervate-like, self-assembled DNA liquid. *Soft Matter* 14(34): 7009–7015.

- D. T. Nguyen, B.-j. Jeon, **Gabrielle R. Abraham**, and Omar A. Saleh. (2019) Length-Dependence and Spatial Structure of DNA Partitioning into a DNA Liquid. *Langmuir* 35(46): 14849–14854.

Abstract

DNA nanostars: A model system to investigate biomolecular condensation

by

Gabrielle Rose Cronin Abraham

Biomolecular condensates — phase-separated drops of proteins and nucleic acids — provide vital spatial organization within cells. Model systems made up of proteins and/or nucleic acids are useful to elucidate the underlying principles that govern the phase separation of biomolecules. Here, I investigate a model system composed of branched, limited valence particles called DNA nanostars, which can phase separate into a DNA-rich phase and a DNA-dilute phase. Nanostars are unique in that they are composed entirely of DNA; thus, modulating individual nanostar properties is straightforward through sequence engineering of the constituent strands. Specifically, one can easily tune key molecular parameters associated with phase separation such as valence and the strength of interactions between particles. Additionally, because nanostars interact via base pairing, it is facile to relate nanostar phase behavior to the binding free energy of inter-nanostar interactions.

In this dissertation, I discuss three projects in which I examine various aspects of nanostar liquids, as motivated by key behaviors of biomolecular condensates. In the first project, I show that the physical properties of the nanostar dense phase — such as the viscosity, macromolecular density, and surface tension — are similar to the properties of biomolecular condensates. However, because nanostar interactions are driven by base pairing while other biomolecular condensates form via electrostatic attractions, the two condensates exhibit contrary responses to changing salt concentration. In the second project, I show that nanostar drops exhibit selective partitioning of solutes, analogous to

behavior displayed by biomolecular condensates. I quantify the effects of adding one or two nanostar binding sites on solute particles and show that this can counter the length-dependent entropic confinement that affects long solutes when entering the nanostar dense phase. In the third project, I investigate a system that mimics the heterogeneity of composition and interactions of biological condensates. When nanostars are combined with a positively charged polymer, I observe a rich phase diagram in which electrostatic and base pairing interactions cooperate in some cases and compete in others to form multiple distinct phases that can coexist.

Overall, this work demonstrates that nanostar phase behavior is highly predictable when phase separation is driven by nanostar–nanostar base pairing. Additionally, I use nanostar drops to mimic several key properties of biomolecular condensates and am able to draw conclusions about the effects of interaction thermodynamics on phase behavior. These results clarify why the nanostar system is interesting to investigate from a material standpoint as well — the dense phase has a surprisingly low volume fraction due to the rigidity of the nanostar arms and sequence-specific interactions can be used to predictably functionalize the nanostar dense phase. These properties can be exploited to create nanostar materials that target specific cell types, act as molecular sensors, or sequester relatively large solute particles.

Contents

Chapter 1

Introduction

1.1 Motivation

1.1.1 Phase separation in biology

Liquid-liquid phase separation (LLPS), the process by which polymers condense into a polymer-dense phase that is spatially distinct from a polymer-dilute phase, is now considered ubiquitous in sub-cellular organization [1, 2]. Within the cell, protein–protein and protein–nucleic acid attractions create phase separated structures that have been implicated in a vast number of vital roles — for example chromosome structuring, transcription, protection of RNA, microtubule organization, ribosome creation, etc. [3, 4, 5, 6]. Characterization of biomolecular condensates (also known as intracellular droplets and membraneless organelles) has shown that they tend to be size-limited droplets with a typical mesh size of around 5 nm, viscosities typically of order 1–10 Pa·sec, and a low surface tension that is generally of order $0.5 - 1$ μN/m [1, 7, 8, 9]. Biomolecular condensates, like membrane-bound organelles, act as compartments that are distinct from the rest of the cell. However, unlike traditional, membrane-bound organelles, biomolec-

ular condensates form dense meshworks via reversible LLPS; thus, the organization they offer in the cell is two fold: (1) Biomolecular condensates create temporal organization because they are dynamic and can dissolve and reform based on cell state [6, 10]. (2) Some molecular species are excluded from the biomolecular condensate while others are highly concentrated within it; thus they create spatial organization [6, 10]. Because of this, biomolecular condensates are sometimes described as temporary reactors: by locally concentrating molecules and changing the local solution conditions, reaction rates within biomolecular condensates may be enhanced [1, 2, 6].

Intracellular phase separation is incredibly complex: The surrounding environment is crowded [7]; the condensates can be composed of (potentially) hundreds of components, which have the potential for numerous interaction types (e.g., electrostatic, $\pi - \pi$ interactions, and hydrophobic interactions) [11, 12, 13, 14]; some of the components can change state via post-translational modifications and configurational changes [1, 6]; and it has been suggested that entering a biomolecular condensate can *cause* a component to change state [15, 16]. Further, the material properties of biomolecular condensates are known to vary as well. For example, some works have shown that some biomolecular condensates can exhibit gel-like behavior such as not fully rounding up into a sphere or incomplete recovery after photobleaching (indicating that some molecules are kinetically trapped rather than rearranging as in a liquid) [1, 6]. However, many *in vivo* and *in vitro* experiments have observed liquid-like behavior of biomolecular condensates. For example, nucleoli have been observed coalescing and P granules have been shown to flow under stress [17, 18]. On the other hand, some works have concluded that biomolecular condensates are dynamic structures that can transition from a liquid-like state to a gel-like state [19]. Furthermore, aberrant phase transitions have been implicated in some diseases (e.g., coacervates containing FUS proteins have appeared solid-like rather than liquid-like in cells with amyotrophic lateral sclerosis, ALS) [20, 21]. Due to the complexity

of biomolecular condensates, a consensus of the principles that determine biomolecular condensation has yet to be reached.

1.1.2   Beyond intracellular phase separation

LLPS is prominent outside of cellular biology as well. The RNA world hypothesis postulates that even before the creation of cells, LLPS played a role in the creation of life. In this theory, RNA nucleotides phase separated with multi-valent cations, e.g., Mg^{2+}, which allowed them to surpass a concentration threshold and polymerize into the first biopolymers [22, 23]. Additionally, artificial phase separated structures have been used to create biomimetic smart materials and have replicated several key properties of intracellular droplets such as selective-partitioning (i.e., only certain molecules will enter the dense phase), enzyme-promoted phase separation and dissolution, and coexisting multiple dense phases that remain immiscible [2, 24, 25, 26, 27]. These works studied *in vitro* model biomolecular condensates to hone in on the individual molecular properties that impact intracellular condensation [1, 10]. Finally, LLPS has been used to purify proteins, can alter flavor perception in food, and has been suggested as a means for drug delivery [28, 29, 30].

1.2   The DNA nanostar

Nanostars (NSs) are small, branched DNA particles that can condense into liquids or gels via a limited number of interactions. Because NSs are (for the most part) composed entirely of DNA, individual NS properties — such as valency, arm length, and internal flexibility — can be predictably designed using already available programs [31, 32, 33]. Additionally, synthesis of specific DNA sequences is cheap and accessible, and, once formed, NSs are nearly monodisperse [34, 35]. Moreover, most NSs undergo phase sepa-

ration via well-characterized Watson-Crick-Franklin base pairing, so unlike other phase separating systems, the thermodynamic properties of inter-NS interactions can be readily calculated [34, 35]. These characteristics make NSs an ideal structure to study phase separation and give the NS system an advantage over other model biomolecular condensate systems: one can easily describe which aspects of NS phase separation depend on inter-particle interactions and which depend on other molecular properties. (See Chapter 2 for a review of DNA hybridization thermodynamics.) As a material, the mesh size of NS networks is relatively large (around 10 nm) because the arms are double-stranded and thus stiff. This allows small molecules and proteins to partition into the dense phase, such as drugs or gold nanoparticles [35, 36]. In addition, proteins and molecules that are known to interact with DNA will similarly interact with NSs, providing numerous tools to make the NS system active [37, 38].

1.2.1   Nanostar anatomy

NSs are limited-valence constructs composed of DNA. All NSs contain a core region which includes double stranded arms that extend from a central junction (Fig. 1.1A). Recent work has shown that the kinetics of NS droplet formation depend strongly on the length of each arm where smaller NSs result in smaller, slower growing condensates [39]. The concentration of NSs in the dense phase is dependent on the amount of space that is taken up by each NS; thus changing the arm length or the available configurations of individual NSs is expected to impact the NS phase boundary [40, 41, 42]. Beyond NS size, Lee et al. (2021) introduced extra flexibility by incorporating unpaired regions in the middle of each NS arm. They showed that the unpaired regions have a small impact on the concentration in the dense phase, but that they weaken inter-NS interactions resulting in a dense phase that is more dynamic and that has a lower critical salt [43].

Proper formation of the NS core is the key first step to a successful NS experiment. However, after NSs are annealed, a fraction of the NS cores will be imperfect (perhaps due to truncated oligomers or imperfect stoichiometry of oligomers). Previous work determined that misformed NSs are largely excluded from the droplet phase resulting in an over estimation of the concentration of DNA in the dilute phase [34]. Additionally, other work showed that misformed NSs will act as a surfactant and bridge NS drops that would otherwise not interact [26].

Frequently, NSs contain two unpaired nucleotides at the central junction, which create angular flexibility between arms of individual NSs [34, 41, 44]. Excluding the unpaired bases at the junction does not prevent NS formation, but it can allow the junction to migrate if specific design principles are not followed [45, 46]. These unpaired nucleotides have been shown to impact NS relaxation in the gel phase: in monovalent salt, NS gels contract faster with unpaired nucleotides at the junction, but in divalent salt, NS gels coarsen faster when the unpaired nucleotides are excluded [47]. Similarly, Um et al. (2006) showed that internal structure of covalently-linked hydrogels resemble reptile scales for NSs with confined arms but is fibrous and fractal for NSs with flexible arms [48]. Finally, NSs that interact via cholesterol functionalization have been shown to form crystalline structures if unpaired nucleotides are included in the junction. The exclusion of these nucleotides prevents crystallization perhaps because the individual NS configurations necessary to form the crystal are restricted without the additional angular flexibility provided by the unpaired nucleotides [44].

Beyond NS core design, the effects of inter-NS interactions on bulk phase separation has been heavily investigated. Tails at the end of each arm (known as overhangs if they are composed of single-stranded DNA) are usually used to drive phase separation. NSs often interact via Watson-Crick-Franklin base pairing, but other interaction types have been used. For example, NSs with cholesterol-functionalized arms have been
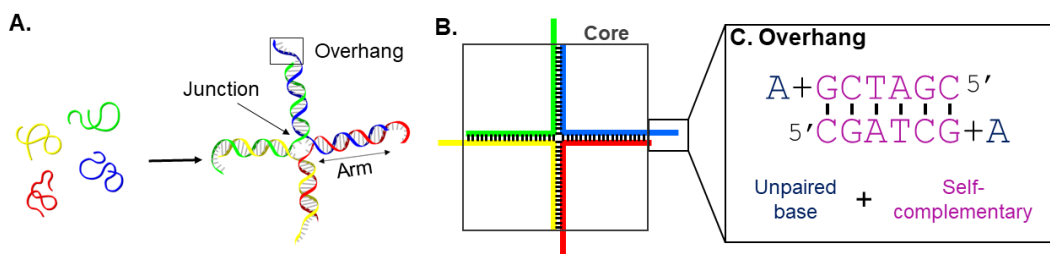
5

Figure 1.1: **Anatomy of a NS** (A.) Schematic of individual NS constructs. NSs begin as four sinlge stranded DNA (ssDNA) oligomers. (Here, each strand is represented by a distinct color.) Upon annealing, half of each oligomer will bind to half of another oligomer to form a NS. (B.) Simplified diagram of a NS that highlights the partial complementarity of two oligomers. (C.) Overhangs are single stranded sequences at the end of NS arms. Self-complementary regions allow NSs to condense. Note that the sequences of the pink region are the same if read from the 5' end. The blue gap nucleotides break up base stacking between the sticky ends and the NS arms. (A.) is adapted from [41] with permission from the Royal Society of Chemistry.

used to create DNA 3D crystals via the multi-body interaction of the hydrophobic tails (i.e., hydrophobic tails interact with tails on three or more neighboring NSs as opposed to the two-body interaction of NS overhang hybridization) [44]. In addition, NSs with overhangs that are rich in cytosine can form inter-NS i-motifs that create pH-responsive NS hydrogels [49]. Beyond these examples, NSs generally interact via base pairing of overhang sequences. Often, the overhang sequence contains a self-complementary region (Fig. 1.1C). These palindromic motifs, known as sticky ends, result in inter-NS attractions that can drive phase separation [50, 51]. One can design orthogonal sticky ends, or two self-complementary sticky ends that do not interact with each other, such that two types of immiscible NS drops can coexist; however, orthogonal NS drops will mix if "surfactant" NSs that contain both types of sticky ends, are included [26, 27]. NSs will also condense when the overhang sequences are not self-complementary if extra components that bind to two NSs, like double stranded DNA (dsDNA) linkers, are included [52, 53].

The thermodynamics of sticky ends binding largely dictate phase behavior and the properties of the dense phase. Longer or stronger overhang sequences result in more stable

inter-NS interactions. Thus, the critical temperature for DNA liquid or gel formation increases with stronger overhangs [27, 40, 54, 55, 56]. NSs with weaker overhangs form more concentrated liquids and gels and less viscous liquids perhaps due to their increased propensity for rearrangement [27, 41]. In addition to the sequence of the sticky end, once two NSs bind, the double stranded sticky end can base stack with neighboring double stranded arms, creating a more stable NS interaction. Breaking up the sticky end–arm base stacking by including a "gap nucleotide" that remains unpaired upon two NSs binding will weaken the interaction (Fig. 1.1C). For example, NSs with the same sticky ends have been shown to form gels when the gap nucleotide is excluded but form liquids when it is included [47].

The impacts of the number of overhangs, or the valency, have also been investigated. Increasing the valency from three to four results in a significantly higher critical temperature for LLPS; however, increasing the valency further (e.g., to five or six) causes a much smaller increase [34, 42]. The transition temperature from the liquid phase to the gel phase has also been shown to increase with valency [27]. In addition, the mass concentration within the dense phase has been shown to change significantly between three-armed and four-armed NSs and between five-armed and six-armed NSs, but the change in density between four-armed and five-armed NSs is small comparatively [42]. This matches previous rheological work that shows that the scaling of the elastic response of a NS gel with respect to NS volume fraction depends on valency. Conrad et al. (2019) observed a large change in the scaling behavior between three- and four-armed NSs and five- and six- armed NSs, the elastic behavior of four- and five-armed NS gels scales similarly with changing volume fraction. They postulate that five-armed NSs form a frustrated network due to the inherent asymmetry of the NS (as opposed to the symmetry in NSs with four and six arms) which causes five-armed NSs to deviate from the trends observed with valency [57].

1.2.2   Nanostar history

The concept for a NS was developed by Ned Seeman, who has been credited as being the founding father of DNA nanotechnology [58, 59]. Seeman was interested in creating ordered lattices out of DNA [58, 60]. The first NS design was based on Holliday junctions, transient branched structures that occur during genetic recombination [61]. These NSs, referred to as nucleic acid junctions at the time, were four-armed structures that lacked unpaired bases in the junction. Preliminary work showed that with this design, all bases in the core are paired in the presence of Mg^{2+} and that the junction is stable if specific design principles are followed [46, 62, 63].

Seeman and colleagues went on to construct and characterize NSs with up to twelve arms [64]. They examined the loops formed by NSs with overhangs on two arms and concluded that individual NSs are too flexible to create ordered lattices [61, 65]. They determined that the angle between the arms varied because the loops varied in size (i.e., the arc per NS varied). From this result, in combination with Förster resonance energy transfer results, Seeman concluded that the angle between arms on a four armed NS could vary up to 30° from the average angle [61, 65]. (Using the design principles developed with NSs and knowledge of the flexibility of the junction, Seeman and others created ordered lattices using 3D DNA structures and other, stiffer, designs [60, 63].)

Following this, DNA NSs have been used to create hydrogels [48, 66]. In some of these works, three and four armed NSs, referred to as dendrimer-like DNA or (X-, Y-, or T-)DNA, were covalently bonded via enzymatic ligation to produce a stable gel that can be dehydrated and resuspended and persists for weeks [48]. Similarly, NS hydrogels connected via i-motifs have been shown to persist over several days at a low pH, but when the pH is raised, the gel dissolves within minutes [66]. Hydrogels that form through the hybridization of long sticky ends have exhibited reversible temperature- and

pH-dependent viscoelastic responses and have been used to confine cells [53, 54, 67, 68]. Finally, NSs with short sticky ends have been shown to form an "equilibrium gel" when prepared at a high concentration of NSs and low temperature [50, 69]. In the equilibrium gel state, the dense phase spans the sample and NSs are tightly interconnected such that NS relaxation is slow compared to the lifetime of the experiment ($\approx$ 10 seconds) [70]. Using DLS, Biffi et al. (2015), established that this state is in equilibrium (as opposed to a metastable state) by showing that the final state is the same regardless of cooling rate [50].

The Sciortino group carried out pioneering works that give insight into NS network structure and dynamics. They show that NSs within equilibrium gels have slower dynamics at higher salt and lower temperature [50, 69, 71]. In these works, they conclude that NS dynamics are well described by Arrhenius behavior [34]. Additionally, they determine that NSs in the dense phase are fully bonded and further supported this conclusion by showing that a network that has a fraction of overhangs unbound is more dynamic than its fully-bound counterpart [34, 52]. Other works have focused on applications of DNA gels. For example, covalently linked hydrogels have been used to detect proteins and can enhance *in vitro* transcription rates [38, 72]. Additionally, functionalized NS hydrogels have been used to target cancer cells to deliver anti-cancer medicine in mice and have been shown to inhibit growth of some cancer cells [40, 53, 73, 74].

Biffi et al. (2013) was the first work to examine LLPS of NSs [34]. They used DLS and absorbance spectroscopy to measure the NS phase diagram and observed a critical slowing down of NSs as the temperature was lowered to the critical temperature of phase separation [34]. The temperature dependence of NS rearrangement just above the critical temperature is well-described by an Arrhenius equation with an activation energy equal to the free energy of binding of one to two overhangs. Arrhenius behavior of NSs within the dense phase has been further confirmed by monovalent salt assays and rheology

experiments (See Chapter 3 and Refs. [57, 69]). However, other properties beyond inter-NS binding, such as intra-NS electrostatic repulsion and/or NS flexibility, have been shown to impact NS behavior [41, 43]. NS liquid drops have been used to mimic some aspects of intracellular phase separation like coexisting phase separated drops that remain immiscible [26, 27]; selective cargo partitioning [26, 27, 75]; and size-limited growth [7].

1.3   Dissertation Overview

In this dissertation, I examine the LLPS of a model system composed of a single component: DNA nanostars (NSs). I calculate the thermodynamics of inter-NS interactions to isolate which attributes of NS LLPS depend on inter-NS interactions and postulate other molecular-level properties that play a role. In Chapter 2, I provide a general background of dense DNA phases and describe models that are used to describe LLPS.

I characterize the effects of salt concentration on bulk NS liquid properties in Chapter 3 [41]. I compare the thermodynamics of inter-NS interactions to trends in density, viscosity, NS diffusivity, and surface tension of NS-liquid droplets as the concentration of monovalent salt was changed. I attribute an increase in the viscosity and decrease in diffusivity with increasing salt to the sequence- and salt-dependent thermodynamics of base pairing. Thus, I show that the transport properties of the liquid are dependent on an Arrhenius process with a single NS bond as the activation barrier. However, other properties cannot be connected to NS binding thermodynamics. Instead, I relate the increase in NS concentration within the dense phase and increase in surface tension to electrostatic screening between arms within the same NS, which allows them to take on more compact shapes. Finally, I conclude that the interior of the NS liquid is heterogeneous: it is composed of highly-connected clusters that are loosely linked together.

In Chapter 4, I turn to the thermodynamic principles that dictate solute partitioning

into NS droplets [75]. I show that the partitioning of solutes that do not interact with NSs can be used to determine the size of the meshwork in the DNA-rich phase. In addition, I examine the partitioning of long dsDNA "linkers" that include sticky ends. I find that linker partitioning is length-dependent because of a confinement penalty of inserting long strands within the liquid's characteristic mesh size. I quantify this entropic-confinement effect using a simple partitioning theory and show that its magnitude is consistent with classic Odijk pictures of confined worm-like chains [76]. Linkers with sticky ends sometimes exhibit inhomogeneous structures: long linkers are excluded from the liquid interior and tend to preferentially accumulate on the surface of the droplets, and long linkers that are forced into the NS liquid undergo a secondary phase separation, forming metastable droplet-in-droplet structures.

In Chapter 5, I describe the phase behavior of NSs when combined with a flexible, positively charged amino acid chain, poly L-lysine (PLL) and examine the interplay between NS–NS and NS–PLL interactions in dictating phase behavior. Without NS–NS interactions, I show that NSs and PLL condense into liquid droplets at low salts but do not phase separate at intermediate salts. When NS–NS base pairing is incorporated, NSs and PLL form gel-like structures and liquid drops at low salts and intermediate salts, respectively. At high salt concentration, base pairing NSs form drops that exclude PLL. Like NS-only droplets, PLL-excluded NS-droplets dissolve at high temperatures; however, NS–PLL structures are stable at high temperature. Finally, I show that orthogonal NSs form separated droplets with PLL in both droplet types, but base-pairing NSs, non-base pairing NSs, and PLL form three-component droplets. These results indicate that despite having opposing responses to changing salt concentration, NS–NS base pairing and NS–PLL electrostatic attractions both dictate phase behavior because they are both similar to $k_B T$.

This dissertation shows that NSs create a local environment that has comparable

physical properties to biomolecular condensates. These liquid drops exhibit similar controlled partitioning to biomolecular condensates where larger molecules are excluded, but incorporating attractions between the solute and the components of the droplet can drive partitioning of molecules that would otherwise be excluded. Additionally, when combined with PLL, phase behavior is dependent on attractive interactions between molecules of the same species (NS–NS interactions) and molecules of different species (NS–PLL). Protein-based condensates have shown similar phase behavior that depends on same-species and inter-species attractions. Overall, this dissertation shows that NS liquids can model several aspects of biomolecular condensation and may prove to be a valuable model system for isolating the individual underlying principles that dictate intracellular phase behavior.

Chapter 2

Relevant Background

2.1 DNA disordered phases[1]

Nano-sized DNA molecules have been used to create disordered phases — dense, unstructured, aqueous assemblies of DNA that span regions much larger than the particles of which they are composed [77]. Materials are considered *ordered* if the constituent particles are organized into regular arrays, or lattices, over long length scales and *disordered* if the particles lack such regular, long-range organization (Fig. 2.1) [78, 79]. Order can be *positional*, *orientational*, or a combination of the two.

DNA-based disordered materials have been used to study phase transitions [34, 47, 69], as a model for self-assembled structures that are pervasive throughout biology [37, 41, 80], and as sensors for a variety of materials including heavy metals and biomolecules [35, 81, 82, 83]. Compared to other types of macromolecules, e.g., synthetic polymers, DNA offers several unique and exploitable features that aid in the creation of disordered phases: The programmable nature of Watson-Crick-Franklin base pairing permits con-

---

[1]This section is replicated from a textbook in preparation that is the result of a collaboration with Dr. Omar A. Saleh. It is included here to provide context for NS liquids in the broader field of DNA disordered phases.
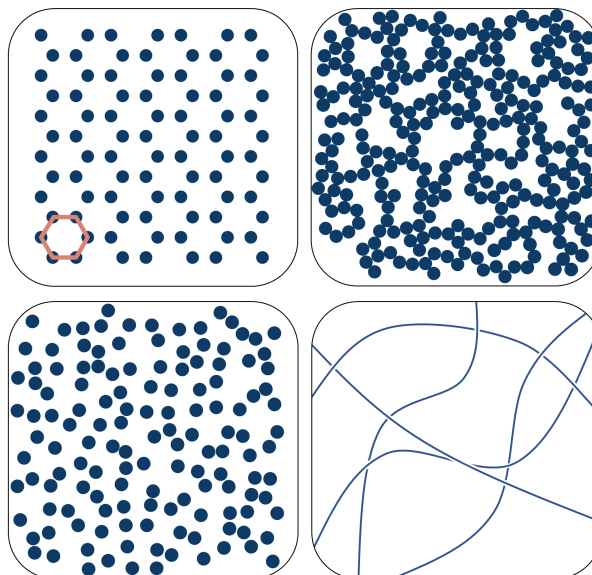
Figure 2.1: **Positional order** The top left panel shows an *ordered lattice*, an arrangement with high positional order that is made up of a repeating configuration of particles which persists for large length scales, as in a crystal. Notice that the hexagon drawn in the bottom left corner can be moved throughout the system and still represent the lattice equally well. The top right panel and bottom left panel show a cross-linked hydrogel of colloids and a liquid composed of colloids, respectively, which have low positional order, as are created by branched DNA particles. The bottom right panel shows disordered, entangled polymers, which can make up a gel or a liquid depending on the interaction strength between the DNA particles.

trolled, rational design of particle shape and inter-particle interactions. Further, the rigid-rod nature of duplex DNA tends to lead to condensed phases with large pore sizes and high-water content, which enables infusion of other molecules into the material [36, 54, 67]. Finally, functionalization of the dense phase is straightforward, both because DNA has a variety of well-understood sequence-specific interactions with other DNA strands, RNA, and proteins, and because DNA is relatively easy to label with various chemical groups such as biotin and fluorophores [53, 84, 85].

The specific structure and behavior of the DNA particles affects the type of disordered phase that is created (See Fig. 2.4). Below is a non-exhaustive list of disordered phases that can be created with DNA.

1. **DNA liquids:** Formally, a liquid phase is a condensed material that, under slowly-applied stress, exhibits a viscous, dissipative response[2] [86, 87]. Such a response requires a delicate balance of inter-particle interactions: there must be attractions that drive condensation, but those attractions must be weak and transient to enable liquid-like dynamics. The temporary nature of the interactions creates order over length scales of a few particle sizes at best with the material otherwise being disordered [78, 79]. To create macromolecular liquids, including DNA liquids, recent work has argued that the constituent particles must have relatively few binding interactions ('finite valence') and a high degree of internal flexibility [70]. In line with these considerations, DNA liquids have been created using particles that contain significant intra-particle configurational freedom and that bind to each other through multiple, but weak, base pairing sites [34, 88].

2. **DNA hydrogels:** Hydrogels are typically an elastic material – they resist small deforming forces by generating a restoring force. The energy is released when the stress is removed, allowing the material to snap back to its original shape[2] [86]. Hydrogels are composed of a network of crosslinked particles that are kinetically trapped [86, 89]; that is, the constituent particles cannot rearrange due to strong attractive interactions with neighboring particles [47, 50, 69]. DNA hydrogels have generally been created using multivalent particles with long-lived, base pairing interactions [48, 50, 90].

---

[2]In simple schemes, a material's response to stress is expected to be elastic or viscous. However, soft, disordered materials typically exhibit a combination of viscous and elastic behaviors depending on the force applied and the timescales considered [91, 92]. Such viscoelasticity is a pervasive property of DNA materials due to the slow relaxation times of the system caused by base pairing, entanglement, and other interactions [41, 71, 90, 93]. Viscoelastic behavior is often characterized using rheology or microrheology (See Chapter 3.) [41, 54, 57]. Here, we refer to gels as materials in which the predominate reaction to stress is elastic, and the time scale of particle rearrangement is long compared to the time scale of the experiment. We refer to liquids as materials where the predominant reaction to stress is viscous, and the particle relaxation time is short compared to the time scale of the experiment [70].
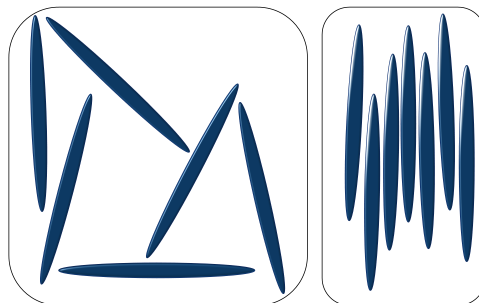
Figure 2.2: **Orientational order** Particles that are longer than they are wide are anisotropic. To the left, anisotropic particles cannot rearrange easily because they are not aligned. On the right, the particles have orientational order and can pack closer together while still sliding past each other, as occurs in liquid crystals. The arrangement in the diagram is an example of a nematic liquid crystal.

3. **DNA liquid crystals:** Liquid crystals are an intermediate phase between fully random liquids and fully ordered crystals. In this state, the particles exhibit some type of crystal-like ordering, while still retaining a liquid-like ability to rearrange [86, 94]. One way in which this can occur is if the particles are rod-like — that is, long, slender, and relatively rigid. Such rod-like particles become trapped and lose translational entropy when forced to pack closely in a disordered state, whereas rods that bundle together in an aligned state retain translational entropy, since they can slide past each other, despite packing tightly [95]. There are multiple types of liquid crystals, which are categorized by the orientation of the particles, the types of symmetry present, and the number of dimensions of the liquid crystal. One example of a DNA-based liquid crystalline phase is the nematic phase, which can be made up of dsDNA [96, 97, 98] or with self-assembled DNA structures that form rods on larger length scales [99, 100]. DNA has also been used to make other liquid crystalline structures, as described in Refs. [77, 101, 102].

2.1.1   Creating DNA disordered phases

DNA disordered phases are often highly concentrated in DNA — for example Zanchetta et. al measured the concentration of DNA in some liquid crystals to surpass 1000 mg/mL [103]. (Taking the mass density of dsDNA to be 1700 mg/mL, a solution concentration of DNA of 1000 mg/mL corresponds to a volume fraction of about 60% [104].) To condense into such a concentrated material, the individual particles must overcome the large electrostatic repulsion that occurs between the highly negatively charged DNA backbones. This typically requires a relatively high concentration of cations in solution (e.g., salt), which weaken (screen) backbone-backbone repulsions [41, 69, 100, 105]. Alternatively, multivalent cations have been shown to drive condensation. For example, long, linear DNA condenses when combined with small, multivalent cations like spermidine (+3) and spermine (+4) [106, 107]. DNA can also form 'complex coacervates,' dense, liquid droplets or gel-like aggregates that condense via the electrostatic attraction between negatively and positively charged polymers [2, 80, 108]. An alternative approach of overcoming DNA–DNA repulsion is to use uncharged polymers, such as PEG and methylcellulose, which act as depletion agents to force large DNA molecules together [99, 102, 103]. Finally, some works have used a solvent where DNA solubility is reduced to promote condensation [102, 109].

Phase separation that occurs due to polycations, depletion agents, or DNA-insoluble solvent is a non-specific process: phase separation is promoted regardless of the sequence of the DNA molecules. Better control of inter-particle attractions can be achieved using sequence-specific interactions, notably base pairing interactions. By tuning the sequence, base pairing interactions can be made strong enough to overcome electrostatic repulsion and drive condensation, which is often seen in DNA liquids and hydrogels. The resulting condensed DNA phases can then be classified as entangled or unentangled:

- **Entangled systems** are composed of linear DNA that form polymer networks. This includes plasmid-length, ssDNA that contains long, repeating complementary sequences that hybridize to condense into a hydrogel [90, 105, 110]. Similarly, single strands containing multiple repeats of a short, partially palindromic sequence, such as $[CTG]_n$, can form DNA liquids via inter-strand hybridization of the partially palindromic sequences, while flexibility is ensured by the nucleotides that remain single stranded [88].

- DNA particles in **unentangled systems** behave like colloids such that each particle has its own volume that other DNA particles cannot penetrate. A prominent example of an unentangled, base pairing system is the DNA 'nanostar' system, a star-shaped design in which each DNA particle has several (typically 3–4) double-stranded arms that meet at a highly flexible junction (Fig. 2.3) [34, 41, 85]. DNA nanostars can form liquids or hydrogels via binding of a short palindromic sequence on the tip of each arm [47, 50, 54]. The phase behavior of nanostars is dependent on the strength of the inter-particle base pairing, where weaker interactions form colloidal liquids and stronger interactions — including covalently bonded nanostars — form colloidal hydrogels [47, 48].

Figure 2.3: The DNA nanostar is a branched DNA particle with arms that end in single stranded, palindromic sequences.

Most DNA liquid crystal works take advantage of the stiff-nature of dsDNA [96, 111, 112]: it can be considered rod-like for lengths shorter than 50 nm [113]. In fact, several recent studies have focused on the liquid crystalline behavior of very short (4 to 20 base pair) dsDNAs [97, 103, 114]. Highly concentrated, ultra-short DNA exhibits diverse phase behaviors that are dependent on DNA length, sequence, and end-to-end base stacking [98, 115]. Alternatively, DNA origami has been used to create liquid crystals out of much longer DNA structures, such as DNA nanotubes, which are rod-like on length scales of a few microns [116]. DNA nanotubes have been used to investigate the effects of inter-molecular interactions that cannot be probed with traditional dsDNA; for example, the effects of altering the helical nature of the rods on liquid crystalline phase behavior [99, 100].

2.1.2   Characterizing disordered phases

Each disordered phase exhibits a unique set of properties including DNA particle assembly and rearrangement. The individual particles are too small to view via optical microscopy. Nonetheless, the differences of each material become obvious when bulk phases of fluorescently tagged DNA are visualized (Fig. 2.4).

For example, the particles within DNA liquids can rearrange and relax resulting in a homogeneous material that exhibits a surface tension; thus, they typically appear as constant intensity, round drops in optical microscopy (Fig. 2.4). A way to demonstrate a material's liquid-like nature is to observe a structure as it relaxes into a spherical droplet — either by perturbing an existing drop into a non-spherical shape or by tracking two drops as they coalesce into one [41]. One can measure the internal time scale of particle rearrangement in a liquid using fluorescence recovery after photobleaching (FRAP), a procedure in which one tracks the return of fluorescent DNA particles as they diffuse into
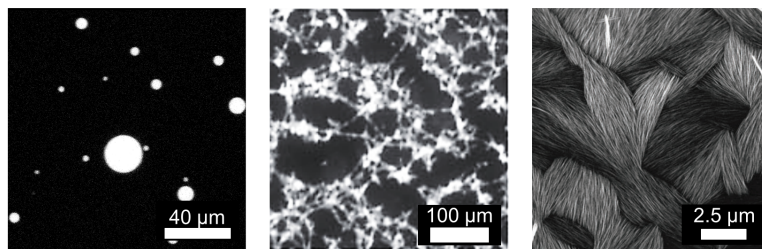
Figure 2.4: On the left, branched DNA particles, DNA nanostars, can rearrange due to their weak interactions and form liquid droplets which round into spheres. In the middle, DNA nanostars with stronger interactions are kinetically trapped and form a DNA hydrogel that spans the sample. On the right, long DNA nanotubes form liquid crystals which are visible as regions of aligned fibers. Left and middle images are reproduced from Ref. [47] and right image is reproduced from Ref. [99] with permission from the Royal Society of Chemistry.

a small region of non-fluorescent DNA [41, 88, 117]. Additionally, the viscoelastic nature of DNA liquids has been probed using rheological methods [41, 57]. A final important property for liquids is the phase diagram — i.e., the set of conditions where a DNA-dense liquid phase coexists with a DNA-dilute phase versus when the system remains homogeneously mixed. Phase diagram measurements require careful determination of the concentrations of dense and dilute phases across a range of conditions (such as different temperatures or salt concentrations) [34, 41, 42, 43].

DNA hydrogels resemble sponges under a microscope — i.e., irregularly-shaped fragments consisting of dense gel regions interspersed by dilute-phase pores of various sizes (Fig. 2.4) [47, 48]. Because hydrogels have long-lasting interparticle interactions, which prevent significant rearrangement over the lifetime of the experiment, their nanoscale structure can be studied directly. For example, atomic force microscopy and electron microscopy have been used to achieve sub-optical resolution of the arrangement of DNA particles within hydrogels [48, 53, 90]. Dynamic light scattering (DLS) has been used to characterize the size of gel clusters [51, 69], and rheological methods have been used to probe the viscoelastic properties of hydrogels [54, 67, 85].

20

DNA liquid crystals can form droplets, similar to DNA liquids; however, the condensates can be non-spherical because liquid crystals exhibit anisotropic surface tensions [98, 118]. When large DNA particles, like DNA nanotubes, are used to make up the crystal, the alignment of individual fibers are directly visible using fluorescence imaging (Fig. 2.4) [99, 100]. Regardless of the particle size, placing polarizers in the light path will confirm the partial ordering of the material. This is because the way that polarized light travels through liquid crystals changes based on the orientation of the light with respect to the orientation of the DNA particles. The specific pattern of light and dark bands gives information about the type of liquid crystal [96, 98, 102, 114, 115]. X-ray scattering and electron microscopy have also been used to examine the interior structure within DNA liquid crystals [93, 100, 102, 112].

2.1.3   Summary of disordered phase behavior

DNA particles have been used to create hydrogels, liquids, and liquid crystals. The shape of the DNA particles and interactions between them are vital in determining which disordered phase they will form. DNA liquid crystals are not crosslinked but can form when, e.g., rod-shaped DNA particles align to allow for denser packing. Both DNA hydrogels and DNA liquids are crosslinked, but the particles that make up DNA hydrogels are kinetically arrested due to strong interactions, while the particles that make up DNA liquids can rearrange easily due to weak interactions.

2.2   Introduction to phase separation

As this thesis focuses on liquid-like DNA phases, here, I provide a general introduction into liquid-liquid phase separation (LLPS). LLPS is a type of coacervation — the process by which regions that are dense in macromolecules demix from regions that are dilute

in macromolecules [1]. Coacervation can occur with a single species of macromolecule (simple coacervation, as in the case with NSs) or with multiple macromolecules (complex coacervation). In addition, coacervates can either be liquid-like or gel-like, but LLPS specifically creates two liquid phases. LLPS occurs when the free energy of two coexisting phases is less than the free energy of a homogeneously mixed system [113, 119, 120]. A system's phase behavior depends on a wide variety of factors including the length, valency, and stiffness of the macromolecule(s) [14].
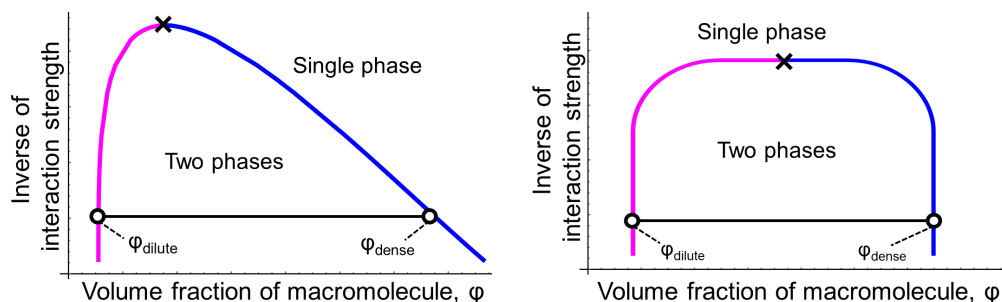
Figure 2.5: Representative phase diagrams for complex coacervation (left) and NS phase separation (right). The pink and blue lines show the volume fraction of the macromolecule in the dilute and dense phase, respectively. The × represents the critical point and the circles indicate the concentration of coexisting dense and dilute phases.

Equilibrium phase behavior is quantified using a phase diagram (Fig. 2.5). Phase diagrams that consider a single component generally have a y-axis that is related to the strength of interactions between molecules (e.g., salt [119] or temperature [34].) The x-axis is generally related to the concentration of a single macromolecular species and is often described using the unitless volume fraction, ϕ, defined as the fraction of the total volume that is taken up by the macromolecule. Phase separating systems often take on an umbrella-like curve (known as a consolution curve, coexistence curve, or binodal) which can face up or down depending on the system and axes used [14]. Within the binodal, a system will phase separate into two phases with volume fractions ϕ_{dense} and

ϕ_{dilute} but will form a homogeneously mixed solution when the system is outside of the binodal. The lines that connect the concentrations of coexisting dense and dilute phases are known as tie lines and can either be horizontal (Fig. 2.5) or have a slope depending on the definition of the y-axis and state of the system. The point at which the interactions are weakest, but phase separation still occurs is known as the critical point, which is used to characterize the robustness of a phase separating system [16].

There are two typical processes that lead to phase separation: spinodal decomposition and nucleation and growth. In each of these, the kinetics of phase separation are different, but the final product is the same. Nucleation and growth occurs when the homogeneously mixed state is metastable, so larger fluctuations are necessary for phase separation to begin. This leads to a delay in phase separation to allow for small (nucleation) points to form and grow by collecting material from the nearby solution. Spinodal decomposition occurs when the homogeneously mixed state is unstable. Thus, phase separation via spinodal decomposition is spontaneous because there is no energetic barrier to the demixed state. It is difficult to determine if a system is undergoing spinodal decomposition or nucleation and growth using optical microscopy because nucleation points are smaller than the resolution of a microscope, but recent work has shown that NS drops form instantly at a high salt and NS concentration, supporting a transition into the spinodal decomposition regime [121].

Several theories have been created to predict when a system will phase separate. Some are outlined below: (1) The Flory-Huggins model approximates the change in free energy from two liquids mixing and is often the basis for the entropy of mixing for other models; however, it does not specify the types of interactions between components [122, 123]. (2) The Voorn-Overbeek model expands upon the Flory-Huggins model to describe electrostatically-driven condensation; thus, it is relevant for the polylysine-NS mixtures explored in Chapter 5 [124]. (3) Wertheim's Thermodynamic Perturbation
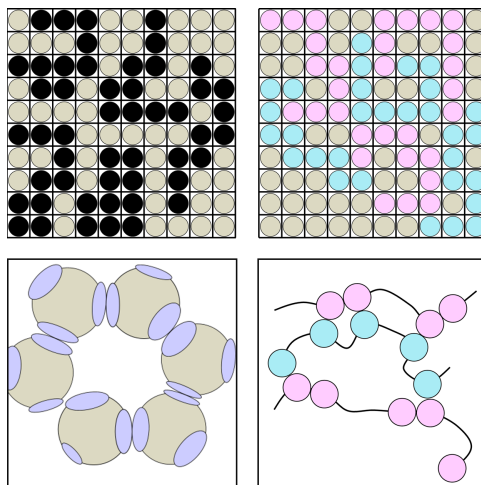
Figure 2.6: (Top left) Flory-Huggins theory assigns monomers (black) and small molecules (tan) to a lattice. In this example, only entropy is considered; there are no interactions between lattice sites. (Top right) The Voorn-Overbeek model also assigns molecules to a lattice and incorporates attractive interactions between positively charged monomers (pink) and negatively charged monomers (blue). (Bottom left) Wertheim's perturbation theory considers a limited number of attractive interactions on colloidal molecules. (Bottom right) The sticker-spacer model includes attractive stickers (pink and blue) connected by non-interacting spacers (black line).

Theory (TPT) can be used to describe demixing of colloids with a limited number of anisotropic interactions, like NSs [125, 126].

2.2.1   Flory-Huggins

The Flory-Huggins (FH) theory describes the conditions in which two liquids will mix. It separates the entropic and enthalpic free energy contributions of mixing and uses mean field theory to determine each individually [122, 123]. The FH model assigns the individual monomers of a linear polymer and small molecules (i.e., solvent or salt ions) to n_{tot} individual lattice sites of the same size (Fig. 2.6) [16, 113]. Entropy favors mixing because more lattice sites are accessible to each molecule when the two systems are well-mixed rather than when each molecule is confined to a subset of the lattice sites, as is the case for the demixed state. The FH model predicts that phase separation occurs

when pair-wise attractions counter entropy-promoted mixing; however it does not specify the type of interactions that occur.

The FH equation describes the change in free energy per lattice (in units $k_B T$) of going from a perfectly demixed system to a perfectly (homogeneously) mixed system:

$$\Delta F_{mixing} = \sum_{i=1}^{m} \frac{\phi_i}{N_i} \ln \phi_i + \sum_{i=1}^{m} \sum_{j>i}^{m} \phi_i \phi_j \chi_{i,j} \tag{2.1}$$

where m is the number of species including macromolecules and small molecules. The first term, the entropy of mixing, depends on N_i, the length of species i (taken to be 1 for small molecules), and ϕ_i, the volume fraction of species i, which given by $\phi_i = \frac{n_i}{n_{tot}}$ where n_i is the number of lattice sites taken up by species i. The second term, the enthalpy of mixing, depends on $\chi_{i,j}$, which is the Flory interaction parameter that characterizes the change in interaction energy upon mixing:

$$\chi_{i,j} = \frac{z}{k_B T} (u_{i,j} - \frac{1}{2}(u_{i,i} + u_{j,j})). \tag{2.2}$$

where z is the valence of each lattice site and $u_{i,j}$ describes the energy of a single interaction between species i and j.

In reality, when a system phase separates, it is neither perfectly mixed nor unmixed; there is always (at least) a small amount of each component in each phase. The free energy of mixing, $F(\phi)$, can be used to predict the phase boundary (Fig. 2.7). Because the system is in equilibrium, the chemical potential, or the free energy contribution per particle, of each species must be the same in both phases. This equilibrium condition can be used to define the common tangent rule: the free energy of a phase separated system lies on the line, $f(\phi)$, that connects two points on the free energy curve that share the
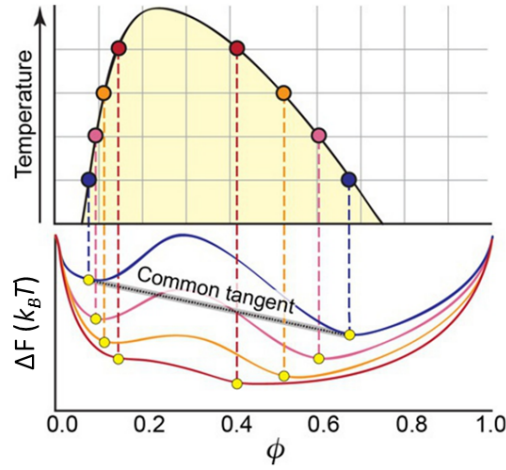
Figure 2.7: Binodal of a phase separating system (top) mapped onto the free energy curves, $F(\phi)$ (bottom). Each line color represents the free energy cure at different temperatures and the yellow dots correspond to points with equivalent slopes, at ϕ_{dense} and ϕ_{dilute}. Reprinted from *Methods in Enzymology*, Volume 611, Ammon E. Posey, Alex S. Holehouse, and Rohit V. Pappu, *Chapter One - Phase Separation of Intrinsically Disordered Proteins*, pages 1-30, (2018), with permission from Elsevier [127].

same slope. $f(\phi)$ can be calculated by

$$\left.\frac{\partial F}{\partial \phi_i}\right|_{\phi_i = \phi_i^{dense}} = \left.\frac{\partial F}{\partial \phi_i}\right|_{\phi_i = \phi_i^{dilute}} = \frac{F(\phi_i^{dense}) - F(\phi_i^{dilute})}{\phi_i^{dense} - \phi_i^{dilute}} \tag{2.3}$$

where each expression of Eq. 2.3 gives the slope of $f(\phi_i)$ that must pass through both points ϕ_i^{dilute} and ϕ_i^{dense} (Fig. 2.7). The FH model predicts that a system will phase separate if the free energy of the tangential line at the bulk concentration, ϕ_0, is less than the well-mixed free energy, i.e., $f(\phi_0) < F_{mixing}(\phi_0)$.

The lever rule can be used to calculate the volume of each phase, or V_{dense} and V_{dilute}, expressed in terms of the fraction of volume taken up by each phase (*not* volume fraction of a species), or $\nu^I = \frac{V_I}{V_{tot}}$ where I can be the dense or dilute phase. The fraction of volume occupied by each phase depends on the difference between the bulk volume fraction and

the volume fraction in the opposite phase, e.g., for phases I and II,

$$\nu^I = \left| \frac{\phi^{II} - \phi_0}{\phi^I - \phi^{II}} \right| \tag{2.4}$$

where ϕ^I is the volume fraction of a component in phase I. Thus, the total free energy of a phase separated system is

$$F^{I,II} = \nu^I \phi^I + \nu^{II} \phi^{II} \tag{2.5}$$

In addition to the phase boundary, the free energy curve can be used to calculate the critical point, which occurs when $\frac{\partial^3 F}{\partial \phi^3} = \frac{\partial^2 F}{\partial \phi^2} = 0$. Finally, the FH model can be used to predict if the system will undergo spinodal decomposition or nucleation and growth. A system undergoes spinodal decomposition if the bulk concentration is between the inflection points of the free energy curve, i.e., between the two points when $\frac{\partial^2 F}{\partial \phi_{poly}^2} = 0$. If the bulk concentration is between the binodal point and the spinodal points, the system undergoes nucleation and growth (Fig. 2.8) [16].
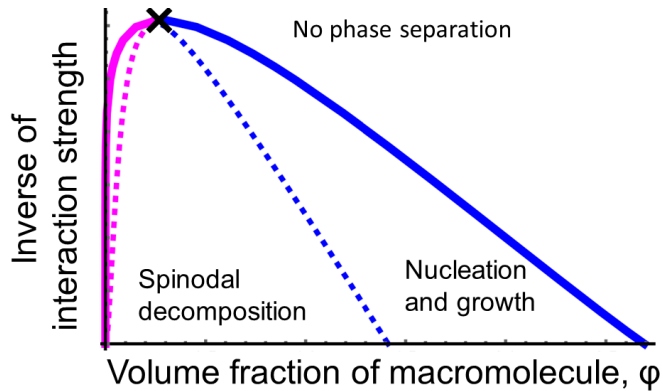

Figure 2.8: Spinodal decomposition occurs if the bulk concentration is between the two dashed lines. Nucleation and growth occurs if the bulk concentration is between the dashed and the solid lines.

2.2.2 Voorn-Overbeek

Voorn-Overbeek (1957) created the first theoretical description of electrostatically-driven complex coacervation of two oppositely charged polymers (Fig. 2.6) [124]. They expanded upon the FH model by separating the change in enthalpy of mixing into an electrostatic term and a non-electrostatic term (which they neglected, but other authors have since included [14, 119, 128]). The Voorn-Overbeek model uses the Debye-Hückel theory to describe the electrostatic free energy of solution:

$$F_{ele} = -\frac{q^2}{3\epsilon}\kappa N_z \tag{2.6}$$

where q is the elementary charge, ϵ is the dielectric constant, κ is the Debye length, $\kappa^2 = \frac{4\pi q^2 N_z}{\epsilon k_B T V_{tot}}$, and N_z is the total number of electrostatic charges.

This can be rewritten as the electrostatic free energy per lattice site (in units $k_B T$):

$$F_{ele} = -\alpha \left(\sum_{i=1}^{m} \sigma_i \phi_i \right)^{3/2} \tag{2.7}$$

with α given by

$$\alpha = \frac{2}{3}\sqrt{\pi} \left(\frac{l_B}{l_0} \right)^{3/2} \tag{2.8}$$

where l_B is the Bjerrum length (the distance where the electrostatic interaction between two charges is equal to the thermal energy scale, often taken to be 0.7 nm in water), and l_0 is the length of a lattice site.

The Voorn-Overbeek theory has been used to model the phase separation of flexible, equal length polymers with high charge density, which were mixed at equal stoichiometry [119]. This work exemplifies a few tricks that can be used with the Voorn-Overbeek model. First, in the high salt limit ([monovalent salt] > 50 mM), the salt concentration is

approximately constant in all phases; thus, the salt's contribution to the entropic term can be ignored. In addition, complex coacervates are charge neutral, so the volume fraction of equal length, flexible polymers with equal charge density in the dense phase must be equal [129]. These assumptions allows one to solve for a single variable $\phi_{poly} = \phi_{polycat} + \phi_{polyan}$ when solving for the phase boundary [119].

2.2.3   Wertheim's Thermodynamic Perturbation Theory

Wertheim's Thermodynamic Perturbation Theory (TPT), also known as the Statistical Associating Fluid Theory (SAFT), has been used to describe the phase separation of NSs [42, 56, 130]. TPT calculates the free energy of a system with a limited number of directional interaction sites (patches) (Fig. 2.6). Each site is limited to a single interaction with a site on another particle [131]. The free energy of the target system (e.g., NSs with sticky ends) is described as a perturbation to a well-characterized reference fluid — taken to be a system of NSs without base pairing interactions. The free energy per particle of the reference fluid, f_{ref} is described as an ideal gas of hard spheres with pair-wise interactions defined by the second virial coefficient, $B_2^{i,j}$:

$$f_{ref} = \frac{F_{ref}}{n} = \sum_{i=1}^{m} \phi_i \ln \phi_i + \ln c_{tot} - 1 + \sum_{i=1}^{m} \sum_{j \geq i}^{m} \frac{c_i c_j}{c_{tot}} B_2^{i,j}(T) \qquad (2.9)$$

where n is the number of particles, ϕ_i is the same volume fraction as in the FH theory, c_i is the number density of species i, and c_{tot} is the total number density of all species. The first term is the same entropy of mixing from FH theory; the second and third terms incorporate excluded volume interactions; and the fourth term describes the pair-wise interactions between blunt NSs (including electrostatic repulsion between backbones) that has been found using simulations [130].

Incorporating attractive patches (NS–NS binding sites) onto each particle perturbs

the system from the reference fluid, $f = f_{ref} + f_{bind}$. The free energy contribution from NS–NS binding depends on the probability of an arm being bound, p_b:

$$f_{bind} = zc_{tot} \ln(1 - p_b) + \frac{1}{2}zc_{tot}p_b \tag{2.10}$$

where z is the valency of a NS and zc_{tot} is the number density of NS arms. Eq. 2.10 shows that the free energy contribution of an unbound arm is dominated by entropy while the free energy of a bound arm is dominated by enthalpy. The probability of binding is calculated using the law of mass action and assuming Arrhenius behavior:

$$k = \frac{[products]}{[reactants]} = \frac{c_{ds}}{c_{ss}^2} = ce^{\Delta G/k_B T} \tag{2.11}$$

where the c_{ds} is the number density of the product, dsDNA; the denominator, c_{ss}^2, is squared because two single strands are required to form a double strand; and ΔG is the free energy of DNA hybridization, as calculated by SantaLucia (2004) (See Section 2.3.) [132]. Eq. 2.11 assumes a system composed of only one species of NS, but previous work has accounted for combining species of multiple valencies [130].

Wertheim TPT has been used to describe the growth in the phase boundary for NSs with increasing valence and salt concentration [130, 133] and the formation of a percolating equilibrium gel phase in the dense phase [133]; however, for many of these works, the quantitative values deviate from experimental results. For example, Conrad (2022) showed that the phase boundaries are similar for a four-armed and five-armed NS, but TPT predicts a consistent increase with increasing valence [42, 57, 134].

2.2.4   Other models

Other models have been used to describe protein-based phase separation. These models can account for some factors that mean-field-based models, like FH theory and the Voorn-Overbeek approximation, cannot. For example, mean field models treat all monomers equally (e.g., if only a subset of monomers are charged, the charges are randomly assigned on the polymer); however, recent works have shown that charge patterning impacts phase behavior, not just the fraction of charged molecules [135, 136, 137]. Other models, like the sticker-spacer model and Random Phase Approximation (RPA), are able to account for the distribution of charge along a polymer (Fig. 2.6) [135, 138, 139]. In the sticker-spacer model, the attractive interactions, "stickers," are spaced along a linear chain and are separated by non-interacting monomers, or "spacers," based on the polymer that they are modeling [135, 140]. RPA considers fluctuations in the concentration of charges in solution due to the charges on the polymer when predicting phase behavior [141, 142]. RPA has also been used to describe the arrangement of NSs in the dense and dilute phase [143].

2.3   SantaLucia model of DNA hybridization

The NSs used throughout this dissertation generally interact via hybridization of sticky ends. Thus, it is necessary to understand the free energy of DNA hybridization to describe the behavior of NSs within the dense phase. The thermodynamics of DNA hybridization is dependent on a variety of interactions beyond Watson-Crick-Franklin base pairing (e.g., base-stacking between neighboring bases and hydrophobic interactions between the bases and surrounding solution) [132]. Rather than isolate the effects of each interaction, SantaLucia (1998) created a phenomenological model that is commonly used to calculate the free energy associated with the binding of a given DNA sequence.

This unified model uses nearest-neighbor parameters to determine the thermodynamics of DNA hybridization as they relate to salt concentration, temperature, and DNA length [132, 144]. The model accounts for each pair of base pairs, $\Delta G_{i,i+1}$; the effects of the outer-most base pairs, ΔG_{int}; and the effects of having a symmetric sequence, ΔG_{symm}:

$$\Delta G_{hybrid} = \sum_{i=1}^{N-1} (\Delta G_{i,i+1}) + \Delta G_{int} + \Delta G_{symm} \qquad (2.12)$$

where N is half the number of phosphates in the hybridized structure. The values for $\Delta G_{i,i+1}$ at 1 M NaCl and 37 °C are given in Ref. [132]. To calculate ΔG_{hybrid} at another temperature, the free energy must be adjusted by

$$\Delta G_{hybrid} = \Delta H_{hybrid} - T\Delta S_{hybrid} \qquad (2.13)$$

where ΔH_{hybrid} is the enthalpy of binding and ΔS_{hybrid} is the entropy of binding, both given in Ref. [132]. Additionally, to calculate ΔG_{hybrid} at a monovalent salt concentration that is not 1 M NaCl, the free energy must be adjusted by

$$\Delta G(C_{Na^+}) = \Delta G(1\ M\ Na^+) - 0.114N \times ln(C_{Na^+}) \qquad (2.14)$$

where C_{Na^+} refers to the molar concentration of sodium ions in solution, N is half the number of phosphates, and 0.114 is an empirically derived coefficient suited for short oligomers. Note that Eq. 2.14 is applicable only for short oligomers, and another equation must be used for longer sequences [132]. These equations make clear that the free energy

32

of DNA hybridization is easily calculable in various salts and temperatures. Because NSs interact primarily through DNA hybridization, the NS system is a unique model that can be used to isolate the effects of inter-molecular interactions on phase behavior.

Chapter 3

Salt-dependent properties of a coacervate-like, self-assembled DNA liquid

3.1 Preamble

This chapter is adapted from "Salt-dependent properties of a coacervate-like, self-assembled DNA liquid," which is the result of a collaboration with Dr. Byoung-jin Jeon, Dr. Dan Nguyen, Nathaniel Conrad, Dr. Deborah K. Fygenson, and Dr. Omar A. Saleh. It is reproduced and adapted from Ref. [41] with permission from the Royal Society of Chemistry.

3.2 Introduction

Since the discovery that phase separation plays a role in sub-cellular organization, many studies have examined the underlying principles of LLPS of biomolecular compo-

nents [17, 120, 145]. Recent works have used intrinsically disordered proteins and RNA as a model system to characterize the effects of net charge, individual sequence changes, and conformational changes on phase behavior [146, 147, 148]. However, there can be unanticipated factors that impact protein-based phase separation. For example, although many works attribute phase separation to attractions between disordered regions of proteins, Wei et al. (2017) concluded that the phase behavior of a protein depends on more than just the disordered regions [9]. They examined the phase separation of a protein, LAF1, and a disordered sequence within LAF1 and showed that the critical salt concentration, viscosity, and mesh size of liquid droplets differed between the two condensates; in other words, the ordered regions of a protein impact phase behavior in addition to the disordered domains [9].

Understanding the formation and properties of biomolecular condensates has proven to be challenging due to the intricacies of the components and of the intermolecular interactions; thus, a unified model that links individual molecular properties to the properties of a coacervate has yet to be developed [1, 149]. Here, the NS system is used to examine how inter- and intra-NS interactions influence bulk phase separation. We expected individual NS properties to be salt-sensitive, due to charge screening effects that modulate the repulsion between negatively charged phosphate groups in sticky-ends of neighboring NSs or in arms within a single NS. Because NS phase separation is dictated by well characterized Watson-Crick-Franklin base pairing, we can relate inter-NS thermodynamics to bulk properties. Bomboi et al. (2015) examined the relaxation of NSs within the dense phase at various salt concentrations [69]. They described the slowing down of NS rearrangement at high salt using sticky end hybridization thermodynamics. Thus, we anticipated that other material properties of NS liquids would be dependent on salt concentration as well.

Here, we find that the changes of some properties can be related to the thermody-

namics of DNA binding, but others cannot. For example, we observe an increase in the viscosity and decrease in diffusivity with increasing salt that can be attributed to the sequence- and salt-dependent thermodynamics of base pairing. From this, we conclude that the transport properties of the liquid are dictated by an Arrhenius-activated process with an activation barrier of a single NS bond. On the other hand, the relationship between volume fraction of DNA in the NS-rich phase and salt establishes that electrostatic screening allows NSs to take on more compact configurations and makes the dense phase more concentrated at higher salt. Similarly, we observe that the surface energy contribution per NS is much lower than the free energy of a single NS–NS bond. We attribute this to NSs being flexible enough to bend such that all arms remain in the dense phase. Finally, the product of the viscosity and diffusion coefficient seems to indicate a breakdown of the Stokes–Einstein relation. From this, we theorize that the interior of the DNA liquid is a heterogeneous, clustered structure and that the size of the clusters depends on salt concentration. Understanding how inter-particle and intra-particle interactions impact the bulk material properties of NS liquids may clarify how individual component properties impact other biomolecular condensates as well.

3.3   Procedures

3.3.1   NS formation

NSs used for this work had the same core sequence as previous NS-liquid works and included two unpaired adenosines at the junction and one unpaired adenosine between the sticky end and double stranded arm (Fig. 3.1a) [34, 47, 50, 69, 150]. Although LLPS here and in previous works was driven by sticky end hybridization of the same sequence (5'-*CGATCG*-3'), in this work, the sticky end was located on the 5' end of each oligomer

whereas it was most often on the 3' end in previous works. We showed that despite this change in design, with sufficient salt and at low temperature, NSs interacted to form DNA-rich, spherical NS-liquid droplets within an aqueous DNA-dilute phase (Fig. 3.1b).
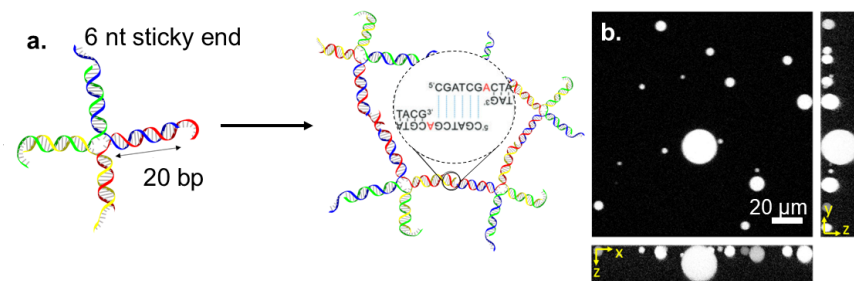
Figure 3.1: (a.) Schematic of individual NS constructs. Once sufficient salt is included, NS liquids are formed via hybridization between 6 nucleotide (nt) sticky ends. (b.) Confocal image of phase separated NS droplets at 0.5 M NaCl. A mixture of untagged and Cy3-tagged NSs (99:1) was used for fluorescent visualization at 561 nm excitation. XZ (bottom) and YZ (right) projections show the spherical shape of the droplets.

3.3.2   Volume fraction in the dense phase

We began by measuring how salt concentration impacts NS concentration in the bulk phase. Previous work has shown that in the phase separating regime, DNA concentration in the dense phase is relatively unaffected by temperature, which suggests that NS concentration may not be impacted by inter-NS binding thermodynamics [34]. To investigate this, we examined how changes in salt concentration affects the density of DNA within the NS liquid via two methods: absorbance spectroscopy and by tracking sedimenting droplets.

Absorbance spectroscopy compares the incident light intensity to the intensity of light that reaches a detector after passing through a sample. The amount of light absorbed depends on the wavelength of light and the composition of the sample. (For example, peak absorbance for DNA is at 260 nm [151].) The concentration of DNA can be determined

using the absorbance at 260 nm and calculated using Beer's Law:

$$A_{260} = \varepsilon l C \tag{3.1}$$

where l is the path length (set by the device), C is the molar concentration of NSs, and ε is the molar extinction coefficient, which is dependent on the DNA sequence. (See Methods for ε calculation.) Following previous work, we separated the dense and the dilute phase using centrifugation and extracted each for analysis with absorbance spectroscopy (Fig. 3.2a) [34].

Using this method, we showed that NSs exhibited a key property of LLPS: At constant interaction strength, the concentration of macromolecules within the dense phase should be constant with changing bulk concentration. Instead, as the bulk concentration of the macromolecule is increased, the volume taken up by the dense phase should increase, but the interior properties of the dense phase should remain the same. We show that this holds true: the concentration in the dense phase is constant for different bulk concentrations of NSs (Fig. 3.2b).

We confirmed that centrifuging the NS liquid does not impact the phase behavior by comparing the concentration measured via absorbance spectroscopy with the concentration derived from NS droplet sedimentation. NS droplets sink because they are dense compared to the surrounding solution (Fig. 3.3a). The rate of descent is dictated by the properties of the dilute phase and the DNA-rich phase: gravitational force pushes the droplet downward but is resisted by the Stokes' drag force — a frictional force created by the viscous solution surrounding the drop. Drops reach terminal (constant) velocity
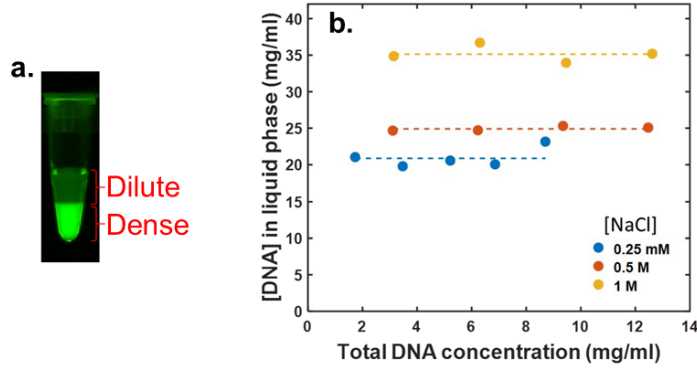
Figure 3.2: (a.) Bulk phase separation of 100 μL of NS solution. NSs are visualized by adding YOYO-1 at 1:100 dye to NS molar ratio. (b.) The concentration of DNA in the NS liquid phase is independent of the total DNA concentration of the NS solutions at all three salt conditions explored.

when the net force on it is zero (Fig. 3.3b). From the velocity of sedimentation, v, we solved for the difference in mass density between the dense and dilute phase:

$$\Delta\rho = \frac{9}{2}\frac{v\eta_{fluid}}{gR^2} \tag{3.2}$$

where η_{fluid} is the viscosity of the surrounding fluid, and R is the radius of the droplet. Assuming Stokes' drag force is applicable requires that the solution is not turbulent, but rather is in the creeping-flow regime, while the droplet sediments [152]. The turbulence of a fluid is characterized by the Reynolds number, the ratio between viscous forces and inertial forces:

$$Re = \frac{\rho_{fluid}v\ L}{\eta_{fluid}} \tag{3.3}$$

where ρ_{fluid} is the mass density of the dilute phase (which was approximated as a solution

39
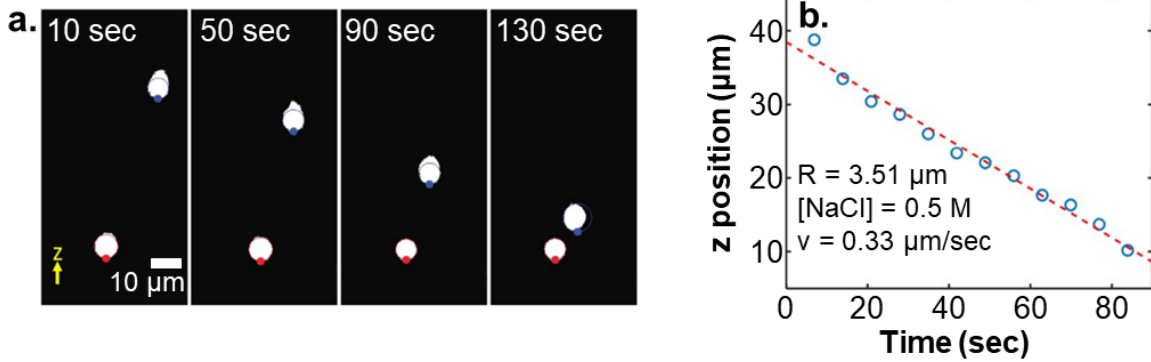
Figure 3.3: (a.) Projection of NS drop sedimenting (blue) with a drop settled on the bottom glass surface (red) for reference. (b.) The velocity of a droplet sedimenting is constant when at terminal velocity.

of salt and water), v is the velocity of the droplet sedimenting, and L is the characteristic length scale of the system (taken to be the radius of the drop). Approximating each parameter to be their maximum possible value ($\rho_{fluid} = 1040$ mg/mL, the mass density of 1 M NaCl in water; $v \approx 10$ μm/s; the maximum radius of a drop to be 50 μm; and $\eta = 10^{-3}$ Pa·s) gives a maximum Reynolds number as $Re < 5 \times 10^{-4}$ — far below the cut off for turbulent flow, which is taken to be of order one, so our assumption of employing Stokes' drag force is validated [152].

Only four components were present while tracking the droplet sedimentation: NSs, salt, buffer, and water. Assuming that the buffer and salt concentrations in the dense and dilute phase are equal, the total density of the droplet, ρ_{drop}, is equal to a weighted average of the density of DNA and the density of salt water (referred to as solution here):

$$\rho_{drop} = \phi_{DNA} \times \rho_{DNA} + \phi_{solution} \times \rho_{solution}, \tag{3.4}$$

where ϕ indicates the volume fraction of each component within the dense phase. $\rho_{solution}$ was adjusted based on the salt concentration [153], and ρ_{DNA} was taken to be 1700 mg/mL, the density of pure DNA [104]. Because the sum of the volume fractions of each species must equal one, from Eq. 3.4, the volume fraction of DNA in the dense phase was calculated using

$$\phi_{DNA} = \frac{\rho_{drop} - \rho_{solution}}{\rho_{DNA} - \rho_{solution}} \tag{3.5}$$

3.3.3   Viscosity

Viscosity, or a fluids ability to resist flow, is a key property of liquids. Because fluid flow is dependent on bonds breaking, we anticipated that the viscosity within the NS dense phase would depend on salt concentration where more stable bonds (high salt) would result in a higher viscosity. We measured the viscosity in the DNA-dense phase using microrheology and bulk oscillatory rheology.

Microrheology is performed by tracking the mean squared displacement ($MSD = \langle (r(t) - r(0))^2 \rangle$) of fluorescent probe particles as they move due to Brownian motion while the movement is resisted by the surrounding fluid. The scaling of the MSD with lag time can be used to determine properties of the sample. For example, the MSD of a probe in purely elastic materials is independent of the lag time whereas the MSD in purely viscous materials is linearly proportional to time. Here we used 200 nm diameter beads, much larger than an individual NS, and embedded them into large NS droplets (Fig. 3.4a). We observed that over long time scales, the MSD of the bead is linearly proportional to the lag time of the measurement, τ; thus the NS liquid acts as a viscous liquid on long time scales (Fig. 3.4b), and the MSD is given by

$$\langle MSD \rangle = 2dD_{bead}\tau \qquad (3.6)$$

where d is the number of dimensions in which the bead displacement is being tracked (in this case, 2) and D_{bead} is the diffusion coefficient of the bead [78]. We derived the viscosity of the dense phase, η, based on the diffusion of a bead of radius R using the Stokes-Einstein equation,

$$D = \frac{k_B T}{6\pi\eta R} \qquad (3.7)$$

For bulk rheology, the dense NS phase was placed between two horizontal plates. The bottom plate oscillated at a set frequency, and the top plate detected the NS-liquid's resistance to the oscillations. The viscosity can be calculated based on the value of the modulus at the frequency where the material shifted from exhibiting elastic behavior to exhibiting viscous behavior: $\eta = 2\pi G_c/\omega_c$ (Fig. 3.4c). For a more in-depth description of bulk rheology, see Ref. [57].

The viscous response measured via the two methods agree incredibly well (e.g., η was measured to be 45 Pa·s via bulk rheology and 46 ± 3 Pa·s via microrheology at 500 mM NaCl). In addition, for both experiments, a deviation from viscous behavior is seen at short time scales (high frequency for bulk viscosity). This may be indicative of the NS liquid's viscoelastic properties. However, in this work, we focused on long time scales where the dense phase acted as a viscous liquid.
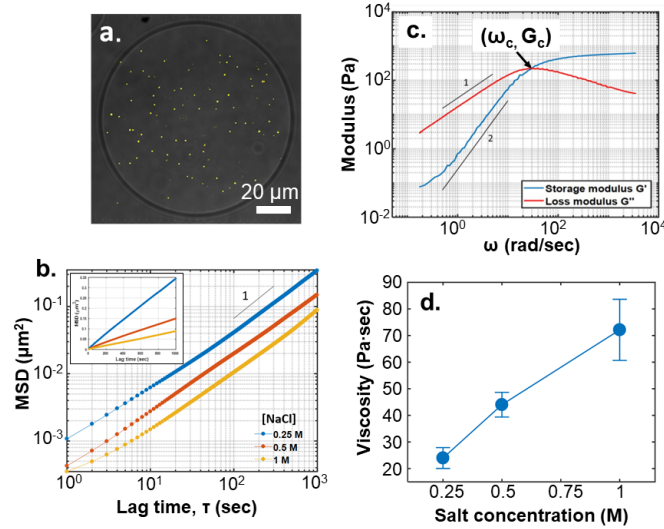
Figure 3.4: **Measurements of viscosity** (a.) Confocal image of fluorescent probe particles (yellow) embedded in a large NS droplet. (b.) Log–log plots of averaged mean squared displacement (MSD) of the probe particles at three different concentrations of NaCl. (c.) Storage and loss moduli (G' and G") of the NS liquid phase at 0.5 M NaCl at 20 ° C from bulk rheology. (d.) Viscosity increases with increasing salt concentration, as measured with microrheology.

3.3.4   Surface tension

Interfaces are energetically costly — for example, in the NS system, we expected that arms at the surface of a drop would be unable to form bonds due to being in contact with the dilute solution. Because of this, NS drops and other liquids round up into spheres, the shape which minimizes the surface area to volume ratio and thus the free energy contribution of the surface. The surface tension describes the free energy contribution per unit area due to an interface [79]. Thus, we expected the surface tension of the NS droplets to increase because the enthalpic penalty per unbound arm would increase at the surface.

Here, we measured the surface tension, σ, by tracking the relaxation of a drop into a sphere of radius R (Fig. 3.5a). We found non-spherical drops by monitoring coalescence events: As two drops begin to coalesce, they form a bridge that connects the two drops
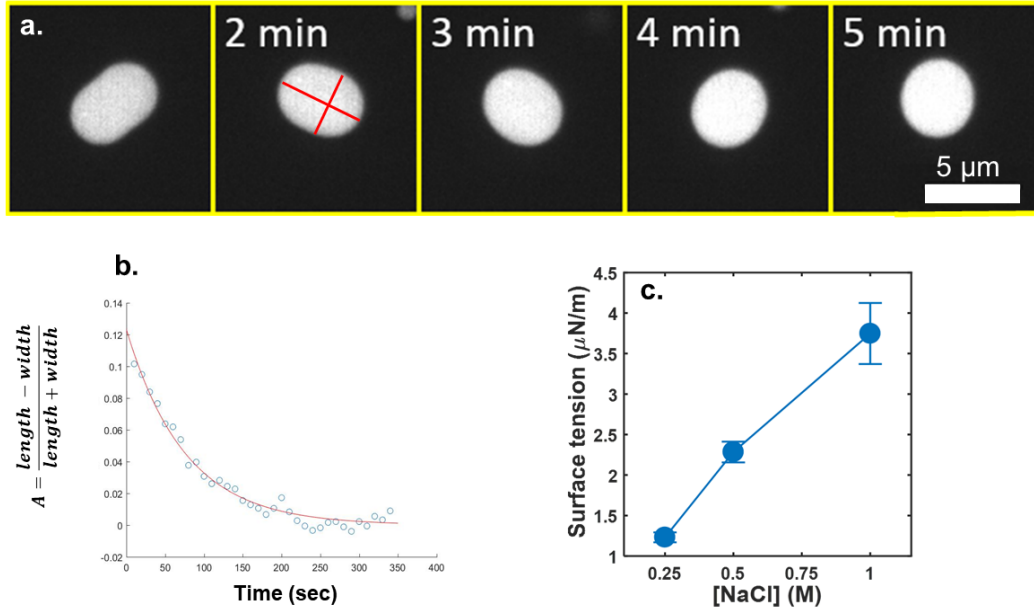
Figure 3.5: (a.) Coalescence event of two NS-liquid droplets imaged over time. (b.) Aspect ratio of a NS-drop is defined as $A = \frac{L-W}{L+W}$ where L and W are the length and width of the deformed droplet under relaxation. (c.) Surface tension increases with increasing salt.

with a width smaller than the radii of either drop. As time progresses, the width of the bridge increases and the coalescing structure forms an ellipsoid. We measured the aspect ratio of the ellipsoid, $A = \frac{L-W}{L+W}$ where L is the length of the longest dimension and W is the maximum width perpendicular to L, and tracked the rate at which the drop rounded into a sphere (Fig. 3.5b). The timescale of relaxation, τ_{relax} is given by [154]:

$$\tau_{relax} = \frac{(2\lambda + 3)(19\lambda + 16)}{40(\lambda + 1)} \frac{\eta_{solution} R}{\sigma} \tag{3.8}$$

where λ is the ratio between the viscosity within the drop (found above) and the surrounding solution, $\lambda = \frac{\eta_{drop}}{\eta_{solution}}$. In the limit where the internal viscosity is much larger

44

than the external viscosity, Eq. 3.8 reduces to

$$\tau_{relax} \approx \frac{19}{20} \frac{\eta_{drop} R}{\sigma}. \tag{3.9}$$

Similar methodology has been used to determine the ratio of viscosity and surface tension of each of the nucleolar subcompartments found in *X. laevis* oocytes [17] and in model systems composed of single proteins and RNA [155]. Here, we isolated the surface tension by incorporating the viscosity that was determined above (Fig. 3.5c and Table 3.4.3).

3.3.5   Diffusivity

The diffusion of particles within liquids depends on pairwise interactions where stronger interactions tend to result in slower rearrangement. Previous work concluded that NS network rearrangement is dependent on the breaking of one or a few NS bonds [34, 50]. Thus, we anticipated the diffusivity of NSs within the dense phase to decrease with increased salt. To measure the diffusion of NSs within the dense phase, we performed FRAP — fluorescence recovery after photobleaching. FRAP involves exposing a small spot of sample to a high-power light source to photobleach the fluorophores within that region (Fig 3.6a) [117]. Immediately after photobleaching, the intensity within the dimmed spot can be well fit to a Gaussian (Fig. 3.6b). As time passes, particles that have not been photobleached diffuse into the dim region and photobleached particles diffuse out. This causes the intensity within the dim spot and the variance of the Gaussian, $s^2(t)$, to increase. The rate of recovery within the photobleached region can be related to the diffusion coefficient of the particles by:

$$D \propto \frac{s^2(t)}{t} \tag{3.10}$$

Additionally, FRAP can be used to determine if the sample is gel-like or liquid-like. If after a long time the intensity returns to the original intensity (full recovery), the sample is liquid-like. If it recovers only partially, the sample is gel-like.
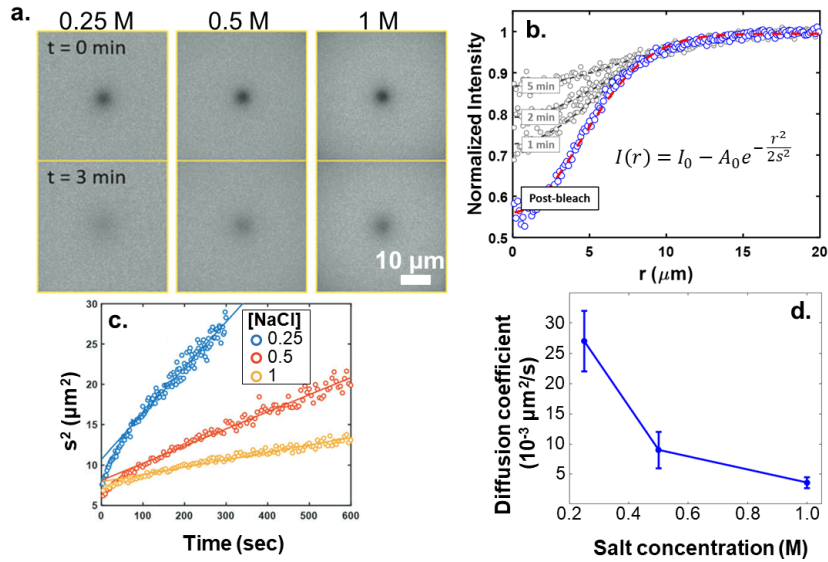
Figure 3.6: (a.) Photobleached spot produced by FRAP immediately after photo-bleaching (top row) and recovery after 3 minutes (bottom row). The salt concentration in the left column is 0.25 M NaCl, the middle is 0.5 M NaCl, and the right is 1 M NaCl. (b.) Average pixel intensity with the center of the drop set to $r = 0$. (c.) As the photobleached spot recovers, the variance of the Gaussian fit to the intensity profile, s^2, increases. The rate of recovery depends on salt concentration. (d.) Diffusion coefficient as it varies with salt.

3.4   Results and Discussion

We compared NS liquid bulk properties to salt concentration because previous work related NS rearrangement to the thermodynamics of sticky end hybridization, which is

known to depend on salt concentration [69]. From SantaLucia and Hicks (2004), we calculated the free energy of binding of 5'-*CGATCGA*-3' sticky ends at each salt concentration which are given in Table 3.1 [132]. (See Chapter 2 for a review of the SantaLucia model.)

[NaCl] (M)	ΔG_{NS} (kcal/mol)	ΔG_{NS} ($\times 10^{-20}$ J/interaction)
0.25	-8.75	-6.1
0.5	-9.13	-6.3
1	-9.5	-6.6

Table 3.1: ΔG of NS–NS binding at various salt concentrations

Recent work has used small angle x-ray scattering (SAXS) to derive the interaction potential between NSs in the dense phase [143]. Using NSs with the same *CGATCGA* sticky end, Spinozzi et al. (2020) calculated the inter-NS binding enthalpy to be approximately the same as the enthalpy that corresponds to the free energies given in Table 3.1.

Figure 3.7: The relationships of (a) viscosity, (b) diffusivity, and (c) surface tension with [NaCl] indicate each parameter is sensitive to the energetics of DNA hybridization.
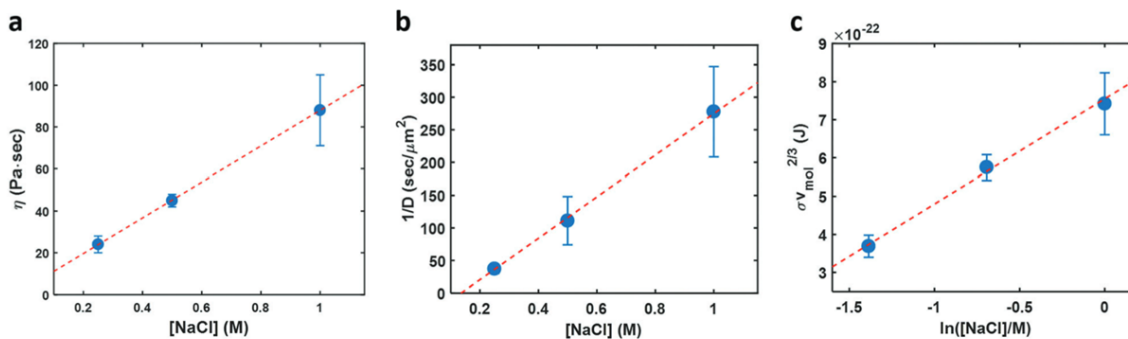
3.4.1   NS binding thermodynamics, viscosity, and diffusivity

Viscosity and diffusivity depend on the breaking and formation of bonds between neighboring particles. Previous work has shown that NS network rearrangement slows

[NaCl] (M)	Viscosity from microrheology (Pa·s)	Viscosity from bulk rheology (Pa·s)	Diffusion coefficient ($10^{-3}\mu\mathrm{m}^2/\mathrm{s}$)
0.25	24 ± 4	x	27 ± 5
0.5	45 ± 3	46	9 ± 3
1	88 ± 17	x	3.6 ± 0.9

Table 3.2: Transport properties vs salt concentration

down at higher salt due to more stable inter-NS interactions [69]. We hypothesized that viscosity and diffusivity would reflect this as well and indeed found that stronger NS–NS interactions result in an increase in viscosity and a decrease in diffusivity (Table 3.4.1).

Previous work determined that for processes that involve breaking NS bonds, the dynamics are well described by Arrhenius behavior [34, 50, 69]. The Arrhenius equation describes the dependence of the timescale of a reaction, τ, on activation energy and temperature:

$$\tau \propto e^{E_a/k_B T} \propto e^{\ln[Na^+]} \tag{3.11}$$

where E_a is the activation energy of a reaction set to ΔG_{NS} here [91]. Thus, we expected these properties to scale with salt as $\eta \propto [NaCl]$ and $1/D \propto [NaCl]$, which is supported by the data (Fig. 3.7a, b). We provided further evidence for this model by performing microrheology with NS drops of a stronger sticky end sequence, 5'-$ACGCGT$-3'. At 500 mM NaCl, $\Delta G_{ACGCGT} \approx -9.5$ kcal/mol while $\Delta G_{CGATCG} \approx -9.1$ kcal/mol. (Note that at 1 M NaCl, $\Delta G_{CGATCG} \approx -9.5$ kcal/mol.) The viscosity of liquids composed of stronger sticky end NSs at 500 mM is approximately the same as the viscosity of original sequence NS-liquids at 1 M NaCl; i.e., the viscosities are the same when the free energy of binding for the two NSs are the same (Fig. 3.8.)
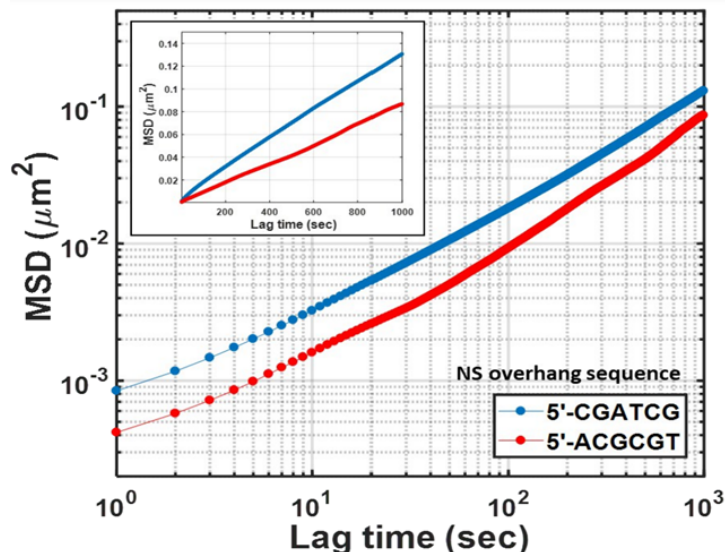
Figure 3.8: Averaged mean squared displacements (MSD) of 200 nm probe particles in liquid droplets of two different NSs, NS-CGATCG and NS-ACGCGT, as a function of lag time at 0.5 M NaCl. The lower MSD values for NS-ACGCGT lead to a higher viscosity, when calculated from $MSD = 4D_{probe}\tau^{\alpha}$.

We also find that these properties scaled such that the activation barrier of the Arrhenius behavior is equal to about one broken NS bond. This agrees with previous DLS work (and more recent rheology work) that similarly determined that NS network rearrangement is dependent on one or two NS bonds breaking [50, 57, 69]. Other works have used microrheology to measure the viscosity of the NS dense phase formed by NSs similar to those used here. Fernandez-Castanon et al. (2018) observed a decrease in viscosity with increasing temperature which follows the Arrhenius model that we propose for relating the macroscopic transport properties to individual NS rearrangement; however, their measured viscosity is about an order of magnitude higher than the measurements here, despite being at a lower salt [71]. Similarly, Biffi et al. (2015) used impurities in their system to measure a similar viscosity to the viscosity found here despite being at a much lower salt than those used here [50]. Finally, Bomboi et al. (2019) created a system in which NSs could only interact with each other via a linker. In addition to

effectively extending each NS arm, they were able to enforce that the NS liquid was not in a fully bound state. They measured the viscosity to be orders of magnitude below our measured viscosity indicating that arm length and/or forming a fully bonded network creates a large impact on the viscosity of the dense phase [52].

Additionally, Lee et al. (2021) used FRAP and observed that the trend of NS diffusivity with salt matches the trend that we observed here [43]. They also observed a larger increase in the diffusion coefficient upon increasing intra-NS flexibility (as compared to changing salt concentration). Although they measured a larger diffusion coefficient than this work, several key differences exist between these systems — namely NS valency, arm length, and temperature.

3.4.2 Beyond binding: NS concentration in the dense phase

The concentration of NSs within the dense phase found via absorbance spectroscopy and droplet sedimentation are listed in Fig. 3.9b. The two methods show that the concentration within the dense phase increases with increasing salt concentration (Fig. 3.9a).

We expected the concentration of NSs in the dense phase to increase with increasing salt concentration due to the NS–NS bonds being stabilized. However, Biffi et al. (2013) calculated the concentration of a fully bonded network assuming that the center of each NS is a point on a diamond lattice and all arms are rigid [34]. The concentration of DNA in this approximation was calculated to be 13.3 mg/mL, significantly less than the concentrations measured here. We speculate that the measured NS concentration is above the limit of the diamond lattice because the angle between NS arms is not fixed, and NSs can take on more compact configurations than the model allows. As the salt concentration is increased, the negative backbones within a NS are increasingly screened
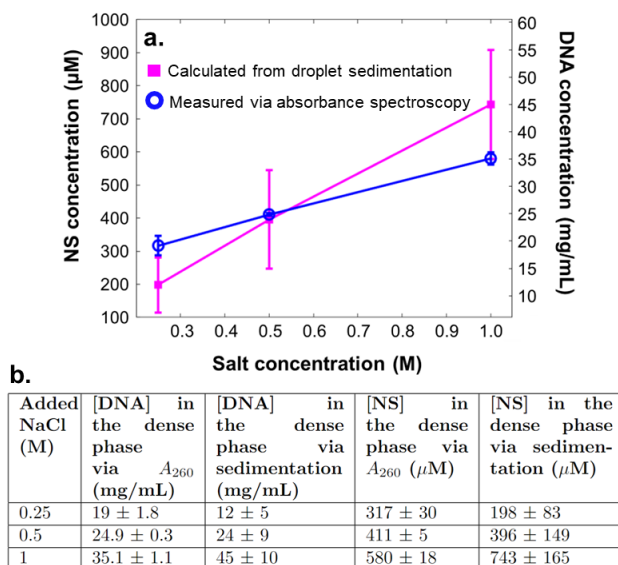
Figure 3.9: NS concentration in the dense phase increases with increasing salt concentration shown (a.) as a graph and (b.) in a table.

which allows NSs to adopt more compact shapes at higher salt concentrations. Finally, from these results, we calculated the volume fraction of NSs within the dense phase to be $1 - 2\%$. A low volume fraction is to be expected given the stiff nature of each arm and limited valence of the NSs; although individual NSs can become more compact at higher salt concentrations, the stiff arms continue to push neighboring NSs away from each other.

Previous work used absorbance spectroscopy and found the concentration of DNA in the dense phase to be about 17 mg/mL at 50 mM NaCl and 20 °C [34]. This aligns well with the absorbance spectroscopy measurements here, which estimate the concentration to be about 15 mg/mL at 50 mM NaCl. Recent work has suggested that DNA concentration in the dense phase is regulated by individual NS properties such as arm length and space taken up by individual NSs [156]. Other experimental results have supported this; for example, Tayar et al. (2022) published work that measured the concentration of NSs in the dense phase composed of NSs with different sticky ends, but the same arm

size. They found a similar DNA density despite working in different solution conditions [157]. Lee et al. (2021) and Conrad et al. (2022) observed a salt-dependent trend that replicated what was observed here: that NSs are more concentrated in the dense phase at higher salt [42, 43]. Lee et al. (2021) used three-armed NSs and consistently measured a lower concentration of NSs in the dense phase than the concentrations measured here, similar to the valence-dependent trend of DNA concentration in the dense phase that was measured by Conrad et al. (2022).

3.4.3 Beyond binding: Surface tension

To compare the surface tension to the free energy of a NS–NS bond, we calculated the free energy penalty per NS at the interface. We anticipated that the surface tension should scale as $\sigma \propto \frac{|\Delta G_{NS}|}{v_{NS}^{2/3}}$, where v_{NS} is the volume per NS (making $v_{NS}^{2/3}$ the surface area taken up by each NS) calculated via our concentration measurements. Because the concentration in the dense phase changes with salt concentration, we expect the number of NSs at the surface to change as well (Table 3.4.3). We used the SantaLucia model to determine that surface tension should scale with $\ln([NaCl])$ [132]. To compare the surface tension to ΔG_{NS}, we calculated the free energy of a single interaction.

[NaCl] (M)	σ (μN/M)	Volume per NS (nm^3)	$\sigma v_{NS}^{2/3}$ ($\times$ 10^{-22} J)	$|\Delta G_{NS}|$ ($\times 10^{-20}$ J)
0.25	1.23 ± 0.06	5190	3.7	6.1
0.5	2.28 ± 0.13	4000	5.8	6.3
1	3.7 ± 0.9	2840	7.4	6.6

Table 3.3: Surface tension and related values as compared to ΔG_{NS} of individual interactions

We find that $\sigma v_{NS}^{2/3}$ scales linearly with $\ln[NaCl]$ indicating that surface tension depends on both thermodynamic interactions and conformational changes of NSs (Fig. 3.7c). Interestingly, we calculate the surface penalty per NS to be consistently orders of

magnitude less than the binding free energy of a single NS–NS interaction. We attribute this to the internal flexibility of each NS: most NS arms are bent inward and are able to join the NS network, and only about one or two in 100 sticky ends are unpaired at the surface.

Recently, Agarwal et al. (2022) compared the surface tension of NS drops of varying arm length. They determined that for their work, scaling the surface tension by the surface area of a NS is insufficient to accurately describe the dependence of NS droplet coarsening on NS size [39]. Instead, they found a smaller decrease in surface tension with increasing arm length than is predicted by the ideal (NS size)^2. That said, we showed that this was sufficient to explain how surface tension scales with salt concentration indicating an interesting distinction between the effects of NS compaction and NS arm length on surface tension.

3.4.4   Beyond binding: Stokes-Einstein Equation

The Stokes-Einstein equation (Eq. 3.7) predicts that for constant particle size, the product of the diffusion coefficient and the viscosity of the fluid should remain constant at the same temperature. However, we observe that the product $D\eta$ decreases with increasing salt concentration (Fig. 3.10). One might assume that the change in $D\eta$ could be explained by the changing concentration of NSs within the dense phase; however, this would result in an increase in $D\eta$ with increasing salt concentration rather than the measured decrease. Instead, we postulate that NSs within the dense phase are inhomogeneous: rather than being evenly distributed in the dense phase, they form heavily-linked clusters that are spatially distinct from each other. As the salt concentration increases, the clusters grow in size and have longer lifetimes which would result in the decrease in $D\eta$ as observed. This may seem to contradict the conclusion above — that the transport
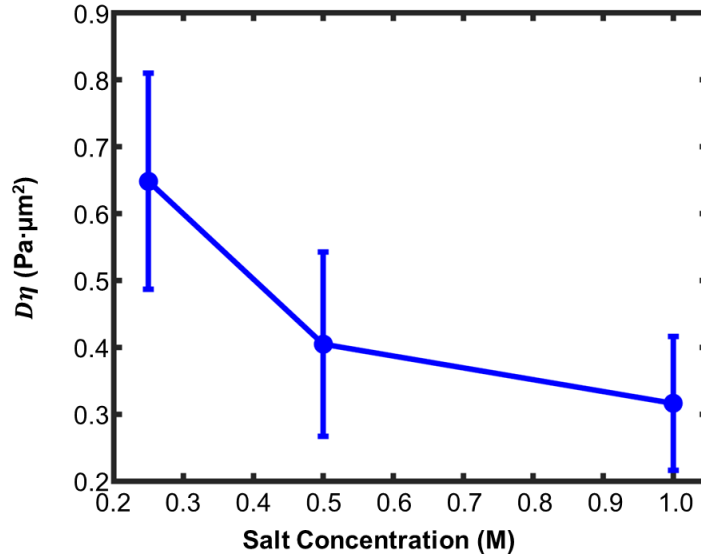
Figure 3.10: The product of the NS diffusion coefficient in the dense phase and viscosity of the dense phase decreases with increasing salt concentration.

properties depend on breaking one NS–NS bond; however, we posit that the clusters are connected by relatively few bonds, which would dominate the transport properties. This conclusion has since been supported by Conrad et al. (2019), which similarly suggested that the interior of the NS liquid was composed of loosely-linked clusters based on the stress where the NS-rich phase yields in bulk rheology [57].

3.4.5 Comparison to other coacervate systems

The unique features of NS-liquids become clear when compared to those of other reported biomolecular liquids, such as synthetic coacervates and liquids derived from components of intracellular droplets (see Table 3.4). The most salient difference is that NS-liquid properties respond to salt in the opposite manner as the other systems. This occurs because the NS-liquids form due to salt-stabilized DNA hybridization, while the other systems form due to electrostatic attractions, which are weakened by added salt. Table 3.4 also points out that the various biomolecular liquids vary strongly regarding

System	Macromolecular volume fraction	Viscosity (Pa·s)	Surface tension (N/m)	Ref.
DNA NS droplets	$2 - 3.5$ wt% (increase)	10^1 (increase)	10^{-6} (increase)	This study
Synthetic coacervates	$15 - 25$ wt% (decrease)	$10^1 - 10^5$ (decrease)	$10^{-5} - 10^{-4}$ (decrease)	[119, 158, 159, 160, 161, 162, 163]
Intracellular droplets	$0.3 - 0.5$ wt% (decrease)	$10^0 - 10^1$ (decrease)	$10^{-6} - 10^{-4}$ (decrease)	[17, 18, 164, 165]

Table 3.4: Physical properties of various coacervate and biomolecular liquid systems (response to increasing [salt]).

their density; note that the variation in the remaining properties (viscosity and surface tension) can roughly be understood as being sensitive to density. Synthetic coacervate systems are generally at least 10-fold denser than the other systems, likely because the constituent polymers tend to be highly charged and flexible, permitting each chain to contact many oppositely-charged chains, thus driving higher liquid densities [119]. In contrast, the present NS-liquid system has a limited valence: strong inter-particle contact is permitted only at the four overhangs, which decreases particle packing and liquid density. Further, we expect that the stiff nature of the DNA arms contributes to the low density by pushing bound particles away from each other. Interestingly, single-component liquids formed from purified LAF1, a protein derived from an intracellular droplet system, achieve an extraordinarily low density (0.3%). The researchers attributed the expansive occupied volume in their system to large configurational fluctuations of the protein [9]. Thus, both the NS model system and the LAF1 model system have very low volume fractions in the dense phase which is modulated by configurational changes.

3.5   Conclusion

The goal of this work is to understand how inter-molecular properties affect NS material properties. Previous works have concluded that the timescale of NS rearrangement within the dense phase is dominated by NS–NS binding interactions [47, 69]. This work shows that while some bulk material properties can be directly linked to thermodynamics of NS binding, other properties require further analysis. We propose that these properties are instead linked to the flexibility of individual NSs and clustering within the dense phase. Specifically, both the viscosity and diffusivity of NSs in the DNA-dense phase can be well described by Arrhenius behavior with the free energy of NS binding as the activation energy, which is supported by previous research [34, 50, 69]. Beyond this, the surface energy contribution per NS is much less than the free energy of a single NS–NS bond. We postulate that most arms are turned inward at the surface, so there are not many unbound sticky ends. Similarly, we attribute the increase in concentration of NSs in the dense phase to increased screening between arms of a single NS, allowing them to adopt a more condensed shape. Finally, our results seem to contradict the Stokes-Einstein equation in that the product of the diffusion coefficient and the viscosity of the NS-liquid decreases with increasing salt concentration. We postulate that this is due to an inhomogeneous distribution of NSs in the dense phase — that there are clusters of tightly linked NSs that grow in size and stability with increasing salt. These results show that the NS-rich phase properties have contrary reactions to salt concentration from other biomolecular condensates, which we speculate is due to the different attractions that drive phase separation in the two systems. More recent works have focused on NS material properties as they relate to NS binding strength and other factors [43, 52, 57, 143, 156, 157]. These works highlight that, in addition to salt concentration, individual NS properties such as internal flexibility and valency play key roles in

determining NS liquid properties.

Chapter 4

Length-Dependence and Spatial Structure of DNA Partitioning into a DNA Liquid

4.1   Preamble

This chapter is based off of the published work "Length-Dependence and Spatial Structure of DNA Partitioning into a DNA Liquid," which is the result of a collaboration with Dr. Dan Nguyen, Dr. Byoung-jin Jeon, and Dr. Omar A. Saleh. It is reproduced and adapted from Ref. [75]. Copyright 2018 American Chemical Society.

4.2   Introduction

Within the cell, biomolecular condensates can be composed of tens or hundreds of distinct components [166, 167]. Some of these components are scaffold molecules, which are essential for coacervates to form. The membrane-less nature of the droplets permits

facile exchange of other molecules with the external solution. These solute molecules, known as client molecules, are not necessary for the phase separation process, but they have been found within biomolecular condensates at concentrations much higher than in the surrounding solution [167].

Recent work has tried to understand what physical factors determine client sequestration. Clients have been shown to bind to scaffolds via a wide variety of interactions including sequence-specific binding between nucleic acids and proteins and non-specific interactions such as electrostatic attraction [166]. The valency of both the client and the scaffold molecules have been shown to have a significant impact on partitioning and can be modulated via, e.g., post-translational modifications [166, 167]. In addition, recent work has shown that — despite not being necessary for phase separation to occur — client molecules can modulate the physical properties of the dense phase and impact phase behavior; they can destabilize or promote phase separation depending on if they are competing for the same interaction sites as other scaffold molecules or are binding to other sites on the scaffold molecules, respectively [15, 16].

We aimed to understand the physical parameters that impact the composition of solutes within phase separated liquids. The NS system is an ideal candidate for studying solute partitioning due to its programmable nature and well-characterized inter-particle interactions. Here, we examined the partitioning of two solutes into the NS liquid system and isolated the effects of two factors that influence client partitioning into biomolecular condensates. We began by examining the partitioning of a neutral, branched polymer and observed that larger solutes are more excluded from the dense phase than smaller solutes. We then moved on to the partitioning of different lengths of linear dsDNA. We took advantage of the programmable nature of DNA and added NS interaction sites to the ends of the linear dsDNA. Previous work had shown that incorporating sticky ends onto solute molecules can drive partitioning into DNA dense phases, but most works

had focused on the partitioning of short DNA sequences (with similar sizes to NSs) [52, 53]. From examining the partitioning of longer strands of DNA, we show that solute partitioning is a balance between length-dependent confinement and attractions between the client and scaffold molecules.

4.3   Results

4.3.1   Effective mesh size of NS-liquids

We first probed the ability of a neutral, branched macromolecule, FITC-labeled dextran, of varying molecular weight (MW) to permeate the NS liquid. We formed NS droplets without the solute present using NS with the same sequence as the previous chapter. We then added a few μM of dextran and incubated the sample for several hours to allow for equilibration. We used a confocal microscope and constructed normalized radial intensity distributions, $I(r)$, which show that dextran partitioning was homogeneous within the droplet interior, indicating that the system had reached equilibrium (Fig. 4.1b). In addition, we confirmed that this concentration of dextran is in a dilute solution regime (where we can ignore solute-solute interactions) by showing that the partitioning behavior is insensitive to dextran concentration (Fig. 4.1c).

We then calculated the relative intensity within the dense and dilute phases and calculated a partition coefficient, $P = \frac{I_{dense}}{I_{dilute}} \propto \frac{C_{dense}}{C_{dilute}}$, assuming that the measured intensity is linear with concentration [43]. For all MW measured, dextran is hindered from entering droplets ($P < 1$); however, larger dextran polymers are more excluded from the dense phase than smaller polymers (Fig. 4.1a, d). The size-dependent partitioning of dextran indicates that NS-liquid permeability is controlled by a characteristic mesh size, ξ. To estimate this length scale, we assumed that each FITC-dextran sample is polydisperse
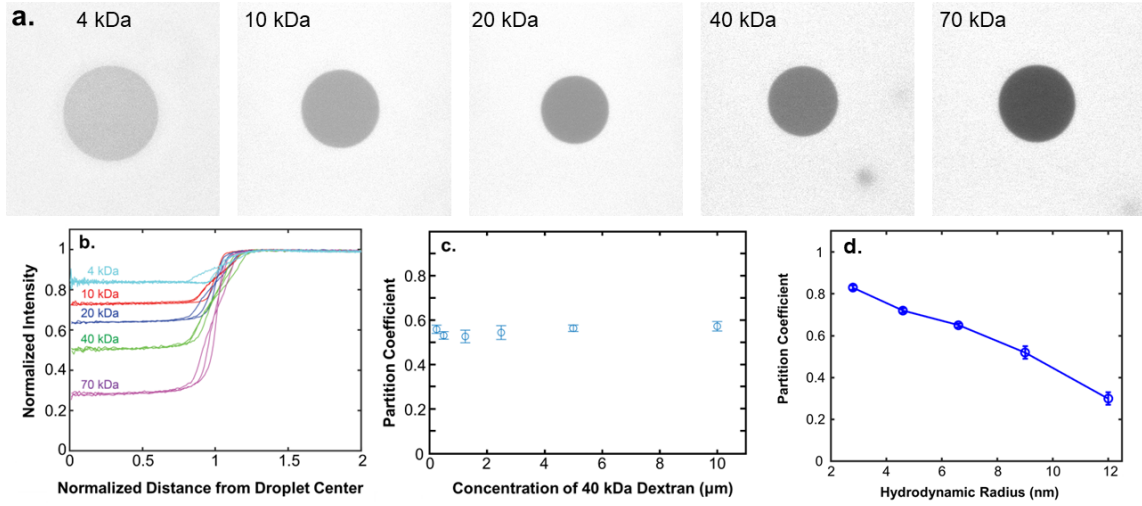
Figure 4.1: **Dextran partitioning into NS droplets** (a.) Example confocal images of various sizes of FITC-dextran combined with NS drops. (b.) Fluorescent intensity profiles (from the center of a NS-liquid droplet into bulk solution) of FITC-dextran partitioning into NS droplets. Each curve corresponds to a distinct droplet, where fluorescence is normalized to the signal from bulk solution and radius is normalized to the droplet radius. (c.) The partition coefficient of FITC-dextran (40 kDa) into NS-liquids is independent of solute concentration up to 10 μM, indicating the measured partition coefficients are in the dilute-solute regime. (d.) The partition coefficient of dextran decreases with increasing hydrodynamic radius.

and that the polydispersity is normally distributed around the reported size. In addition, we assumed that molecules with hydrodynamic diameters that are bigger than the mesh size, $D_h > \xi$, are excluded from the NS-liquid, while those smaller than the mesh size, $D_h < \xi$, can freely enter. Thus, when the average size of the dextran molecules is the same size as the mesh size, $\langle D_h \rangle = \xi$, half of the molecules will be fully excluded from the dense phase (because their hydrodynamic radius is greater than the mesh size). The smaller half of the molecules will partition into the dense phase such that the concentration in the dense and dilute phase will be equal. Taking f to be the fraction of small molecules that partition into the droplet and $1 - f$ to be the fraction of small molecules that do not enter the droplet, the number of dextran molecules within the dense and dilute phases are

$$N_{dense} = f N_{small} = \frac{N}{2} f$$
$$N_{dilute} = (1 - f)N_{small} + N_{big} = \frac{N}{2}(1 - f) + \frac{N}{2} \tag{4.1}$$

where N is the total number of dextran molecules, and N is divided by two in the third expression in each equation because $N_{small} = N_{big} = \frac{1}{2}N$. f is expected to be equal to the ratio of the volume of the dense phase and total volume, i.e., $f = \frac{v_{dense}}{v_{tot}}$, because it only considers dextran molecules which easily partition into the dense phase. This gives

$$P = \frac{C_{dense}}{C_{dilute}} = \frac{fN}{2v_{dense}} \frac{2v_{dilute}}{(2 - f)N} \tag{4.2}$$

Because we used a low concentration of NSs, we approximated the volume of the dilute phase to be equal to the total volume, thus, $f \approx \frac{v_{dense}}{v_{dilute}}$. This gives that the partition coefficient is

$$P \approx \frac{1}{2 - f} \tag{4.3}$$

Again, employing that the volume of the dense phase is small, f is expected to be small as well, thus, $f \ll 2$. This approximation gives a partition coefficient of $P \approx 1/2$ when the average hydrodynamic radius of the dextran is the same as the mesh size. Because this roughly occurred for the 40 kDa dextran sample, we estimated $\xi \approx 9$ nm (Fig. 4.1b).

4.3.2   Linear dsDNA partitioning is sequence-specific and length-dependent

We next examined the ability for linear dsDNA *linkers* of various lengths and NS binding affinities to partition into NS liquids (Fig. 4.2A). For this, we followed the same preparation protocol as for dextran: we formed NS droplets, added the linker such that

the concentration of linker remained in the dilute regime, and allowed the sample to equilibrate over a long time. Similar to dextran, dsDNA with no NS interactions (blunt dsDNA) remains largely excluded from the NS-liquid phase (Fig. 4.2B); however, unlike dextran, blunt dsDNA partitioning shows no clear size-dependent trend (Fig. 4.3A).

We tuned linker–NS interactions by incorporating overhangs on one or both ends of the dsDNA (Fig. 4.2A). These single stranded sequences included both the sticky end and an abasic spacer between the sticky end and double stranded part of the linker (which was necessary for incorporating sticky ends on the linker, see Methods), making the NS–linker interaction and the NS–NS interaction about the same strength. For the shortest linker, 131 bp, adding a single overhang to one side of the dsDNA drives preferential partitioning ($P > 1$) such that the concentration of linker within the drop is higher than the surrounding solution. Adding a second overhang to the shortest linker results in stronger partitioning: the partition coefficient of the 131 bp linker with two overhangs is roughly five times that of its single overhang counterpart (Fig. 4.3D). Interestingly, another work measured a similar increase in partitioning when transitioning from monovalent clients to divalent clients in a model protein-based system [167].

A single sticky end is insufficient to drive preferential partitioning for the next linker size; for 202 bp, the linker preferentially partitions with overhangs on both ends of the dsDNA but not one end. The partition coefficient of the intermediate length linker, 278 bp, with two overhangs is about one, indicating that the concentrations of dsDNA that partitions into the droplet is equal to the concentration of dsDNA in the NS-dilute phase. (Fig. 4.2B and Fig. 4.3C, D). Interestingly, we also observed a tendency for linkers to accumulate on the droplet surface in this case and several others. Linkers longer than 202 bp with two overhangs and 202 and 278 bp linkers with one overhang create a core-shell-like structure where the concentration at the surface of the drop is higher than in the interior of the drop and in the bulk solution (Fig. 4.3B, C). The accumulation of
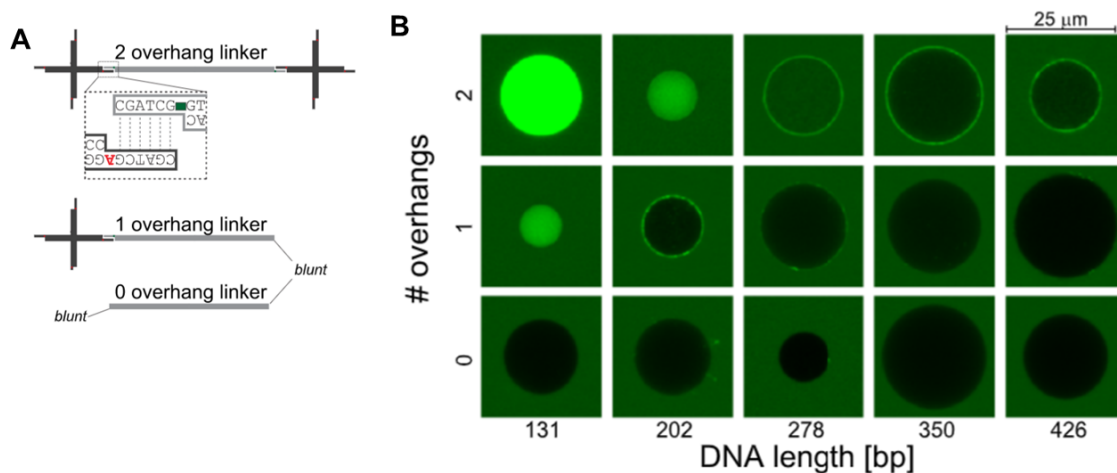
Figure 4.2: **Double-stranded DNA partitioning into NS-liquids** (A) Experimental design: linear dsDNA linkers of various lengths, and with 0, 1, or 2 overhangs are mixed with NSs. Linker overhangs match those of the NSs (except for the presence of an internal Cy3 dye/abasic site, green square), permitting specific NS–linker binding. (B) Representative images of fluorescently labeled linkers of various lengths and overhang numbers, interacting with droplets of unlabeled NSs. The images are confocal measurements through the droplet midplane. Mixtures were equilibrated through extensive incubation at 23°C.

linkers on the droplet surface was ignored in calculating P.

4.3.3   DsDNA partitioning model

As with dextran, we calculated $I(r)$, the radial intensity profile for each linker type (Fig. 4.3A–C). From $I(r)$, we quantified the accumulation of linkers on the surface and showed that the concentration within the drop is homogeneous (ignoring the surface enhancement) indicating that we are at equilibrium. To understand the effects of solute length and NS–solute interactions on linker partitioning, we propose a thermodynamic model that states that, in equilibrium, partitioning into the dense phase creates an entropic penalty that is balanced by the attractive base pairing energetics. In the model,
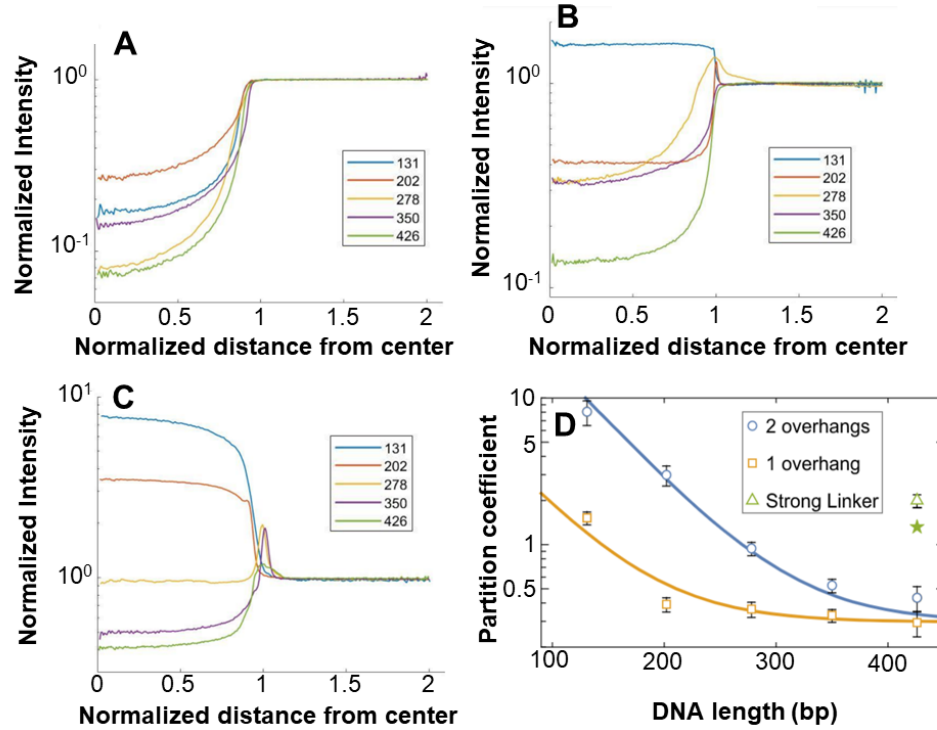
Figure 4.3: (A–C) Fluorescent intensity profiles (from the center of a NS-liquid droplet into bulk solution) of Cy3-tagged dsDNA partitioning into NS droplets. For each overhang condition ((A) 0 (B) 1, or (C) 2 overhangs), there is a representative curve for each dsDNA length under study. Fluorescence is normalized to the signal from bulk solution and radius is normalized to the droplet radius. (D) Partition coefficients vs. length for single- and double-overhang linkers (squares and circles, respectively), as measured from images such as in Fig. 4.2B). Lines indicate fits to Eq. 4.4. Triangle: measured P of 426 bp strong linker (see Fig. 4.4). Star: P predicted from Eq. 4.4 for the strong linker using best-fit parameters adjusted for increased binding strength. For each data point, error bars indicate the standard error for at least 5 droplets.

the partition coefficient, P_n, of a linker with $n = \{1, 2\}$ overhangs is given by

$$P_n = e^{n\epsilon/2 - \alpha L} + b \tag{4.4}$$

where ϵ is the length-independent attraction energy between NSs and linkers; αL is the entropic penalty of confining a linker of length L within the NS-liquid meshwork; and $b = 0.30 \pm 0.04$ which accounts for background light that inflates the measured partition coefficient.

65

Based on previous work, we assume that all overhangs are fully bonded in the dense phase before and after linkers are added [34, 41]. In order to accommodate a linker with two overhangs into the NS-liquid, one NS–NS bond must first break. This means that if the linker begins unbound in solution, the net gain of two linker overhangs entering the dense phase is only one, i.e., an energy change of $0.5n\Delta G$ per linker, where ΔG is the overhang hybridization energy. This aligns with previous work, which found that at equilibrium, NS rearrangement within the dense phase is dictated by the thermodynamics of overhang hybridization [34, 41, 50, 69].

We compared the fit value of the free energy to the SantaLucia nearest neighbor model [132]. Eq. 4.4 gives a fit value of $\epsilon = 4.7 \pm 0.5\ k_B T$. The fit thus underestimates the free energy of binding, taken here to be identical for NS–NS and standard linker–NS bonds, which was calculated to be $\Delta G_{NS} \approx -7.5$ kcal/mol $\approx -13\ k_B T$ [132]. (Note that the calculated ΔG_{NS} is less here than in Chapter 3 because Jeon et al. (2018) accounted for the base stacking between the sticky end and the unpaired adenosine which is skipped here due to the abasic site on the linker [41].) We postulate that ϵ and ΔG_{NS} differ because one of our initial assumptions — that linkers are fully unbound in the dilute phase — is incorrect. Instead, it's possible that some fraction of overhangs, $\mathcal{F}$, are bound in solution. Adjusting the model to reflect that linker overhangs could be bound before entering the NS droplet and assuming that the free energy of binding is ΔG_{NS} changes the second term of the exponential to be $0.5n\Delta G(1-\mathcal{F})$. Fitting this to the data gives that $\mathcal{F} \approx 0.6$ indicating that linker overhangs are frequently bound in solution.

Odijk (1983) described the free energy penalty of confining a stiff polymer in an entangled network of mesh size ξ, which restricts the positional and orientational configurations of the polymer to within a virtual tube (i.e., a cylinder with a curved height axis that follows the polymer path) [76]. The polymer should be well described by the worm-like chain model, like dsDNA, and is expected to not interact with the walls of the virtual

Meaning	Variable	Value
Mesh size	ξ	9 nm
Persistence length	l_p	50 nm [113, 168]
Contour length	L	45 to 145 nm
Deflection length	λ	15 nm

Table 4.1: Relevant length scales for estimating free energy from confining linkers to NS meshwork.

tube except for hard-wall repulsion. Odijk argued against the common approximation that a polymer is perfectly stiff for length scales shorter than its persistence length, l_p and instead stated that polymers can bend on length scales shorter than l_p. When in the virtual tube, these fluctuations are restricted to being smaller than the diameter of the virtual tube, ξ. The deflection length scale, λ, describes the length beyond which the fluctuations become restricted. λ is given by

$$\lambda \propto \xi^{2/3} l_p^{1/3} \tag{4.5}$$

Odijk showed that adjusting the deflection length scale resulted in a model that more accurately aligned with previous experimental results.

Based on the length scales listed in Table 4.1, we determined that the linkers are in a regime where the increase in free energy due to confinement is described by

$$\Delta F \approx \frac{L}{\lambda} ln(l_p/\lambda) \tag{4.6}$$

where ΔF is given in units of $k_B T$. Eq. 4.6 shows a linear dependence on length, as is reflected in the fit (Eq. 4.4). From the global fit, we calculate the increase in free energy from confinement per unit length to be $\alpha = 0.055 \pm 0.007\ k_B T/$nm. The Odijk prediction gives $\frac{1}{\lambda} ln(l_p/\lambda) \approx 0.07\ k_B T/$nm, in good agreement with our results.
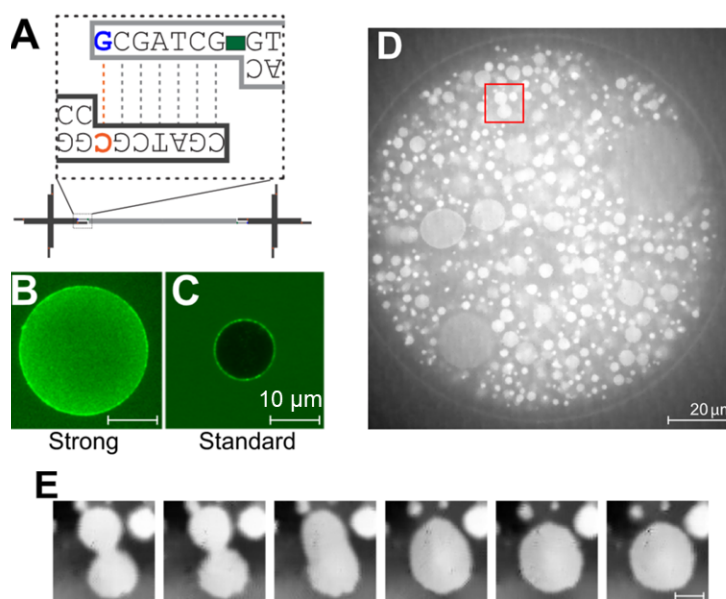
Figure 4.4: **Strong linker system** (A) Schematic of NS–strong linker-binding inter-action. Green square indicates the location of Cy3 dye. (B) NS droplet (unlabeled NSs) showing partitioning of 426 bp, Cy3-labeled strong linkers; conditions and sample preparation match those in in Fig. 4.2B including long incubation times. From such images, we estimate $P = 2.0 \pm 0.2$. (C) For comparison, repeated image from Fig. 4.2B image of partitioning of 426 bp, Cy3-labeled standard linker. (D) Long-lived, but nonequilibrium, structure showing internal droplets, rich in Cy3-labeled strong linkers, within a large NS droplet prepared in 50 mM NaCl and 8 mM MgCl$_2$. (E) Time series of highlighted area from (D) showing coalescence of internal droplets. Scale bar 2μm.

4.3.4   Strong linkers

We made two adjustments to the system to attempt to force the longest linkers into the droplet phase: (1) the unpaired base in NS overhangs was changed from an adenine to a cytosine; (2) the linker overhang sequence was extended to include a 5' guanine capable of binding said cytosine (Fig. 4.4A). The alterations to the NSs and linkers, which enable two extra base-stacking interactions, made NS–strong linker interactions prefered over NS–standard linker, strong linker–strong linker, or NS–NS bonds.

We observed that close-to-equilibrated solutions of 426 bp linkers with two strong overhangs are enriched in the NS droplet (Fig. 4.4b). These samples were prepared

68

using the same methods as was used for standard linkers, although the dimmer center of the drop indicates that the system has not yet reached equilibrium. We conclude that the stronger binding is able to compensate for the entropic confinement of these long strands. The partition coefficient of the strong linker was calculated to be $P = 2.0 \pm 0.2$ which we used to test our model: we applied Eq. 4.4 using the best-fit parameters to the standard-linker data, but augmenting the energetic factor, ϵ by a factor of 1.7. This accounted for the different overhang strengths $\Delta G_{NS} = -7.2$ kcal/mol vs $\Delta G_{strong} = -12.7$ kcal/mol. Eq. 4.4 predicts that $P_{2,strong} = 1.3$, in rough agreement with the measured value (Fig. 4.3D).

4.3.5   Internal droplets and core-shell structures

We showed that 426 bp strong linker partitioning depends on sample preparation. For example, we added the strong linkers to NS drops with 8 mM Mg^{2+} present in solution. Additionally, rather than waiting a long time between adding linkers and imaging, we pipette mixed the solution after adding linkers and imaged immediately. Instead of partitioning homogeneously, linker-dense droplets formed within the NS liquid (Fig. 4.4D). We determined that the internal droplets are liquid because they round up after coalescing (Fig. 4.4E). We observed many, large linker droplets soon after mixing, indicating that the demixing was spontaneous. Spinodal decomposition could be possible at such a low concentration of linkers because the large entropic confinement penalty of these long strands entering the NS liquid ($\alpha L \approx 8\ k_B T$) could alter the free energy landscape. We postulate that the internal droplets are metastable: linkers were forced into the dense phase via pipette mixing but will be ejected out of the large NS droplet to the external dilute solution, so as to reach the equilibrium state. This process is expected to be extremely slow, likely because of the high viscosity of the NS-liquid.

The observed surface enrichment of linkers can also be explained by the interplay of overhang energetics and entropic confinement: linkers on the droplet surface can still bind to NSs in the droplet but are not required to thread through the NS-liquid meshwork. The surface is thus a location where energetic gains are not offset by an entropic penalty, which accounts for the surface enhancement. Additionally, we observe that the surface enrichment is length dependent: single-overhang, long linkers do not form a core-shell structure where shorter linkers do (Fig. 4.2B). This may occur because the surface of the drop is not perfectly smooth. The thermal fluctuations could decrease the concentration of NSs at the surface of the drop, creating a mesh with an effective mesh size larger than that of the interior of the drop. Previous work has shown that the width of the interfacial regime, $\sqrt{k_B T/\sigma} \approx 60$ nm, is fairly broad. This *thermal roughening* would allow smaller linkers to accumulate on the surface of the drop but would exclude larger linkers.

4.3.6   Short linker partitioning

Eq. 4.4 suggests that there is a length of blunt dsDNA that can diffuse into the droplets despite not having NS attractions ($\approx$ 20 bp). Following the same protocol as Fig. 4.3b, we further provide support for Eq. 4.4 by showing that 20 bp linkers can partition into the dense phase without including overhangs.

Figure 4.5: 20 bp linkers (green, middle image) will partition into NS drops (untagged, bright field image that shows drops, left) without overhangs. Overlay(right) shows the homogeneous mixing of 20 bp linkers in both phases.

4.4 Conclusion

In this work, we focused on two physical parameters that influenced solute partitioning into NS-droplets. Both solutes exhibit size-dependent partitioning where smaller molecules can more easily move into the dense phase. Dextran, a neutral, branched polymer, was used to estimate the mesh size of the NS liquid, which was calculated to be approximately the length of a NS arm. Linear dsDNAs of different sizes were used to investigate the effects of the length of the solute and sequence-specific interactions with NSs. The length dependence is similar to that observed by dextran and is well modeled by the entropic confinement of a stiff polymer in an entangled mesh [76]. The entropic penalty can be overcome by adding overhangs to the ends of the linkers which allows the NSs and linkers to bind to each other; however, our model underestimates the free energy of hybridization of the overhangs. We propose that this indicates that linkers are often bound to one or two NSs in solution.

Finally, we observed two unexpected morphologies in this work. The first is a core-shell structure exhibited by the longer lengths of linear dsDNA with overhang interactions. We postulate that this structure occurs because the entropic penalty of confining the DNA to the exterior of the drop is less than the penalty of confining it to a mesh. We also observed inhomogeneous mixing of dsDNA that had modified linkers to strengthen linker–NS interactions. We believe that these dense-linker droplets occur when long linkers are forced into the dense phase via pipette mixing and are not an equilibrium state.

More recent works have combined the NS system with various solutes. For example, when orthogonal NS droplets are formed, incorporating the sticky end of one NS species has been shown to lead to selective partitioning of gene-length DNA and small proteins further supporting the energetic component of our model [26, 27]. Leather et al. (2022)

examined the kinetics of small ssDNA solutes that could bind to toeholds included on NSs that phase separate via cholesterol modifications on the end of each arm [169]. They observed that while smaller solutes enter the dense phase first, larger solutes with stronger NS–solute interactions displace them. The partitioning of DNA-binding proteins in another non-equilibrium (active) system has been shown to be temperature dependent [37]. This work proposes that the proteins "hitch a ride" as the NSs diffused within the liquid [37]. Finally, other works have focused on modulating the phase behavior of NSs with client molecules. For example, stiffening NS arms by including short ssDNA that fill in a gap included in the arms has been shown to promote phase separation [43]. These works show that programming solute partitioning with the NS system is straightforward and that the NS system can be used to quantify the properties that effect solute partitioning.

Chapter 5

Phase behavior of base-pairing DNA particles with polylysine

5.1 Introduction

Recent work has suggested that intracellular phase separation is driven by a combination of attractive self-interactions between particles of the same species and interactions between particles of different species. For example, a model system compared the phase behavior of a nucleolar protein in the presence and absence of a second nucleolar protein. They observed that the primary protein phase separates alone but measured a distinctly different phase diagram when the secondary protein was included [148]. Another model system composed of single stranded RNA and a positively charged polypeptide exhibits two phase separating regimes at differing concentrations of divalent salt ions. In the low salt regime, both the RNA and the polypeptide form complex coacervates, but in the high salt regime, only RNA is highly concentrated in the dense phase [170]. This indicates a switch between the attractions that drive phase separation in each salt regime: in the low salt regime, phase separation is driven by electrostatic attraction between the protein

and RNA while divalent-salt-induced non-cannonical base pairing of RNA induces phase separation in the high salt regime.

Here, we studied the interplay of two interactions that can drive phase separation: base pairing between NSs and electrostatic attraction between NSs and poly L-lysine (PLL), a positively charged amino acid chain. Polylysine–DNA condensation has been examined before: it is well documented that plasmid-length DNA and polylysine form organized toroidal structures under the right conditions [171, 172, 173]. In other conditions, the long, linear DNA form "fuzzy" compact structures with polylysine [173]. In addition, molecular dynamic simulations have shown that short chains of polylysine form complexes with a single strand of dsDNA. Although polylysine was shown to make contacts with both the major and minor grooves of the DNA, the amino acid chain does not align with the phosphate backbone of the DNA [174]. Rather, a single polylysine chain made multiple contacts with the dsDNA, but several amine groups remained separated from the DNA backbone between these contacts. Finally, recent works have used linear ss- and dsDNA oligomers with polylysine as a model system to probe the effects of flexibility, length, and base stacking on phase behavior and to create dynamic phase separating systems that respond to incident light or an applied electric field [175, 176, 177, 178].

We fluorescently tagged PLL and NSs with Fluorescein isothiocyanate (FITC) and Cy5, respectively, to examine their phase behavior (Fig. 5.1). We determine that phase behavior is highly salt dependent and that both NS–NS base pairing and NS–PLL electrostatic attraction play a role in determining the salt concentration for liquid-like behavior. Furthermore, we show that NS–PLL drops are stable at high temperature whereas NS drops (in the absence of PLL) are well known to dissolve at high temperature [34, 69]. Finally, we demonstrate that NSs with orthogonal sticky ends form immiscible complex coacervates, separate drops that both contain PLL. This sequence-specific separation does not persist when non-base-pairing NSs are combined with NSs with sticky ends and
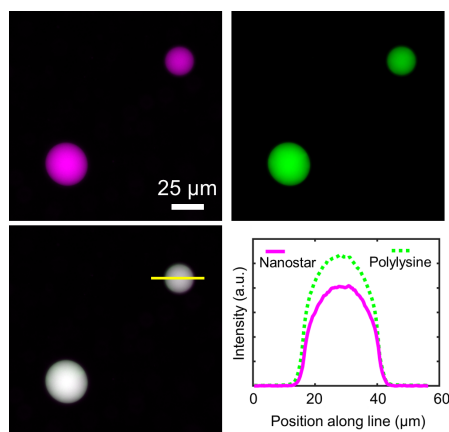
Figure 5.1: NSs (magenta, top left) and PLL (green, top right) colocalize into liquid drops. The bottom right shows the intensity vs position along the yellow line in the bottom left, merged image.

PLL. Overall, this system shows rich phase behavior because of surprisingly closely-tuned interactions which exhibit opposing responses to salt concentration.

5.2   Results

5.2.1   Phase diagram

We used fluorescent microscopy to image the material structures formed by PLL and NSs with sticky ends at varying charge ratios and monovalent salt concentrations. At a one-to-one charge ratio and low salt concentration, NSs and PLL form gel-like structures (Fig. 5.2D). When the salt concentration is increased to 1 M NaCl, NSs and PLL form liquid droplets that round up within minutes and coalesce (Fig. 5.2B). At the highest salt concentration tested, we observed a third phase, where DNA condenses into liquid drops which exclude PLL (Fig. 5.2A). A fourth regime emerges when the number of negative charges are outweighed by the number of positive charges (Fig. 5.2C). With an excess of NSs and at low salt, NSs form liquid drops with NS–PLL gels clustered on the exterior of the NS droplet.
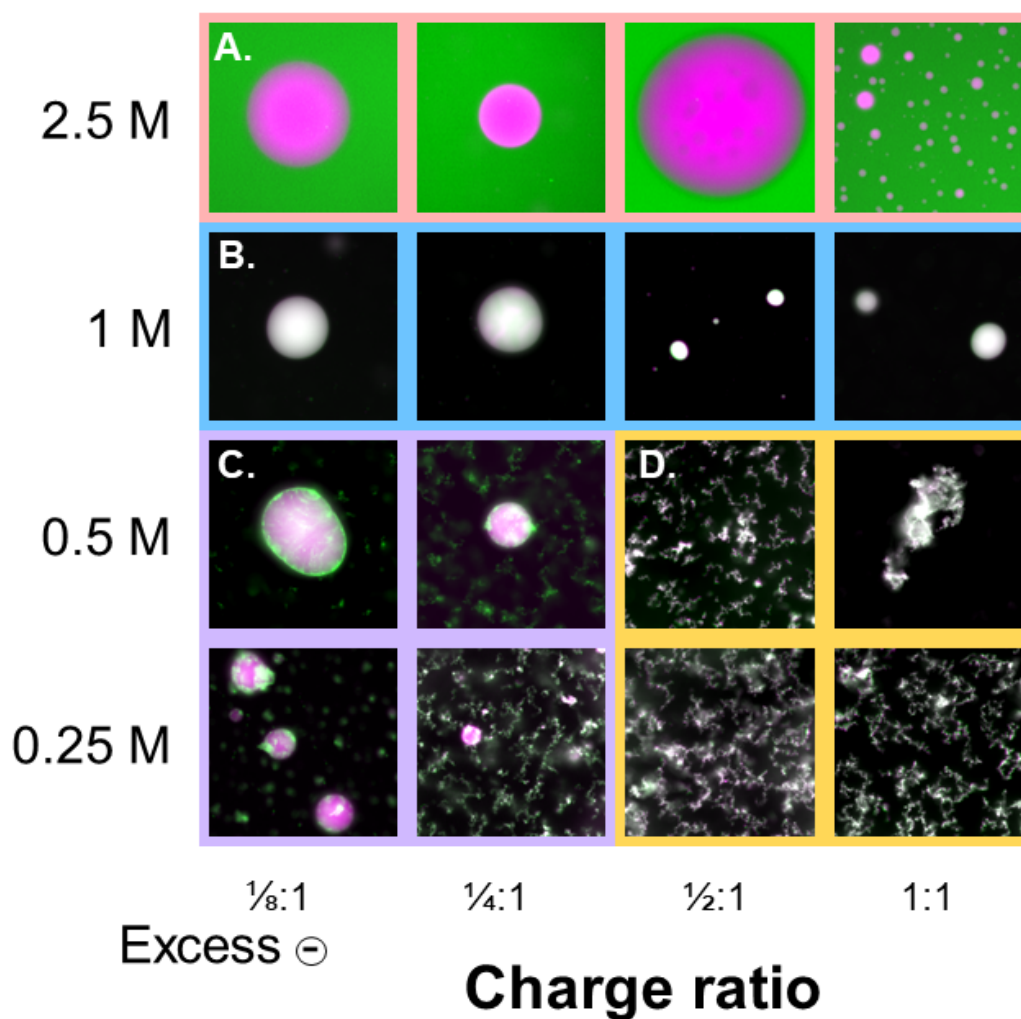
Figure 5.2: Representative images of each phase regime. In each case, the NSs are shown in magenta and PLL is shown in green. When NSs and PLL colocalize, they appear white. **(A) High salt regime:** At 2.5 M NaCl, NSs form drops that exclude PLL for all charge ratios. **(B) Intermediate salt regime:** NSs and PLL colocalize to form liquid-like drops for all charge concentrations. **(C) Low salt regime, large excess of NS:** NSs form drops that coexist with, but exclude, NS–PLL gels. **(D) Charge balanced, low salt regime:** NSs and PLL form colocalized gels. The dimensions of all images are 165×165 μm.
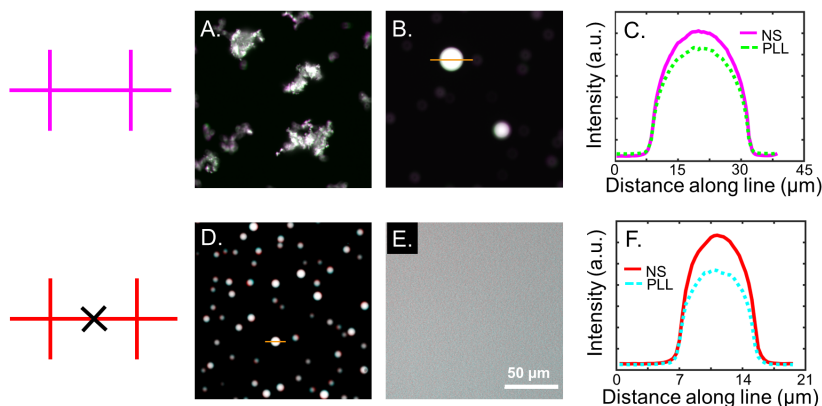
Figure 5.3: (A-C) Self-complementary NS (magenta) and PLL (green) form (A) gel–like aggregates at 0.5 M NaCl and (B) liquid drops at 1 M NaCl. (C) Intensity profile for both PLL and NSs along the orange line in B. (D-F) NSs that cannot base-pair (red) and PLL (cyan) form (D) liquid drops at 0.5 M NaCl and (E) do not phase separate at 1 M NaCl. (F) Intensity profile for both PLL and NSs along the orange line in D.

5.2.2   Liquid-like regime shifts with changing overhang

We compared the phase behavior of PLL in the presence of NSs with sticky ends and NSs with non-palindromic overhangs. At 0.5 M NaCl and a one-to-one charge ratio, NSs with sticky ends form gel-like structures (Fig. 5.3A); however, NSs with non-palindromic overhangs condense into liquid drops (Fig. 5.3D). NSs with sticky ends require a higher salt concentration (1 M NaCl) to form liquid drops (Fig. 5.3B) while NS without sticky ends do not phase separate at this higher salt concentration (Fig. 5.3E). For each case, NSs and PLL were shown to colocalize in the same region (Fig. 5.3C, F).

5.2.3   NS–PLL drops are stable at high temperature

It is well documented that NS droplets (in the absence of PLL) melt at high temperature because sticky end hybridization is temperature dependent (Fig. 5.4C) [34, 179]. When NSs and PLL form colocalized liquids, the droplets are stable at high temperatures over several hours (Fig. 5.4A). However, when NSs and PLL are combined in conditions

77

where NS condensates exclude PLL — e.g., 2.5 M NaCl (Fig. 5.4B) — the NS droplets melt at the same temperature as NSs in solution alone.
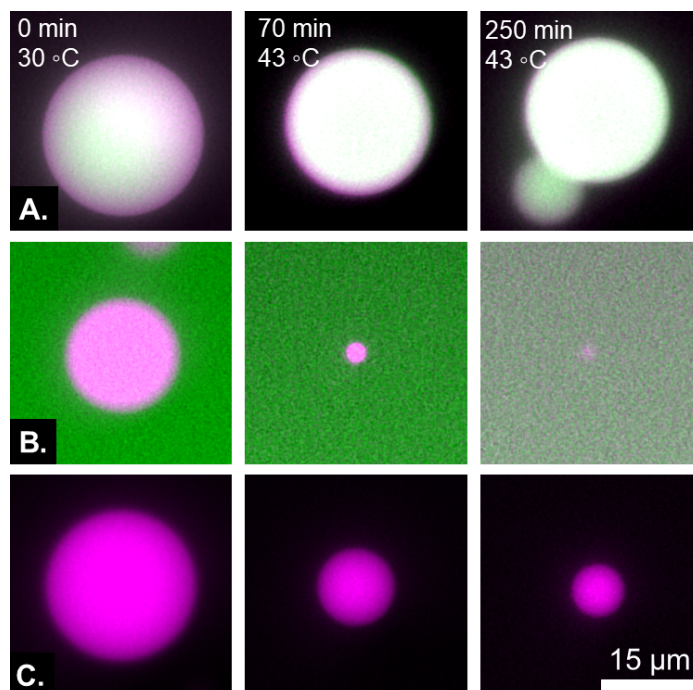
Figure 5.4: (A) NS(magenta)-PLL(green) droplets (1 M NaCl) do not melt at 43 °C, but NS drops that exclude PLL (B, 2.5 M NaCl) and NS drops alone (C) do melt at the same temperature.

5.2.4   Orthogonal base-pairing NSs exclude each other

We designed orthogonal NSs that contain self-complementary sticky ends that do not bind with the original NS sequence. We compared the structures that formed when multiple types of NSs (e.g., orthogonal and original sequence NSs; blunt and original sequence NSs) were combined with PLL (Fig. 5.5). At a one-to-one charge ratio and at 1 M NaCl, orthogonal NSs form drops with PLL that exclude the original sequence NSs, and vise versa. On the other hand, blunt NSs and original sequence NSs form colocalized drops with PLL. In the low-salt regime, both sets of NSs and PLL colocalize, regardless of sticky end sequence. Note that for this section, orthogonal NSs were not fluorescently

tagged. However, the original sequence NSs were excluded from some condensates and PLL does not condense alone; thus, I assert that condensates that are observed to be dense only in PLL are colocalized with untagged orthogonal NSs. In the low-salt, orthogonal NS case, there were no structures that excluded the original sequence NSs, so I posit that all three components were colocalized.
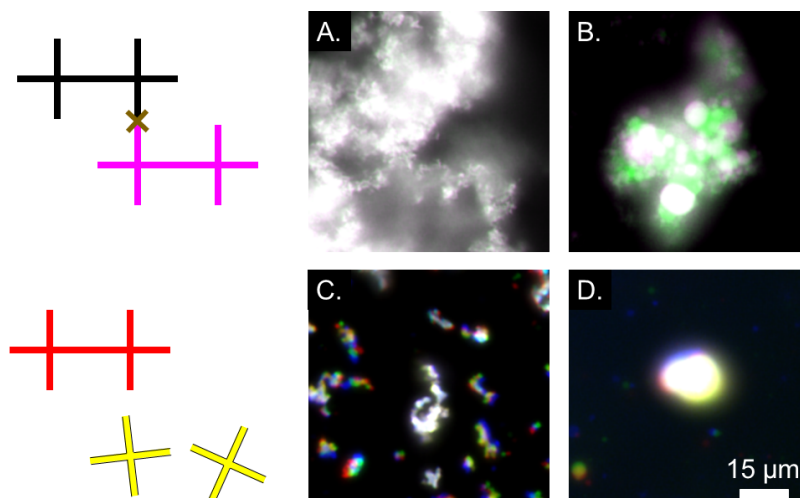
Figure 5.5: (A-B) Two NSs with orthogonal sticky ends (magenta and untagged) and PLL (green). (A) At 0.5 M NaCl, both types of NSs (with orthogonal sticky ends) and PLL colocalize. (B) At 1 M NaCl, drops of individual NS types form with PLL, but exclude orthogonal NSs. (C-D) Blunt NS (yellow) with self-complementary NS (red) and PLL (blue). Blunt NS, self-complementary NS, and PLL colocalize at both (C) 0.5 M NaCl and (D) 1 M NaCl.

5.3   Qualitative Discussion

The phase behavior of complex coacervation has been studied in several model systems. The transition from gel-like to liquid-like structures upon increasing salt concentration is well documented for electrostatically-driven coacervation — similar to the transition that is observed here for base pairing NSs and PLL between 0.5 M and 1 M NaCl [161, 180]. Qualitatively, electrostatically-driven complex coacervates become more

liquid-like at high salt concentration because the salt ions screen (i.e., weaken) the attractions between the macromolecules which allows them to rearrange, a defining property of liquids.

As the salt concentration is increased further, the attractive interactions continue to be weakened until they cannot overcome the entropy of mixing. Thus, for systems that condense strictly through electrostatic attraction, coacervates do not form above a critical salt concentration [119, 161]. Notable exceptions occur when additional interactions (e.g., hydrophobic interactions) become heightened at high salt concentration, resulting in re-entrant phase behavior [16, 181]. We postulate that the transition from NS–PLL liquid droplets to PLL-excluded NS droplets (i.e., the transition that occurs between 1 M NaCl to 2.5 M NaCl) can be explained in a similar way — that at higher salt concentration, the PLL–NS interactions are weakened such that the entropy gain of PLL remaining in solution exceeds the electrostatic attractions. On the other hand, because NS phase separation is driven by base-pairing, increasing salt concentration stabilizes inter-NS interactions and phase separation is promoted; thus PLL-excluding NS droplets form.

We observe that PLL–NS gels coated NS drops when the system was at low salt and far from charged balanced. Recent work with model systems composed of short nucleic acids and intrinsically disordered proteins that were far from charged balanced observed core-shell-like structures where the tails of the surplus polymer coated the exterior of the coacervate [182, 183]. Here, however, we observed the opposite — the polymer that is at a deficit (PLL) accumulates on the exterior of the drop that is composed of the polymer that is in an over-abundance (NSs). We suggest that this deviation occurs due to NS–NS binding. First, a subset of the NSs form gel-like coacervates with PLL such that the gels are charge balanced. The excess NSs then form NS-only liquid drops. Other systems have observed adhesion without encapsulation similar to what was observed here. In those systems, adhesion of orthogonal NS drops was driven by a small concentration of

surfactant NSs, but when the surfactant concentration was too high (i.e., the attraction between orthogonal NSs was strengthened), both types of NSs would mix [26]. Thus, we postulate that if gel-droplet adhesion is weak (e.g., if only a few sticky ends in the NS–PLL could bind with the NS droplet), the NS–PLL gel may accumulate on the side of the NS drop without fully entering the droplet phase.

The data show that NS–NS base pairing and NS–PLL electrostatic attraction can act cooperatively to determine phase behavior and dense phase properties. For example, sticky end NSs form gels with PLL in the same salt concentration where non-palindromic NSs form liquids. We postulate that base pairing slows down particle rearrangement such that the NSs and PLL become kinetically trapped in the gel phase. Additionally, NS–PLL liquid drops are stable at high temperature whereas NS droplets that do not incorporate PLL (e.g., drops made without PLL present and drops made in the high salt regime) melt at the same temperature, indicating that the incorporation of PLL results in structures that are more stable at high temperatures than NSs alone.

The multi-NS–PLL system ties together these conclusions. At 1 M NaCl, blunt NSs and PLL combine with the sticky end NSs to form liquids, but NSs with orthogonal sticky ends form droplets with PLL that are spatially distinct from original sequence NS–PLL droplets. We propose that if, first, sticky end NS and PLL form drops, blunt NSs can gain an enthalpic benefit from partitioning into the droplet phase because of the high concentration of PLL. NSs with orthogonal sticky ends can gain the same enthalpic benefit without being close to a second NS species by forming spatially distinct condensates with PLL. However, at the lower salt concentration, the electrostatic attraction between PLL and both species of NSs is strong enough to overcome the base pairing-driven inter-NS phase separation; thus, a three component coacervate is formed regardless of sticky ends. Small changes in system design result in large differences in phase behavior because the strength of both attractions are of similar strength, but exhibit opposing responses to

changing salt concentration.

5.4   Conclusion

We observe a surprising number of distinct behaviors in this system: at low salt concentrations, NSs and PLL either fully condense into gels or form coexisting NS–PLL gels and NS liquid drops. As the salt concentration is increased, the NS–PLL electrostatic attractions are weakened such that NSs and PLL condense into liquid drops. At an even higher salt concentration, NSs condense into drops which exclude PLL. The PLL-excluded NS-liquid phase only exists if NSs can base pair with each other; otherwise, NSs and PLL remain homogeneously mixed at high salt concentration. Additionally, the transition from NS–PLL gels to NS–PLL liquids is at a lower salt concentration when NS base pairing is removed. We show that both types of attractive interactions play a role in determining phase behavior. Comparing orthogonal sequence-specific interactions to blunt NS and sticky end NS shows that the phase behavior of this system is easily programmable. We are currently working to model this behavior by incorporating various interactions using what is known about electrostatics and base pairing phase transitions (as described in Chapter 2.)

Chapter 6

Conclusion and Future works

6.1 Conclusion

This thesis examines LLPS of a model, DNA-based system. LLPS is a vital means for sub-cellular organization; however the complex nature of intracellular phase separation has hindered examining the underlying principles of the process in its native environment. To better describe biomolecular condensation, some works have studied disordered chains of amino acids and nucleic acids as a model phase separating system. Here, I focus on the phase separation of NSs. Unlike other model LLPS systems, NS phase separation is driven by Watson-Crick-Franklin base pairing, so it is possible to isolate which dense phase properties can be directly linked to particle interactions and which cannot.

First, we examined the physical properties of the NS dense phase. We showed that these properties can be tuned using salt concentration and isolated which properties depend on inter-NS interactions and which do not. We determine that properties that depend on NS rearrangement, like viscosity and diffusivity, can be well described by the Arrhenius equation with an activation energy that is dependent on overhang hybridization thermodynamics. Interestingly, recent experimental work that characterized condensates

composed of disordered polypeptides and ssDNA showed that the viscosity and diffusivity are well modeled as Arrhenius processes as well [184]. The activation barrier of the polypeptide-ssDNA Arrhenius behavior was similar to the activation barrier used here, but varied widely depending on the polypeptide sequence. (From Chapter 3, $E_A = \Delta G_{NS} = 36 - 40$ kJ/mol; from Ref. [184], $E_A = 22 - 64$ kJ/mol.) Other properties in the NS system are better explained by increased electrostatic screening between arms of the same NS upon adding salt, which allows for more compact configurations. Finally, we showed that both NS drops and biomolecular condensates have a comparable viscosity, surface tension, and volume fraction of macromolecules in the dense phase.

In addition, we studied controlled solute partitioning into the dense phase. Locally concentrating some solutes while excluding others is a key property of biomolecular condensates. We observed size dependent partitioning where larger molecules are more excluded by the dense phase. For semi-flexible, linear polymers, this size-dependent exclusion was well described as an entropic penalty of confining the polymer to within the NS mesh [76]. Sequence-specific interactions could overcome the effects of entropic confinement to drive partitioning. To my knowledge, such rigorous characterization of partitioning into other biomolecular condensates has not yet been performed, although the effects of valency have begun to be investigated in model protein-based systems [166].

Finally, we combined NSs with a linear polycation, PLL. NSs without sticky ends and PLL phase separate at low salt and dissolve at high salt, similar to other electrostatically-driven phase separating systems. When we combine PLL and NSs with sticky ends, NSs form droplets that exclude PLL rather than dissolving at high salt. In addition, we showed that PLL with non-base pairing NSs exhibit liquid-like behavior at a lower salt concentration than PLL with sticky end NSs. We qualitatively suggest that incorporating both types of attractive interactions (base pairing and electrostatic) slows down particle rearrangement in the dense phase and causes the gel phase to persist to higher salt

concentration. In addition, when the attraction between NSs and PLL is sufficiently screened, the entropic confinement in the dense phase prevents PLL partitioning. These results are similar to those of a recent work which showed that the phase separation of a nucleoli-based, phase separating protein is dependent on a combination of homotypic interactions (with other proteins of the same species) and heterotypic interactions (with proteins of different species/nucleic acids), similar to the combination of NS–NS and NS–PLL interactions [148].

Overall, this thesis highlights some aspects of biomolecular condensation that are well modeled using NS LLPS. In each of these works, we have investigated the impact of NS binding interactions. By isolating the impact of inter-particle interactions, we were able to investigate what other properties impact phase behavior, solute partitioning, and multicomponent phase separation. We anticipate that similar properties play a role in biomolecular condensation and these conclusions will prove to be helpful for understanding intracellular phase separation.

6.2   Future Works

NS materials remain an interesting system to investigate due to their ability to mimic intracellular phase separation, their potential for biomedical applications, and their simple, programmable nature that can be used to elucidate the physics of phase separation. That said, examining disordered phases of NSs is still in its infancy — both in terms of applications and using NSs as a model system.

Results here and in other works have shown that NS phase behavior is dependent on both inter- and intra-NS interactions. Arm length, NS valence, internal flexibility, and overhang binding thermodynamics have all been investigated [27, 39, 41, 43, 57]. However, additional foundational work is needed to create a model that fully explains

NS phase behavior. For example, altering internal NS flexibility has been examined in two ways: unpaired nucleotides at the junction of the NS and unpaired nucleotides in the center of each arm [43, 47]. Comparing these two systems would separate the effects of flexibility as an inherent NS property from the effects of specific design choices. In addition, most works that examine NS phase behavior include sticky ends on every arm, but it is possible to create NSs that have sticky ends on a subset of arms. For example, some applications require that a sticky end sequence be replaced with a functional group, reducing the valency without changing the arm number [38, 53]. Sterically, NSs with higher valence should have less configurational freedom of each arm; thus, it would be beneficial to isolate the effects of arm number and valency on NS phase behavior. Having a firm grasp on the impact of individual NS properties on phase behavior will facilitate in accurately predicting the correct NS design choices necessary to create a materials with specific, desired properties.

Finally, NSs have shown promise in many potential applications. Aptamer functionalized NS gels have been shown to target specific cells and have been used to delivere medicine to the interior of cancer cells [53, 73]. Additionally, some types of tumor cells were less prolific when cultured in DNA hydrogels [40, 74]. However, many of these works were preliminary. For example, delivery of medicine into cancer cells and slowing tumor growth were not compared to a non-cancerous control. Despite the success of these works, many more exploratory works are needed before moving to *in vivo* experiments with NSs [156]. Moreover, some works have used NS liquids as biomimetic condensates, but there are many more intracellular processes that can be modeled with NSs [75, 169, 185]. For example, stress granules are thought to partition RNA to protect it from degradation [5]. From the results here, it would be simple to drive sequence-specific RNA partitioning into the droplet phase; however, it is unclear if NSs could be designed such that RNA would be protected from degradation in the NS-dense phase. NSs also have the potential

to model aberrant phase transitions that have been linked to disease — for example the transition of liquid-like, DNA-repair condensates to a solid-like state has been implicated in ALS [20]. Currently, most NS works have examined the transition between liquid condensates and the fully dissolved state; however, it is possible to examine the transition from condensed NS liquids to gels. Modeling the liquid-gel transition with NSs may elucidate the origins of some diseases and reveal methods to treat them.

Appendix A

Methods

A.1 Methods used throughout

A.1.1 Creating NSs

Single-stranded DNA oligomers were purchased from Integrated DNA Technologies (IDT) as a dried powder. Generally, oligomers were standard desalted, but sometimes polyacrylamide gel electrophoresis (PAGE) or high-performance liquid chromatography (HPLC) purification oligomers were used. Before being opened, each tube was centrifuged with a benchtop centrifuge (2,000 × g) to prevent sample loss if DNA was lodged in the cap of the tube.

After centrifuging, oligomers were resuspended in 10 mM Tris HCl (pH 7.5, Sigma-Aldrich) such that the concentration was predicted to be between 100 and 200 μM based on the IDT-reported ng of DNA. Samples were then vortexed and centrifuged repeatedly and heated at 50 °C for 10 minutes to ensure that all DNA was well dissolved.

After returning to room temperature, the concentration of each oligomer was measured using a NanoDrop™ One. The oliogmers were then mixed stoichiometrically such

that the molar concentration of each oligomer was the same. NSs were then annealed by first incubating at 95 °C for 10 minutes. The temperature was then lowered at a rate of -0.5 °C/min until the sample reached 0 °C. NSs were stored at -20 °C after annealing and were incubated at 50 °C before use, a temperature at which the NS cores are stable, but NS sticky ends are not.

A.1.2   Cleaning NSs

Sometimes, impurities needed to be removed from NS stocks. To do so, we used Amicon®Ultra Centrifugal filters. Filters were first rinsed to remove potential impurities. We then used the large centrifugal filter (which the DNA can flow through) for 30 minutes to remove large impurities and then used a small centrifugal filter for 15 minutes to remove small impurities and reconcentrate NSs. Additionally, we showed that filling the sample to the maximum volume resulted in the highest yield. For individual oligomers of standard NSs (each oligomer 49 bp long), 100 kDa and 3 kDa filters work well; however, for NSs that have already been annealed, 0.22 μm and 50 kDa filters are necessary. Gel electrophoresis showed that there is minimal difference between filtering NSs before or after annealing; however, filtering NSs after annealing tended to result in a higher yield.

A.1.3   Calculated NS extinction coefficients

Often, it was necessary to determine the concentration of NSs after annealing them. The calculation of purely dsDNA or ssDNA is straightforward; however, NSs are a combination of ds- and ssDNA. The most accurate method of calculating the extinction coefficient was determined to be to take the weighted average of the ds- and ssDNA extinction coefficients. For example, for the standard NS used throughout this thesis there are 160 paired nucleotides and 36 unpaired nucleotides. Thus the extinction coefficient

Oligomer-ss or ds	Extinction coefficient (L/mol·cm)
Oligo 1 - ss	477600
Oligo 2 - ss	458600
Oligo 3 - ss	477600
Oligo 4 - ss	456400
Oligo 1 - ds	810842
Oligo 2 - ds	812797
Oligo 3 - ds	813785
Oligo 4 - ds	811742

Table A.1: Individual oligomer extinction coefficients

of a NS, ε_{NS}, was calculated to be:

$$\varepsilon_{NS} = \frac{160}{196}\varepsilon_{ds} + \frac{36}{196}\varepsilon_{ss} \tag{A.1}$$

where ε_{ss} is the extinction coefficient of the entire sequence single stranded and ε_{ds} depends on the extinction coefficient of each oligomer such that

$$\varepsilon_{ds} = \frac{(\varepsilon_{ds,1} + \varepsilon_{ds,3}) + (\varepsilon_{ds,2} + \varepsilon_{ds,4})}{2}. \tag{A.2}$$

Here the numerator is written to emphasize taking the average of each orthogonal set of oligomers, i.e., oligomers 1 and 3 do not base pair within an individual NS.

Each extinction coefficient for individual oligomers for the primary NS used in Chapter 5 is given in Table A.1. Thus, for the primary NS used in Chapter 5, the extinction coefficient used was $\varepsilon_{ds} = 1/2(\varepsilon_{ds,1} + \varepsilon_{ds,2} + \varepsilon_{ds,3} + \varepsilon_{ds,4}) = 1/2(810842 + 812797 + 813785 + 811742) = 1624583$ L/mol·cm, and the total extinction coefficient for nanostars was calculated to be $\varepsilon_{NS} = 1412066.7$ L/mol·cm.

A.1.4   Pre-forming NS droplets

If a low concentration of NSs (e.g., 10 μM) is flowed into a channel immediately after mixing, the drops formed will be small; thus, it is often convenient to "preform" NS drops, i.e., allow drops to coalesce into larger drops before flowing them into the channel. To do so, we first mixed the sample such that the NSs or salt was added last (to prevent the sedimentation of droplets while other components were being added.) The solution was then pipette mixed and placed on a tube rotator and left for several hours. This allowed NSs to coalesce without sedimenting and forming a single large drop. Preformed NSs were transferred to a channel with pipettes with cut tips which reduces the shear force on the NS drops. While the preformed NSs being pipetted and added to a channel, the tube and pipette were rotated by hand to prevent sedimentation as well.

NS drops were preformed in Chapters 3 and 4, but not in Chapter 5 because complex coacervates exhibit non-specific adhesion to plastic surfaces that NS drops do not.

A.1.5   Channel preparation

Unless otherwise described, channels were prepared by melting parafilm onto cleaned coverslips and microscope slides. The glass was cleaned by rinsing with acetone, isoproyl alcohol, and then water. They were quickly dried with high purity N_2. Immediately following rinsing, the glass was plasma cleaned for 10 minutes.

Channels were prepared immediately after cleaning by placing two strips of parafilm between the top coverslip and the bottom coverslip/slide. The parafilm was melted by slowly dragging a 700 °F soldering iron on the top coverslip over the parafilm. Channels were filled immediately after preparation. Often, the channels were sealed to prevent evaporation. This was done with epoxy resin that was close to setting or with optical glue that was cured with a UV light.

A.2   Chapter 3: Characterizing NS-liquids

A.2.1   Fluorescently tagged NSs

When fluorescent visualization is necessary, one of the DNA oligomers was replaced with a variant containing an internal Cy3 dye at the 3' end of the overhang. Cy3-tagged NSs were diluted 100-fold with untagged NSs for use in all experiments requiring fluorescence. Cy3-tagged NSs integrate homogeneously into NS-liquids.

A.2.2   Density and volume fraction

100 μL solutions of 5–15 mg/mL DNA NSs were prepared with 0.25, 0.5, or 1 M NaCl, with 1:100 molar ratio of YOYO-1:NSs. The NS solutions were incubated at 50 °C for 30 min and centrifuged at 3000×g for 100 min. Using a transilluminator (Invitrogen) for visualization, the DNA-dilute phase was removed via pipette. The DNA concentration of the resulting NS-liquid was then measured via absorbance at 260 nm using a Nanodrop One spectrophotometer (Thermo Fisher Scientific). Volume fraction was calculated from the measured mass concentration of DNA in the dense phase using the mass concentration of pure DNA, i.e., $\phi = C_{DNA}/(1.7 \text{ g/cm}^3)$ [186].

A.2.3   Microrheology

Mixtures of NS and 200 nm fluorescent beads (540 ex/560 em, FluoSpheres$^{\text{TM}}$ from Thermo Fisher Scientific) were added into 10 μL of tris buffer at [NaCl] of 0.25, 0.5, and 1 M and incubated overnight at room temperature on a rotator, thereby allowing formation of large (≥ 50 μm) spherical NS droplets. NS-liquid droplets were introduced into a flowcell (i.e. a coverslip–para-film–coverslip sandwich with a channel cut in the parafilm) using end-cut pipette tips, and subsequently sealed with epoxy. The mobility of

fluorescent beads in NS-liquids were tracked with confocal microscopy for > 100 min with 1 s intervals. $MSDs$ were calculated and fit to the form $MSD(t) \propto 4D_{probe}t^{\alpha}$, where α is the diffusive exponent, to estimate the diffusion coefficient, D_{probe}. Viscosities, η of DNA NS-liquids at different[NaCl] were then calculated using the Stokes–Einstein equation, $D_{probe} = k_B T/6\pi\eta r$, where k_B is the Boltzmann constant, $T = 293$ K is temperature, and $r = 100$ nm is the probe radius.

A.2.4 Fluorescence Recovery after photobleaching

Fluorescent NS-liquid droplets, containing a 99:1 mixture of untagged:Cy3-tagged NSs, were imaged using a Leica SP8 confocal microscope. Image acquisition and data analysis was carried out following the method described by Seiffert and Oppermann [117]. Briefly, samples were imaged (512×512 pixels) using an objective with low numerical aperture ($10\times$; 0.3 NA) with $20\times$ zoom. A point was bleached with 550 nm excitation(10 s at 50% laser power, which was measured to be about 0.5 mW at the sample level) and fluorescent recovery was examined over 558–717 nm emission at 2, 5, and 5 s intervals for 0.25, 0.5, and 1 M [NaCl], respectively. The average fluorescent intensity, $I(r)$, at a given radius from the bleached spot, r,was calculated at each recovery time point and fit to the equation $I(t,r) = I_0(t) - A(t)e^{-r^2/2s(t)^2}$, where s^2 is the time-dependent variance of the Gaussian function.

A.2.5 Coalescence experiments

Coalescence was observed for fluorescent NS-liquid droplets on a flat oil/water interface[]. Briefly, a flow cell was prepared where the surface of the bottom coverslip was made hydrophobic with Sigmacote (Sigma-Aldrich). 2% of PFPE–PEG–PFPE triblock-copolymer surfactant (E2K0660; RAN Biotechnologies, Inc.) in 3M Novec$^{\text{TM}}$ 7500

Engineered Fluid (3M) was prepared and wicked into the flow cell. Then, an aqueous so-lution of preformed NS-liquid droplets in the salt of interest was flowed into the flow cell. The result is a flat oil/water interface where individual NS-liquid droplets can diffuse laterally, with minimal friction, to encounter and coalesce with other droplets. Coa-lescence events were recorded with confocal microscopy (Visitech), where 3D volumes were captured with 10 s intervals at 561 nm excitation.To calculate surface tensions, we use a formulation by Leal that shows, at late stages, the relaxation timescale, τ, of the transformation of an elliptical droplet into a spherical one is dictated by the ratio of the internal and external viscosities ($\lambda = \frac{\eta_{in}}{\eta_{out}}$), the radius of the droplet R, and the surface tension σ [154]. We calculate τ as the decay time scale of the dimensionless parameter $A = (L - W)/(L + W)$, which is a ratio of the difference and sum of the length (L) and width(W) of a deformed droplet during coalescence. Combining those results with mea-sured values of droplet radii and estimated viscosity values obtained from microrheology, surface tensions of NS-liquid droplets in various[NaCl] can be calculated from Eq. 3.9.

A.3   Chapter 4: dsDNA partitioning

A.3.1   DsDNA linker generation

DsDNA linkers were generated via autosticky PCR, where overhangs can be added to extension products through the use of primers containing internal abasic sites (Integrated DNA Technologies) [187]. Phusion DNA polymerase was used for PCR. See Table XX for linker sequences, including overhangs and the duplex regions.

A.3.2   Confocal Microscopy

For visualization, samples were added to flow cells constructed from thin glass cover slips, as described in Section B.1.4. Samples were prepared by first incubating ≥ 10 μM NSs in 1 M NaCl on a rotator for ≥ 1 h at room temperature, thereby allowing NS-liquid droplets to form. The solute of interest, either FITC-dextran (Sigma-Aldrich) or dsDNA linker, was then added with subsequent incubation for ≥ 1 h at room temperature. Mixtures were added to flow cell channels using a cut pipette tip and then sealed with epoxy to minimize evaporation. Flow cells were stored overnight at 23 °C before imaging.

Confocal microscopy was performed using a Leica SP8 Resonant Scanning confocal microscope with an Okolab stage top incubator and objective heater. Once the system reached a constant temperature of 23 °C, samples were placed on the stage and imaged using a 63×/1.3 NA glycerol objective with 533 nm excitation. Images were captured using 8× line averaging and 2× frame averaging, which limited photobleaching.

A.3.3   Partition Coefficient Quantification

We analyzed the fluorescent images of droplets to quantify the partition coefficient, P, that is, the ratio of solute concentration in the dense liquid relative to that in the dilute solution. Image analysis proceeded by finding the droplet center in the measured confocal plane and then using all pixel intensity values and distances from the center to construct a histogram of total intensity versus radius, r. This histogram was converted to the final radial intensity distribution, $I(r)$, by dividing the intensity in each bin by $2\pi r \Delta r$, where Δr is the bin width. Finally, P is estimated as the ratio of the average of I in the first 10 bins ($r \leq 0.7$ μ m), relative to the average in the droplet exterior. In this manner, spatial resolution enabled the separation of any added signal from surface enhancement from the internal bulk partitioning; that is, the signal near the droplet

surface was ignored when calculating P.

A.4 Chapter 5: NSs and PLL

A.4.1 NS formation

DNA oligomers were ordered from IDT. They were resuspended in 10 mM Tris-HCl before being mixed at equimolar concentrations. The mixture was then annealed by heating at 95 °C for 10 minutes followed by -0.5 °C/min. Proper NS formation was confirmed using agarose gel electrophoresis. NSs were stored at -20 °C between experiments.

A.4.2 Sample preparation

Each experiment was prepared following the same mixing order to reduce non-specific sticking of NS-PLL condensates to plastic surfaces. First, 10 mM Tris-HCl, 5 M NaCl, and water were combined and vortexed. Then PLL was added and pipette mixed. Before NSs were added, the flow channel was prepared. Finally, the NSs were added to solution with a cut pipette tip and the solution was pipette mixed three times before being added to the flow channel with the same pipette tip. If multiple species of NSs were included, they were combined before being added to the salt-PLL mixture such that all NSs were added in a single step.

A.4.3 Sample measurement

NS-PLL structures were placed in a flow channel made up of polyacrylamide coated slides and parafilm. Polyacrylamide slides were prepared using the same methodology found here [188]. Briefly, microscope slides and coverslips were heavily cleaned by Son-

icating with Hellmanex, ethanol, NaOH, and water. Slides were then incubated for 30 minutes in 3-(Trimethoxysilyl)poropylmethacrylate, ethanol, and acetic acid which had been degased. Slides were coated by leaving them in solution with acrylamide, TEMED, and ammonium persulfate overnight.

Immediately before use, slides were rinsed with water and dried with pure N_2 gas. Parafilm was melted onto the slide with a soldering iron such that a narrow channel was formed. Samples were added to the channel with a cut pipette tip to reduce shearing. Channels were sealed using Norland Optical Adhesive and that was cured with a UV light. Samples were immediately visualized using epifluorescent microscopy (Nikon Eclipse Ti2-E). Unless otherwise stated, samples were visualized at 25 $°C$ (Oko UNO).

Appendix B

DNA sequences

Below are each of the DNA sequences used throughout this thesis. The NSs are split into two tables: those that can phase separate via hybridization of sticky ends and those that cannot. All oligomer sequences are given 5'→3'.

Linkers used in Chapter 4:

131 bp:

CGAACTGTCCATGCTTGAGCTAATACGACTCACTATAGGGAGAGCGACTACGGTGA

GGGTCGGGTCCAGTAGCTTCGGCTACTGTTGAGTAGAGTGTGGGCTCCGTAGTCGC

CGTGGAACCTGCACCTCAC

202 bp:

TCATCACTAAAGAAATCCCGAGTAATACGACTCACTATAGGGAGAGATGTAACTGA

ATGAAATGGTGAAGGACGGGTCCAGTAGGCTGCTTCGGCAGCCTACTTGTTGAGTA

GAGTGTGAGCTCCGTAACTAGTTACATCCTAGCATAACCCCTTGGGGCCTCTAAAC

GGGTCTTGAGGGGTTTTTTGCCCGAGGAAATCAT

278 bp:

CGAACTGTCCATGCTTGAGCCGGCGTAGAGGATCGAGATCTCGATCCCGCGAAATT

AATACGACTCACTATAGGGGAATTGTGAGCGGATAACAATTCCCCTCTAGAAATAA

TTTTGTTTAACTTTAAGAAGGAGATATACATATGAGAGTTCTGGTTACCGGTGGTA

GCGGTTACATTGGAAGTCATACCTGTGTGCAATTACTGCAAAACGGTCATGATGTC

ATCATTCTTGATAACCTCTGTAACAGTAAGCGCAGCGTGGAACCTGCACCTCAC

350 bp:

CGAACTGTCCATGCTTGAGCCGGCGTAGAGGATCGAGATCTCGATCCCGCGAAATT

AATACGACTCACTATAGGGGAATTGTGAGCGGATAACAATTCCCCTCTAGAAATAA

TTTTGTTTAACTTTAAGAAGGAGATATACATATGAGAGTTCTGGTTACCGGTGGTA

GCGGTTACATTGGAAGTCATACCTGTGTGCAATTACTGCAAAACGGTCATGATGTC

ATCATTCTTGATAACCTCTGTAACAGTAAGCGCAGCGTACTGCCTGTTATCGAGCG

TTTAGGCGGCAAACATCCAACGTTTGTTGAAGGCGATATTCGTAACGAAGCCGTGG

AACCTGCACCTCAC

426 bp:

CGAACTGTCCATGCTTGAGCTAATACGACTCACTATAGGGAGAGCGACTACGGTGA

GGGTCGGGTCCAGTAGCTTCGGCTACTGTTGAGTAGAGTGTGGGCTCCGTAGTCGC

CTAGCATAACCCCGCGGGGCCTCTTCGGGGGTCTCGCGGGGTTTTTTGCTGAAAGA

AGCTTCAAATAAAACGAAAGGCTCAGTCGAAAGACTGGGCCTTTCGTTTTATCTGT

TGTTTGTCGCTGCGGCCGCACTCGAGCACCACCACCACCACCACTGAGATCCGGCT

GCTAACAAAGCCCGAAAGGAAGCTGAGTTGGCTGCTGCCACCGCTGAGCAATAACT

AGCATAACCCCTTGGGGCCTCTAAACGGGTCTTGAGGGGTTTTTTGCTGAAAGGAG

GAACTATATCCGGATCGTGGAACCTGCACCTCAC

Chapters	Oligomer number/total	Sequence
Chapters 3 & 4	Primary NS 1/4	CGA TCG CGT ACT ATG GCG GGT GAT AAA AAC GGG AAG AGC ATG CCC ATC C
Chapters 3 & 4	Primary NS 2/4	CGA TCG CGG ATG GGC ATG CTC TTC CCG AAC TCA ACT GCC TGG TGA TAC C
Chapters 3 & 4	Primary NS 3/4	CGA TCG CGG TAT CAC CAG GCA GTT GAG AAC ATG CGA GGG TCC AAT ACC C
Chapters 3 & 4	Primary NS 4/4	CGA TCG CGG GTA TTG GAC CCT CGC ATG AAT TTA TCA CCC GCC ATA GTA C
Chapter 5	Primary NS 1/4	CGA TCG ACG CTG CAA CTG GAG GAT ACG AAG CCG TGG CAA GTC AGG TGC G
Chapter 5	Primary NS 2/4	CGA TCG ACG GCT CAG TCG GTT TCC GAG AAC GTA TCC TCC AGT TGC AGC G
Chapter 5	Primary NS 3/4	CGA TCG ACG AGC GTT GGA CAT GTA TCG AAC TCG AAA ACC GAC TGA GCC G
Chapter 5	Primary NS 4/4	CGA TCG ACG CAC CTG ACT TGC CAC GGC AAC GAT ACA TGT CCA ACG CTC G
Chapter 5	Orthogonal NS 1/4	GCT AGC ACA CCG CCC GGG CAG AAC AGG AAC GGT GAT ATC CCG GGC CTC G
Chapter 5	Orthogonal NS 2/4	GCT AGC ACT TCG CCC GGG TGC TAA GAG AAC CTG TTC TGC CCG GGC GGT G
Chapter 5	Orthogonal NS 3/4	GCT AGC AGC CTT CCC GGG AGC GCT CGC AAC TCT TAG CAC CCG GGC GAA G
Chapter 5	Orthogonal NS 4/4	GCT AGC ACG AGG CCC GGG ATA TCA CCG AAG CGA GCG CTC CCG GGA AGG C

Table B.1: Nanostars with sticky ends

Chapters	Oligomer number/total	Sequence
Chapter 5	Blunt NS 1/4	TCG CTG CAA CTG GAG GAT ACG AAG CCG TGG CAA GTC AGG TGC G
Chapter 5	Blunt NS 2/4	TCG GCT CAG TCG GTT TCC GAG AAC GTA TCC TCC AGT TGC AGC G
Chapter 5	Blunt NS 3/4	TCG AGC GTT GGA CAT GTA TCG AAC TCG GAA ACC GAC TGA GCC G
Chapter 5	Blunt NS 4/4	TCG CAC CTG ACT TGC CAC GGC AAC GAT ACA TGT CCA ACG CTC G
Chapter 5	Non-palindromic NS 1/4	GGA ATT CCT GTA TCA GGC TCC GAT GCG CTT CAT ACT CTT CTT AAC AAC C
Chapter 5	Non-palindromic NS 2/4	GGA ATT CCT GGT TGT TAA GAA GAG TAT GTT CTG CCG CGC CTC GAG TCC C
Chapter 5	Non-palindromic NS 3/4	GGA ATT CCT GGG ACT CGA GGC GCG GCA GTT CCG CCA TCC CTC CAT TTC G
Chapter 5	Non-palindromic NS 4/4	GGA ATT CCT CGA AAT GGA GGG ATG GCG GTT GCG CAT CGG AGC CTG ATA C

Table B.2: Nanostars without sticky ends

Bibliography

[1] N. A. Yewdall, A. A. André, T. Lu, and E. Spruijt, *Coacervates as models of membraneless organelles, Current Opinion In Colloid And Interface Science* **52** (2021).

[2] N. Martin, L. Tian, D. Spencer, A. Coutable-Pennarun, J. L. R. Anderson, and S. Mann, *Photoswitchable phase separation and oligonucleotide trafficking in DNA coacervate microdroplets, Angewandte Chemie International Edition* **58** (2019) 14594–14598.

[3] B. R. Sabari, A. Dall'Agnese, and R. A. Young, *Biomolecular condensates in the nucleus, Trends In Biochemical Sciences* **45** (2020).

[4] L. Peng, E. M. Li, and L. Y. Xu, *From start to end: Phase separation and transcriptional regulation, Biochimica Et Biophysica Acta (BBA) - Gene Regulatory Mechanisms* **1863** (2020) 194641.

[5] D. Campos-Melo, Z. C. Hawley, C. A. Droppelmann, and M. J. Strong, *The integral role of RNA in stress granule formation and function, Frontiers In Cell And Developmental Biology* **9** (2021) 808.

[6] S. Alberti, *Phase separation in biology, Current Biology* **27** (2017) 1097–1102.

[7] X. Tschurikow, A. Gadzekpo, M. P. Tran, R. Chatterjee, M. Sobucki, V. Zaburdaev, K. Göpfrich, and L. Hilbert, *Amphiphiles formed from synthetic DNA-nanomotifs mimic the dispersal of transcriptional clusters in the cell nucleus, BioRxiv* (2023).

[8] D. S. Vazquez, P. L. Toledo, A. R. Gianotti, and M. R. Ermácora, *Protein conformation and biomolecular condensates, Current Research In Structural Biology* **4** (2022) 285–307.

[9] M. T. Wei, S. Elbaum-Garfinkle, A. S. Holehouse, C. C. H. Chen, M. Feric, C. B. Arnold, R. D. Priestley, R. V. Pappu, and C. P. Brangwynne, *Phase behaviour of disordered proteins underlying low density and high permeability of liquid organelles, Nature Chemistry* **9** (2017) 1118–1125.

[10] W. M. Aumiller and C. D. Keating, *Experimental models for dynamic compartmentalization of biomolecules in liquid organelles: Reversible formation and partitioning in aqueous biphasic systems*, Advances In Colloid And Interface Science **239** (2017) 75–87.

[11] B. R. Sabari, A. Dall'Agnese, A. Boija, I. A. Klein, E. L. Coffey, K. Shrinivas, B. J. Abraham, N. M. Hannett, A. V. Zamudio, J. C. Manteiga, C. H. Li, Y. E. Guo, D. S. Day, J. Schuijers, E. Vasile, S. Malik, D. Hnisz, T. I. Lee, I. I. Cisse, R. G. Roeder, P. A. Sharp, A. K. Chakraborty, and R. A. Young, *Coactivator condensation at super-enhancers links phase separation and gene control*, Science **361** (2018).

[12] K. K. Nakashima, A. A. André, and E. Spruijt, *Enzymatic control over coacervation*, Methods In Enzymology **646** (2021) 353–389.

[13] J. K. A. Tom and A. A. Deniz, *Complex dynamics of multicomponent biological coacervates*, Current Opinion In Colloid And Interface Science **56** (2021) 101488.

[14] C. E. Sing and S. L. Perry, *Recent progress in the science of complex coacervation*, Soft Matter **16** (2020) 2885–2914.

[15] K. M. Ruff, F. Dar, and R. V. Pappu, *Ligand effects on phase separation of multivalent macromolecules*, Proceedings Of The National Academy Of Sciences Of The United States Of America **118** (2021).

[16] D. M. Shapiro, M. Ney, S. A. Eghtesadi, and A. Chilkoti, *Protein phase separation arising from intrinsic disorder: First-principles to bespoke applications*, Journal Of Physical Chemistry B **125** (2021) 6740–6759.

[17] M. Feric, N. Vaidya, T. S. Harmon, D. M. Mitrea, L. Zhu, T. M. Richardson, R. W. Kriwacki, R. V. Pappu, and C. P. Brangwynne, *Coexisting liquid phases underlie nucleolar subcompartments*, Cell **165** (2016) 1686–1697.

[18] C. P. Brangwynne, C. R. Eckmann, D. S. Courson, A. Rybarska, C. Hoege, J. Gharakhani, F. Jülicher, and A. A. Hyman, *Germline P granules are liquid droplets that localize by controlled dissolution/condensation*, Science **324** (2009) 1729–1732.

[19] K. K. Nakashima, M. A. Vibhute, and E. Spruijt, *Biomolecular chemistry in liquid phase separated compartments*, Frontiers In Molecular Biosciences **6** (2019) 21.

[20] A. Patel, H. O. Lee, L. Jawerth, S. Maharana, M. Jahnel, M. Y. Hein, S. Stoynov, J. Mahamid, S. Saha, T. M. Franzmann, A. Pozniakovski, I. Poser, N. Maghelli, L. A. Royer, M. Weigert, E. W. Myers, S. Grill, D. Drechsel, A. A. Hyman, and S. Alberti, *A liquid-to-solid phase transition of the ALS protein FUS accelerated by disease mutation*, Cell **162** (2015) 1066–1077.

[21] Y. Shin and C. P. Brangwynne, *Liquid phase condensation in cell physiology and disease*, Science **357** (2017).

[22] R. R. Poudyal, F. P. Cakmak, C. D. Keating, and P. C. Bevilacqua, *Physical principles and extant biology reveal roles for RNA-containing membraneless compartments in origins of life chemistry*, Biochemistry **57** (2018) 2509–2519.

[23] H. G. Hansma, *Better than membranes at the origin of life?*, Life **7** (2017) 28.

[24] S. Koga, D. S. Williams, A. W. Perriman, and S. Mann, *Peptide–nucleotide microdroplets as a step towards a membrane-free protocell model*, Nature Chemistry **3** (2011) 720–724.

[25] C. D. Crowe and C. D. Keating, *Liquid–liquid phase separation in artificial cells*, Interface Focus **8** (2018).

[26] B. J. Jeon, D. T. Nguyen, and O. A. Saleh, *Sequence-controlled adhesion and microemulsification in a two-phase system of DNA liquid droplets*, Journal Of Physical Chemistry B **124** (2020) 8888–8895.

[27] Y. Sato, T. Sakamoto, and M. Takinoue, *Sequence-based engineering of dynamic functions of micrometer-sized DNA droplets*, Science Advances **6** (2020).

[28] X. Jun-xia, Y. Hai-yan, and Y. Jian, *Microencapsulation of sweet orange oil by complex coacervation with soybean protein isolate/gum arabic*, Food Chemistry **125** (2011) 1267–1272.

[29] Y. Xu, M. Mazzawi, K. Chen, L. Sun, and P. L. Dubin, *Protein purification by polyelectrolyte coacervation: Influence of protein charge anisotropy on selectivity*, Biomacromolecules **12** (2011) 1512–1522.

[30] A. S. Indulkar, Y. Gao, S. A. Raina, G. G. Zhang, and L. S. Taylor, *Exploiting the phenomenon of liquid-liquid phase separation for enhanced and sustained membrane transport of a poorly water-soluble drug*, Molecular Pharmaceutics **13** (2016) 2059–2069.

[31] P. Šulc, F. Romano, T. E. Ouldridge, L. Rovigatti, J. P. K. Doye, and A. A. Louis, *Sequence-dependent thermodynamics of a coarse-grained DNA model*, The Journal Of Chemical Physics **137** (2012) 135101.

[32] M. E. Fornace, J. Huang, C. T. Newman, N. J. Porubsky, M. B. Pierce, and N. A. Pierce, *NUPACK: analysis and design of nucleic acid structures, devices, and systems*, ChemRxiv (2022).

[33] J. N. Zadeh, C. D. Steenberg, J. S. Bois, B. R. Wolfe, M. B. Pierce, A. R. Khan, R. M. Dirks, and N. A. Pierce, *NUPACK: analysis and design of nucleic acid systems*, J. Comput. Chem. **32** (2011) 170–173.

[34] S. Biffi, R. Cerbino, F. Bomboi, E. M. Paraboschi, R. Asselta, F. Sciortino, and T. Bellini, *Phase behavior and critical activated dynamics of limited-valence DNA nanostars*, Proceedings Of The National Academy Of Sciences **110** (2013) 15633–15637.

[35] F. Li, J. Tang, J. Geng, D. Luo, and D. Yang, *Polymeric DNA hydrogel: Design, synthesis and applications*, Progress In Polymer Science **98** (2019).

[36] Y. Shao, H. Jia, T. Cao, and D. Liu, *Supramolecular hydrogels based on DNA self-assembly*, Accounts Of Chemical Research **50** (2017) 659–668.

[37] O. A. Saleh, B. J. Jeon, and T. Liedl, *Enzymatic degradation of liquid droplets of DNA is modulated near the phase boundary*, Proceedings Of The National Academy Of Sciences Of The United States Of America **117** (2020) 16160–16166.

[38] N. Park, S. H. Um, H. Funabashi, J. Xu, and D. Luo, *A cell-free protein-producing gel*, Nature Materials **8** (2009) 432–437.

[39] S. Agarwal, D. Osmanovic, M. A. Klocke, and E. Franco, *The growth rate of DNA condensate droplets increases with the size of participating subunits*, ACS Nano **16** (2022) 11842–11851.

[40] M. Leo, E. Lattuada, D. Caprara, L. Salvatori, A. Vecchione, F. Sciortino, P. Filetici, and A. Stoppacciaro, *Treatment of kidney clear cell carcinoma, lung adenocarcinoma and glioblastoma cell lines with hydrogels made of DNA nanostars*, Biomaterials Science **10** (2022) 1304–1316.

[41] B. J. Jeon, D. T. Nguyen, G. R. Abraham, N. Conrad, D. K. Fygenson, and O. A. Saleh, *Salt-dependent properties of a coacervate-like, self-assembled DNA liquid*, Soft Matter **14** (2018) 7009–7015.

[42] N. Conrad, G. Chang, O. A. Saleh, and D. K. Fygenson, *Emulsion imaging of a DNA nanostar condensate phase diagram reveals valence and electrostatic effects*, J. Chem. Phys **157** (2022) 234203.

[43] T. Lee, S. Do, J. G. Lee, D.-N. Kim, and Y. Shin, *The flexibility-based modulation of DNA nanostar phase separation*, Nanoscale **13** (2021) 17638.

[44] R. A. Brady, W. T. Kaufhold, N. J. Brooks, V. Fodera, and L. D. Michele, *Flexibility defines structure in crystals of amphiphilic DNA nanostars*, Journal of Physics: Condens. Matter (2019).

[45] J.-H. Chen, M. E. A. Churchill, T. D. Tullius, N. R. Kallenback, and N. C. Seeman, *Construction and analysis of monomobile DNA junctions*, Biochemistry **27** (1988) 6032–6038.

[46] N. R. Kallenbach, R. lne Ma, and N. C. Seeman, *An immobile nucleic acid junction constructed from oligonucleotides*, Nature **305** (1983) 51–65.

[47] D. T. Nguyen and O. A. Saleh, *Tuning phase and aging of DNA hydrogels through molecular design*, Soft Matter **13** (2017) 5421–5427.

[48] S. H. Um, J. B. Lee, N. Park, S. Y. Kwon, C. C. Umbach, and D. Luo, *Enzyme-catalysed assembly of DNA hydrogel*, Nature Materials **5** (2006) 797–801.

[49] E. Cheng, Y. Xing, P. Chen, Yang, Y. Sun, D. Zhou, T. Xu, Q. Fan, and D. Liu, *A ph-triggered, fast-responding DNA hydrogel*, Angewandte Chemie International Edition **48** (2009) 7660–7663.

[50] S. Biffi, R. Cerbino, G. Nava, F. Bomboi, F. Sciortino, and T. Bellini, *Equilibrium gels of low-valence DNA nanostars: a colloidal model for strong glass formers*, Soft Matter (2015).

[51] Z. Xing, A. Caciagli, T. Cao, I. Stoev, M. Zupkauskas, T. O'Neill, T. Wenzel, R. Lamboll, D. Liu, and E. Eiser, *Microrheology of DNA hydrogels*, Proceedings Of The National Academy Of Sciences Of The United States Of America **115** (2018) 8137–8142.

[52] F. Bomboi, D. Caprara, J. Fernandez-Castanon, and F. Sciortino, *Cold-swappable DNA gels*, Nanoscale **11** (2019) 9691–9697.

[53] J. Li, C. Zheng, S. Cansiz, C. Wu, J. Xu, C. Cui, Y. Liu, W. Hou, Y. Wang, L. Zhang, I. T. Teng, H. H. Yang, and W. Tan, *Self-assembly of DNA nanohydrogels with controllable size and stimuli-responsive property for targeted gene regulation therapy*, Journal Of The American Chemical Society **137** (2015) 1412–1415.

[54] Y. Xing, E. Cheng, Y. Yang, P. Chen, T. Zhang, Y. Sun, Z. Yang, and D. Liu, *Self-assembled DNA hydrogels with designable thermal and enzymatic responsiveness*, Advanced Materials **23** (2011) 1117–1121.

[55] E. Lattuada, T. Pietrangeli, and F. Sciortino, *Interpenetrating gels in binary suspensions of DNA nanostars*, The Journal Of Chemical Physics **157** (2022) 135101.

[56] L. Rovigatti, F. Bomboi, and F. Sciortino, *Accurate phase diagram of tetravalent DNA nanostars*, The Journal Of Chemical Physics **140** (2014) 154903.

[57] N. Conrad, T. Kennedy, D. K. Fygenson, and O. A. Saleh, *Increasing valence pushes DNA nanostar networks to the isostatic point*, Proceedings Of The National Academy Of Sciences **116** (2019) 7238–7243.

[58] P. S. Weiss, *A conversation with Prof. Ned Seeman: Founder of DNA nanotechnology*, ACS Nano **2** (2008) 1089–1096.

[59] N. C. Seeman, *Nucleic acid junctions and lattices*, Journal Of Theoretical Biology **99** (1982) 237–247.

[60] E. Winfree, F. Liu, L. A. Wenzler, and N. C. Seeman, *Design and self-assembly of two-dimensional DNA crystals*, Nature **394** (1998) 539–544.

[61] N. C. Seeman and N. R. Kallenbach, *DNA branched junctions*, Annual Review Of Biophysics And Biomolecular Structure **23** (1994) 53–86.

[62] D. E. Wemmer, A. J. Wand, N. C. Seeman, and N. R. Kallenbach, *NMR analysis of DNA junctions: imino proton NMR studies of individual arms and intact junction*, Biochemistry **24** (1985) 5745–5749.

[63] S. M. Chen, F. Heffron, W. J. Chazin, and W. Leupin, *Two-dimensional 1H NMR studies of synthetic immobile holliday junctions*, Biochemistry **30** (1991) 766–771.

[64] X. Wang and N. C. Seeman, *Assembly and characterization of 8-arm and 12-arm DNA branched junctions*, Journal Of The American Chemical Society **129** (2007) 8169–8176.

[65] M. L. Petrillo, C. J. Newton, R. P. Cunningham, R. Ma, N. R. Kallenbach, and N. C. Seeman, *The ligation and flexibility of four-arm DNA junctions*, Biopolymers **27** (1988) 1337–1352.

[66] E. Cheng, Y. Xing, P. Chen, Y. Yang, Y. Sun, D. Zhou, L. Xu, Q. Fan, and D. Liu, *A pH-triggered, fast-responding DNA hydrogel*, Angewandte Chemie International Edition **48** (2009).

[67] X. Zhou, C. Li, Y. Shao, C. Chen, Z. Yang, and D. Liu, *Reversibly tuning the mechanical properties of a DNA hydrogel by a DNA nanomotor*, Chemical Communications **52** (2016) 10668–10671.

[68] J. Jin, Y. Xing, Y. Xi, X. Liu, T. Zhou, X. Ma, Z. Yang, S. Wang, and D. Liu, *A triggered DNA hydrogel cover to envelop and release single cells*, Advanced Materials **25** (2013) 4714–4717.

[69] F. Bomboi, S. Biffi, R. Cerbino, T. Bellini, F. Bordi, and F. Sciortino, *Equilibrium gels of trivalent DNA-nanostars: Effect of the ionic strength on the dynamics*, The European Physical Journal E **38** (2015) 1–8.

[70] F. Sciortino and E. Zaccarelli, *Equlibrium gels of limited valence colloids*, Current Opinion In Colloid And Interface Science **30** (2017) 90–96.

[71] J. Fernandez-Castanon, S. Bianchi, F. Saglimbeni, R. D. Leonardo, and F. Sciortino, *Microrheology of DNA hydrogel gelling and melting on cooling*, *Soft Matter* **14** (2018) 6431–6438.

[72] L. Zhang, J. Lei, L. Liu, C. Li, and H. Ju, *Self-assembled DNA hydrogel as switchable material for aptamer-based fluorescent detection of protein*, *Analytical Chemistry* **85** (2013) 11077–11082.

[73] M. Nishikawa, Y. Mizuno, K. Mohri, N. Matsuoka, S. Rattanakiat, Y. Takahashi, H. Funabashi, D. Luo, and Y. Takakura, *Biodegradable CpG DNA hydrogels for sustained delivery of doxorubicin and immunostimulatory signals in tumor-bearing mice*, *Biomaterials* **32** (2011) 488–494.

[74] J. Song, K. Im, S. Hwang, J. Hur, J. Nam, G. O. Ahn, S. Hwang, S. Kim, and N. Park, *DNA hydrogel delivery vehicle for light-triggered and synergistic cancer therapy*, *Nanoscale* **7** (2015) 9433–9437.

[75] D. T. Nguyen, B. J. Jeon, G. R. Abraham, and O. A. Saleh, *Length-dependence and spatial structure of DNA partitioning into a DNA liquid*, *Langmuir* **35** (2019) 14849–14854.

[76] T. Odijk, *On the statistics and dynamics of confined or entangled stiff polymers*, *Macromolecules* **16** (1983) 1340–1344.

[77] T. Bellini, R. Cerbino, and G. Zanchetta, *DNA-based soft phases.* Springer, 2012.

[78] P. M. Chaikin and T. C. Lubensky, *Principles of Condensed Matter Physics.* Cambridge University Press, 1995.

[79] J. N. Israelachvili, *Intermolecular and surface forces.* Academic Press, 2nd ed., 1992.

[80] A. L. Turner, M. Watson, O. G. Wilkins, L. Cato, A. Travers, J. O. Thomas, and K. Stott, *Highly disordered histone H1-DNA model complexes and their condensates*, *Proceedings Of National Academy Of Science* **115** (2018) 1840–1847.

[81] Y. Wang, Y. Zhu, G. Zeng, Y. Zhang, C. Zhang, and C. Feng, *How to construct DNA hydrogels for environmental applications: Advanced water treatment and environmental analysis*, *Small* **14** (2018) 1703305.

[82] J. Gačanin, C. V. Synatschke, and T. Weil, *Biomedical applications of DNA-based hydrogels*, *Advanced Functional Materials* **30** (2020) 1906253.

[83] L. Zhou, X. Jiao, S. Liu, M. Hao, S. Cheng, P. Zhang, and Y. Wen, *Functional DNA-based hydrogel intelligent materials for biomedical applications*, *Journal Of Materials Chemistry B* **8** (2020) 1991.

[84] N. Klocker, F. P. Weissenboeck, and A. Rentmeister, *Covalent labeling of nucleic acids*, Chem. Soc. Rev. **49** (2020) 8749.

[85] A. J. Simon, L. T. Walls-Smith, and K. V. Plaxco, *Exploiting the conformational-selection mechanism to control the response kinetic of a "smart" DNA hydrogel*, Analyst **143** (2018) 2531–2538.

[86] M. Doi, *Soft Matter Physics*. Oxford Univeristy Press, 2013.

[87] F. Brochard-Wyart, P. Nassoy, and P.-H. Puech, *Essentials of Soft Matter Science*. CRC Press, 2020.

[88] A. Jain and R. D. Vale, *RNA phase transitions in repeat expansion disorders*, Nature **546** (2017) 243–247.

[89] J. S. Kahn, Y. Hu, and I. Willner, *Stimuli-responsive DNA-based hydrogels: From basic principles to applications*, Accounts Of Chemical Research **50** (2017) 680–690.

[90] J. B. Lee, S. Peng, D. Yang, Y. H. Roh, H. Funabashi, N. Park, E. J. Rice, L. Chen, R. Long, M. Wu, and D. Luo, *A mechanical metamaterial made from a DNA hydrogel*, Nature Nanotechnology **7** (2012) 816–820.

[91] P. C. Hiemenz and T. P. Lodge, *Polymer Chemistry*. CRC Press, 2007.

[92] R. S. Lakes, *Viscoelastic Materials*. Cambridge Univeristy Publications, 2009.

[93] K. Liu, M. Shuai, D. Chen, M. Tuchband, J. Y. Gerasimov, J. Su, Q. Liu, W. Zajaczkowski, W. Pisula, K. Müllen, N. A. Clark, and A. Herrmann, *Solvent-free liquid crystals and liquids from DNA*, Chemistry Europe J **21** (2015) 4898–4903.

[94] P. G. de Gennes and J. Prost, *The Physics of Liquid Crystals*. Oxford Science Publications, 1995.

[95] L. Onsager, *The effects of shape on the interaction of colloidal particles*, Annals Of The New York Academy Of Sciences (1949).

[96] T. Bellini, G. Zanchetta, T. P. Fraccia, R. Cebrino, E. Tsai, G. P. Smith, M. J. Moran, D. M. Walba, and N. A. Clark, *Liquid crystal self-assembly of random sequence DNA oligomers*, Proceedings Of The National Academy Of Sciences **109** (2012) 1110–1115.

[97] M. Rossi, G. Zanchetta, S. Klussmann, N. A. Clark, and T. Bellini, *Propagation of chirality in mixtures of natural and enantiomeric DNA oligomers*, Physical Review Letters **110** (2013).

[98] T. P. Fraccia, G. P. Smith, L. Bethge, G. Zanchetta, G. Nava, S. Klussmann, N. A. Clark, and T. Bellini, *Liquid crystal ordering and isotropic gelation in solutions of four-base-long DNA oligomers*, ACS Nano **10** (2016).

[99] C.-Y. Park, D. K. Fygenson, and O. A. Saleh, *Electrostatics and depletion determine competition between 2D nematic and 3D bundled phases of rod-like DNA nanotubes*, Soft Matter **12** (2016) 5089–5095.

[100] M. Siavashpouri, C. H. Wachaur, M. J. Zakhary, F. Praetorius, H. Dietz, and Z. Dogic, *Molecular engineering of chiral colloidal liquid crystals using DNA origami*, Nature Materials **16** (2017) 849–856.

[101] I. W. Hamley, *Liquid crystal phase formation by biopolymers*, Soft Matter **6** (2010).

[102] F. Livolant and A. Leforestier, *Condensed phases of DNA: Structures and phase transitions*, Progress In Polymer Science **21** (1996) 1115–1164.

[103] G. Zanchetta, M. Nakata, M. Buscaglia, T. Bellini, and N. A. Clark, *Phase separation and liquid cyrstallization of complementary sequences in mixtures of nanoDNA oligomers*, Proceedings Of National Academy Of Science **105** (2007) 1111–1117.

[104] C. L. Schildkraut, J. Marmur, and P. Doty, *Determination of the base composition of deoxyribonucleic acid from its buoyant density in CsCl*, Journal Of Molecular Biology **4** (1962) 430–443.

[105] W. Liu, A. Samanta, J. Deng, C. O. Akintayo, and A. Walther, *Mechanistic insights into the phase separation behavior and pathway-directed information exchange in all-DNA droplets*, Angewandte Chemie **134** (2022).

[106] J. Pelta, F. O. Livolant, and J.-L. Sikorav, *DNA aggregation induced by polyamines and cobalthexamine*, Chemjournal = JOURNAL OF BIOLOGICAL CHEMISTRY, Commun. **271** (1996) 5656–5662.

[107] H. H. Strey, R. Podgornik, D. C. Rau, and V. A. Parsegian, *DNA–DNA interactions*, Current Opinion In Structural Biology **8** (1998) 309–313.

[108] A. Shakya and J. T. King, *DNA local-flexibility-dependent assembly of phase-separated liquid droplets*, Biophysical Journal **115** (2018) 11964–11969.

[109] A. D. Price and D. K. Schwartz, *DNA hybridization-induced reorientation of liquid crystal anchoring at the nematic liquid crystal/aqueous interface*, J. Am. Chem. Soc. **130** (2008).

[110] Y. Huang, W. Xu, G. Liu, and L. Tian, *A pure DNA hydrogel with stable catalytic ability produced by one-step rolling circle amplification*, Chem. Commun **53** (2017) 3038–3041.

[111] F. Livolant, A. M. Levelut, J. Doucet, and J. P. Benoit, *The highly concentrated liquid crystalline phase of DNA is columnar hexagonal*, Nature **339** (1989) 724–726.

[112] H. H. Strey, J. Wang, R. Podgornik, A. Rupprecht, L. Yu, V. A. Parsegian, and E. B. Sirota, *Refusing to twist: Demonstration of a line hexatic phase in DNA liquid crystals*, Physical Review Letters **84** (2000) 3105–3108.

[113] M. Rubinstein and R. H. Colby, *Polymer Physics.* Oxford University Press, 2003.

[114] G. Zanchetta, F. Giavazzi, M. Nakata, M. Buscaglia, R. Cerbino, N. A. Clark, and T. Bellini, *Right-handed double-helix ultrashort DNAyields chiral nematic phases with bothright- and left-handed director twist*, Proceedings Of The National Academy Of Sciences **107** (2012) 17497–17502.

[115] M. Nakata, G. Zanchetta, B. D. Chapman, C. D. Jones, J. O. Cross, R. Pindak, T. Bellini, and N. A. Clark, *End-to-end stacking and liquid crystal condensation of 6– to 20–base pair DNA duplexes*, Science **218** (2007) 1276–1279.

[116] C. R. Martin and P. Kohli, *The emerging field of nanotube biotechnology*, Nature Reviews **2** (2003) 29–37.

[117] S. Seiffert and W. Oppermann, *Systematic evaluation of FRAP experiments performed in a confocal laser scanning microscope*, Journal Of Microscopy **220** (2005) 20–30.

[118] S. Chandrasekhar, *Surface tension of liquid crystals*, Molecular Crystals And Liquid Crystals **2** (2007) 71–80.

[119] E. Spruijt, A. H. Westphal, J. W. Borst, M. A. C. Stuart, and J. V. D. Gucht, *Binodal compositions of polyelectrolyte complexes*, Macromolecules **43** (2010) 6476–6484.

[120] C. D. Keating and R. V. Pappu, *Liquid-liquid phase separation: A widespread and versatile way to organize aqueous solutions*, J. Phys. Chem. B (2021).

[121] S. Wilken, A. Chaderjian, and O. A. Saleh, *Hyperuniform phase-separated DNA droplets*, ArXiv (2022).

[122] P. J. Flory, *Thermodynamics of High Polymer Solutions*, The Journal Of Chemical Physics **10** (1942) 51.

[123] M. L. Huggins, *Theory of Solutions of High Polymers*, *Journal Of The American Chemical Society* **64** (1942) 1712–1719.

[124] J. T. G. Overbeek' and M. J. Voorn, *Phase separation in polyelectrolyte solutions: Theory of complex coacervation*, *Journal of Cellular and Comparative Physiology* (1957).

[125] M. S. Wertheim, *Fluids with highly directional attractive forces. II. Thermodynamic perturbation theory and integral equations*, *Journal Of Statistical Physics* **35** (1984) 35–47.

[126] M. S. Wertheim, *Fluids with highly directional attractive forces. I. Statistical thermodynamics*, *Journal Of Statistical Physics* **35** (1984) 19–34.

[127] A. E. Posey, A. S. Holehouse, and R. V. Pappu, *Phase separation of intrinsically disordered proteins*, *Methods In Enzymology* **611** (2018) 1–30.

[128] P. K. Jha, P. S. Desai, J. Li, and R. G. Larson, *pH and salt effects on the associative phase separation of oppositely charged polyelectrolytes*, *Polymers* **6** (2014) 1414–1436.

[129] C. G. D. Kruif, F. Weinbreck, and R. D. Vries, *Complex coacervation of proteins and anionic polysaccharides*, *Current Opinion In Colloid And Interface Science* **9** (2004) 340–349.

[130] E. Locatelli, P. H. Handle, C. N. Likos, F. Sciortino, and L. Rovigatti, *Condensation and demixing in solutions of DNA nanostars and their mixtures*, *ACS Nano* **11** (2017) 2094–2102.

[131] M. S. Wertheim, *Fluids with highly directional attractive forces. I. Statistical thermodynamics*, *Journal Of Statistical Physics* **35** (1984) 19–34.

[132] J. Santalucia and D. Hicks, *The thermodynamics of DNA structural motifs*, *Annu. Rev. Biophys. Biomol. Struct* **33** (2004) 415–455.

[133] F. Sciortino and E. Zaccarelli, *Reversible gels of patchy particles*, *Current Opinion In Solid State And Materials Science* **15** (2011) 246–253.

[134] H. Liu, S. K. Kumar, F. Sciortino, and G. T. Evans, *Vapor-liquid coexistence of fluids with attractive patches: An application of Wertheim's theory of association*, *The Journal Of Chemical Physics* **130** (2009) 044902.

[135] J. M. Choi, A. S. Holehouse, and R. V. Pappu, *Physical principles underlying the complex biology of intracellular phase transitions*, *Annual Review Of Biophysics* **49** (2020) 107–133.

[136] B. S. Schuster, R. M. Regy, E. M. Dolan, A. K. Ranganath, N. Jovic, S. D. Khare, Z. Shi, and J. Mittal, *Biomolecular condensates: Sequence determinants of phase separation, microstructural organization, enzymatic activity, and material properties*, Journal Of Physical Chemistry B **125** (2021) 3441–3451.

[137] S. Srivastava and M. V. Tirrell, *Polyelectrolyte complexation*, Advances In Chemical Physics **161** (2016) 499–544.

[138] T. S. Harmon, A. S. Holehouse, and R. V. Pappu, *Differential solvation of intrinsically disordered linkers drives the formation of spatially organized droplets in ternary systems of linear multivalent proteins*, New Journal Of Physics (2018).

[139] M. Castelnovo and J. F. Joanny, *Complexation between oppositely charged polyelectrolytes: Beyond the random phase approximation*, European Physical Journal E **6** (2001) 377–386.

[140] Y. H. Lin, J. Song, J. D. Forman-Kay, and H. S. Chan, *Random-phase-approximation theory for sequence-dependent, biologically functional liquid-liquid phase separation of intrinsically disordered proteins*, Journal Of Molecular Liquids **228** (2017) 176–193.

[141] A. V. Ermoshkin and M. O. D. L. Cruz, *A modified random phase approximation of polyelectrolyte solutions*, Macromolecules **36** (2003) 7824–7832.

[142] A. M. Rumyantsev, N. E. Jackson, B. Yu, J. M. Ting, W. Chen, M. V. Tirrell, and J. J. D. Pablo, *Controlling complex coacervation via random polyelectrolyte sequences*, ACS Macro Letters **8** (2019) 1296–1302.

[143] F. Spinozzi, M. G. Ortore, G. Nava, F. Bomboi, F. Carducci, H. Amenitsch, T. Bellini, F. Sciortino, and P. Mariani, *Gelling without structuring: A SAXS study of the interactions among DNA nanostars*, Langmuir **30** (2020) 15.

[144] J. SantaLucia, *A unified view of polymer, dumbbell, and oligonucleotide DNA nearest-neighbor thermodynamics*, Proceedings Of The National Academy Of Sciences Of The United States Of America **95** (1998) 1460–1465.

[145] A. A. Hyman, C. A. Weber, and F. Jülicher, *Liquid-liquid phase separation in biology*, Annu. Rev. Cell Dev. Biol **30** (2014) 39–58.

[146] A. Bremer, M. Farag, W. M. Borcherds, I. Peran, E. W. Martin, R. V. Pappu, and T. Mittag, *Deciphering how naturally occurring sequence features impact the phase behaviours of disordered prion-like domains*, Nature Chemistry **14** (2021) 196–207.

[147] T. J. Nott, E. Petsalaki, J. D. Forman-Kay, A. J. Baldwin, P. Farber, D. Jervis, E. Fussner, A. Plochowietz, T. D. Craggs, D. P. Bazett-Jones, and T. Pawson, *Phase transition of a disordered nuage protein generates environmentally responsive membraneless organelles*, Molecular Cell **57** (2015) 936–947.

[148] D. M. Mitrea, J. A. Cika, C. B. Stanley, A. Nourse, P. L. Onuchic, P. R. Banerjee, A. H. Phillips, C. G. Park, A. A. Deniz, and R. W. Kriwacki, *Self-interaction of NPM1 modulates multiple mechanisms of liquid–liquid phase separation*, Nature Communications **9** (2018) 1–13.

[149] D. M. Mitrea, B. Chandra, M. C. Ferrolino, E. B. Gibbs, M. Tolbert, M. R. White, and R. W. Kriwacki, *Methods for physical characterization of phase-separated bodies and membrane-less organelles*, Journal Of Molecular Biology **430** (2018) 4773–4805.

[150] J. Fernandez-Castanon, F. Bomboi, L. Rovigatti, M. Zanatta, A. Paciaroni, L. Comez, L. Porcar, C. J. Jafta, G. C. Fadda, T. Bellini, and F. Sciortino, *Small-angle neutron scattering and molecular dynamics structural study of gelling DNA nanostars*, The Journal Of Chemical Physics **145** (2016) 84910.

[151] T. Scientific, *NanoDrop One User Guide*. ThermoFisher Scientific.

[152] D. J. Tritton, *Physical Fluid Dynamics*. Oxford Science Publications, 2nd ed., 1977.

[153] R. H. Perry and D. W. Green, *Perry's Chemical Engineer Handbook*. McGraw-Hill, 7th ed., 1999.

[154] L. G. Leal, *Advanced transport phenomena: Fluid mechanics and convective transport processes*. Cambridge University Press, 2007.

[155] H. Zhang, S. Elbaum-Garfinkle, E. M. Langdon, A. A. Bridges, C. P. Brangwynne, and A. S. Gladfelter, *RNA controls polyQ protein phase transitions*, Molecular Cell **60** (2015) 220–230.

[156] E. Lattuada, M. Leo, D. Caprara, L. Salvatori, A. Stoppacciaro, F. Sciortino, and P. Filetici, *DNA-GEL, novel nanomaterial for biomedical applications and delivery of bioactive molecules*, Frontiers In Pharmacology **11** (2020) 1345.

[157] A. M. Tayar, F. Caballero, T. Anderberg, O. A. Saleh, M. C. Marchetti, and Z. Dogic, *Controlling liquid-liquid phase behavior with an active fluid*, ArXiv (2022).

[158] H. Bohidar, P. L. Dubin, P. R. Majhi, C. Tribet, and W. Jaeger, *Effects of protein-polyelectrolyte affinity and polyelectrolyte molecular weight on dynamic properties of bovine serum albumin-poly(diallyldimethylammonium chloride) coacervates*, Biomacromolecules **6** (2005) 1573–1585.

[159] E. Spruijt, J. Sprakel, M. A. C. Stuart, and J. V. D. Gucht, *Interfacial tension between a complex coacervate phase and its coexisting aqueous phase*, *Soft Matter* **6** (2009) 172–178.

[160] M. Zhao, J. Zhou, C. Su, L. Niu, D. Liang, and B. Li, *Complexation behavior of oppositely charged polyelectrolytes: Effect of charge distribution*, *The Journal Of Chemical Physics* **142** (2015) 204902.

[161] D. Priftis, R. Farina, and M. Tirrell, *Interfacial energy of polypeptide complex coacervates measured via capillary adhesion*, *Langmuir* **28** (2012) 8721–8729.

[162] J. van der Gucht, E. Spruijt, M. Lemmers, and M. A. C. Stuart, *Polyelectrolyte complexes: bulk phases and colloidal systems*, *Journal Of Colloid And Interface Science* **361** (2011) 407–422.

[163] E. Spruijt, F. A. Leermakers, R. Fokkink, R. Schweins, A. A. V. Well, M. A. C. Stuart, and J. V. D. Gucht, *Structure and dynamics of polyelectrolyte complex coacervates studied by scattering of neutrons, x-rays, and light*, *Macromolecules* **46** (2013) 4596–4605.

[164] J. Berry, S. C. Weber, N. Vaidya, M. Haataja, C. P. Brangwynne, and D. A. Weitz, *RNA transcription modulates phase transition-driven nuclear body assembly*, *Proceedings Of The National Academy Of Sciences Of The United States Of America* **112** (2015) 5237–5245.

[165] M. T. Wei, S. Elbaum-Garfinkle, A. S. Holehouse, C. C. H. Chen, M. Feric, C. B. Arnold, R. D. Priestley, R. V. Pappu, and C. P. Brangwynne, *Phase behaviour of disordered proteins underlying low density and high permeability of liquid organelles*, *Nature Chemistry* **9** (2017).

[166] J. A. Ditlev, L. B. Case, and M. K. Rosen, *Who's in and who's out—compositional control of biomolecular condensates*, *Journal Of Molecular Biology* **430** (2018) 4666–4684.

[167] S. F. Banani, A. M. Rice, W. B. Peeples, Y. Lin, S. Jain, R. Parker, and M. K. Rosen, *Compositional control of phase-separated cellular bodies in brief what are the general principles that define the composition of phase-separated cellular bodies?*, *Cell* **166** (2016) 651–663.

[168] G. S. Manning, *The persistence length of DNA is reached from the persistence length of its null isomer through an internal electrostatic stretching force*, *Biophysical Journal* **91** (2006) 3607.

[169] A. Leathers, M. Walczak, R. A. Brady, A. A. Samad, J. Kotar, M. J. Booth, P. Cicuta, and L. D. Michele, *Reaction-diffusion patterning of DNA-based artificial cells*, *Journal Of The American Chemical Society* **144** (2022) 17468–17476.

[170] P. L. Onuchic, A. N. Milin, I. Alshareedah, A. A. Deniz, and P. R. Banerjee, *Divalent cations can control a switch-like behavior in heterotypic and homotypic RNA coacervates*, *Scientific Reports* **9** (2019) 1–10.

[171] G. Liu, M. Molas, G. A. Grossmann, M. Pasumarthy, J. C. Perales, M. J. Cooper, and R. W. Hanson, *Biological properties of poly-L-lysine-DNA complexes generated by cooperative binding of the polycation*, *The Journal Of Biological Chemistry* **276** (2001) 34379–34387.

[172] W. Zauner, M. Ogris, and E. Wagner, *Polylysine-based transfection systems utilizing receptor-mediated delivery*, *Advanced Drug Delivery Reviews* **30** (1998) 97–113.

[173] E. Wagner, M. Cotten, R. Foisner, and M. L. Birnstiel, *Transferrin-polycation-DNA complexes: the effect of polycations on the structure of the complex and DNA delivery to cells*, *Proceedings Of The National Academy Of Sciences Of The United States Of America* **88** (1991) 4255–4259.

[174] J. Ziebarth and Y. Wang, *Molecular dynamics simulations of DNA-polycation complex formation*, *Biophysical Journal* **97** (2009) 1971–1983.

[175] W. A. Wee, H. Sugiyama, and S. Park, *Photoswitchable single-stranded DNA-peptide coacervate formation as a dynamic system for reaction control*, *IScience* **24** (12, 2021) 103455.

[176] Y. Yin, L. Niu, X. Zhu, M. Zhao, Z. Zhang, S. Mann, and D. Liang, *Non-equilibrium behaviour in coacervate-based protocells under electric-field-induced excitation*, *Nature Communications* **7** (2, 2016) 1–7.

[177] J. R. Vieregg, M. Lueckheide, A. B. Marciel, L. Leon, A. J. Bologna, J. R. Rivera, and M. V. Tirrell, *Oligonucleotide-peptide complexes: Phase control by hybridization*, *Journal Of The American Chemical Society* **140** (2018) 1632–1638.

[178] T. P. Fraccia and T. Z. Jia, *Liquid crystal coacervates composed of short double-stranded dna and cationic peptides*, *ACS Nano* **14** (11, 2020) 15071–15082.

[179] Y. A. G. Fosado, Z. Xing, E. Eiser, M. Hudek, and O. Henrich, *A numerical study of three-armed DNA hydrogel structures*, *ArXiv* (2019).

[180] Q. Wang and J. B. Schlenoff, *The polyelectrolyte complex/coacervate continuum*, *Macromolecules* **47** (2014) 3108–3116.

[181] G. Krainer, T. J. Welsh, J. A. Joseph, J. R. Espinosa, S. Wittmann, E. de Csilléry, A. Sridhar, Z. Toprakcioglu, G. Gudiškytė, M. A. Czekalska, W. E. Arter, J. Guillén-Boixet, T. M. Franzmann, S. Qamar, P. S. George-Hyslop, A. A. Hyman, R. Collepardo-Guevara, S. Alberti, and T. P. Knowles, *Reentrant liquid*

condensate phase of proteins is stabilized by hydrophobic and non-ionic interactions, Nature Communications **12** (2021) 1–14.

[182] I. Alshareedah, M. M. Moosa, M. Raju, D. A. Potoyan, and P. R. Banerjee, *Phase transition of RNA-protein complexes into ordered hollow condensates*, Proceedings Of The National Academy Of Sciences Of The United States Of America **117** (2020) 15650–15658.

[183] I. Alshareedah, G. M. Thurston, and P. R. Banerjee, *Quantifying viscosity and surface tension of multicomponent protein-nucleic acid condensates*, Biophysical Journal **120** (2021) 1161–1169.

[184] I. Alshareedah, A. Singh, A. Quinn, and P. R. Banerjee, *Determinants of viscoelasticity and flow activation energy in biomolecular condensates*, BioRxiv (2022).

[185] D. T. Nguyen, *Self-assembling DNA complexes: an in vitro platform to probe the relation between transcription and condensed DNA phases*, PhD Thesis From Univeristy Of California, Santa Barbara (2018).

[186] G. Macaya, J. P. Thiery, and G. Bernardi, *An approach to the organization of eukaryotic genomes at a macromolecular level*, Journal Of Molecular Biology **108** (1976) 237–254.

[187] J. Gál, R. Schnell, S. Szekeres, and M. Kálmán, *Directional cloning of native PCR products with preformed sticky ends (autosticky PCR)*, Molecular And General Genetics **260** (1999) 569–573.

[188] S. J. DeCamp, G. S. Redner, A. Baskaran, M. F. Hagan, and Z. Dogic, *Orientational order of motile defects in active nematics*, Nature Materials **14** (8, 2015) 1110–1115.